

# HIGH PERFORMANCE PEROVSKITE PHOTODETECTORS

by

Aureliano Perez III, B.S.

A thesis submitted to the Graduate Council of  
Texas State University in partial fulfillment  
of the requirements for the degree of  
Master of Science  
with a Major in Physics  
August 2017

Committee Members:

Alexander Zakhidov, Chair

Jian Li

Casey Smith

**COPYRIGHT**

by

Aureliano Perez III

2017

## **FAIR USE AND AUTHOR'S PERMISSION STATEMENT**

### **Fair Use**

This work is protected by the Copyright Laws of the United States (Public Law 94-553, section 107). Consistent with fair use as defined in the Copyright Laws, brief quotations from this material are allowed with proper acknowledgement. Use of this material for financial gain without the author's express written permission is not allowed.

### **Duplication Permission**

As the copyright holder of this work I, Aureliano Perez III, authorize duplication of this work, in whole or in part, for educational or scholarly purposes only.

## **ACKNOWLEDGEMENTS**

As I begin, I wish to thank the members of my graduate committee:

Dr. Alexander Zakhidov, Dr. Jian Li, and Dr. Casey Smith. I express my utmost appreciation to Dr. Zakhidov for his patience, guidance, and interest throughout the completion of this work. I consider myself fortunate to have been given the opportunity to work with such a dedicated scientist and educator.

I offer my thanks to Dr. Swaminathan Venkatesen, Dr. Dmitry Layashenko, Mr. Christopher Manspeaker, and Mr. Mehedhi Hasan for their insight and support.

I offer my thanks to the Analysis Research Service Center (ARSC) and the Nanofabrication Research Service Center (NRSC) for providing the equipment and training necessary for many of the highly-sophisticated instruments used in this effort.

I offer my thanks to my parents, Aureliano Jr. and Charlotte, for their love, understanding, hard work, sacrifices, and perseverance in providing me the opportunities of a university education. Their guidance and support has been the foundation of all that I have achieved.

I would finally like to thank all my friends for their continued support and humor.

## TABLE OF CONTENTS

	<b>Page</b>
ACKNOWLEDGEMENTS .....	iv
LIST OF TABLES .....	vii
LIST OF FIGURES .....	viii
ABSTRACT .....	xii
CHAPTER	
1. INTRODUCTION .....	1
1.1 Background and Motivation .....	1
1.2 Organic Perovskites: Structures and Deposition Methods .....	3
1.3 Photodetectors and Solar Cells .....	6
1.4 Perovskite Photodiodes .....	16
1.5 Figures of Merit .....	20
1.6 Photolithography .....	23
2. METHODS .....	33
2.1 Device Fabrication .....	33
2.2 X-Ray Diffraction .....	41
2.3 Scanning Electron Microscopy .....	43
2.4 Atomic Force Microscopy .....	44
2.5 Profilometry .....	47
2.6 Current-Voltage Measurements .....	48
2.7 External Quantum Efficiency Measurements .....	50
3. RESULTS .....	51
3.1 Device Optimization .....	51
3.2 Comparative Analysis .....	67
3.3 Patterning Results .....	77
4. CONCLUSIONS .....	88
APPENDIX SECTION .....	91

REFERENCES ..... 92

## LIST OF TABLES

Table	Page
1. Typical values of commercially available (Si, GaAs, Germanium), and lab-scale (CdTe, perovskite) photodetectors.....	23
2. Average values of device PCE, $V_{OC}$ , $I_{SC}$ , and FF for varying ratios of $PbI_2$ to MAAC .....	52
3. Average values of device PCE, $V_{OC}$ , $I_{SC}$ , and FF for varying MAI concentrations .....	54
4. Average values of device PCE, $V_{OC}$ , $I_{SC}$ , and FF for varying levels of humidity during perovskite film annealing step.....	57
5. Average values of device PCE, $V_{OC}$ , $I_{SC}$ , and FF measured under AM1.5G illumination for varying temperatures and times of perovskite annealing step ....	60
6. Initial test matrix developed using JMP Pro 12 design of experiments software.....	62
7. Average values of device PCE, $V_{OC}$ , $I_{SC}$ , and FF for varying concentrations of MAI and varying spin speeds of $PbI_2$ -MAAC and MAI depositions.....	63
8. New test matrix developed using JMP Pro 12 design of experiments software and results from initial test .....	64
9. Average values of device PCE, $V_{OC}$ , $I_{SC}$ , and FF for varying concentrations of MAI and varying spin speeds of $PbI_2$ -MAAC and MAI depositions.....	64
10. Profilometer Measurements .....	66
11. Optimized device performance values for perovskite films grown with and without MAAC .....	73
12. Atomic spectra of I, H, N, and F.....	82

## LIST OF FIGURES

Figure	Page
1. CCD and CMOS Image sensor market as reported by SONY .....	1
2. Diagram of typical perovskite crystal structure with $A=CH_3NH_3$ , $B=Pb$ , and $X_3=I_3$ .....	3
3. Radiative (a) generation and (b) recombination mechanisms for an arbitrary semiconductor with an energy band gap of $E_g$ .....	8
4. Intrinsic silicon's absorption coefficient as a function of wavelength .....	10
5. Band bending typically seen at junction of an n-type semiconductor and a p-type semiconductor .....	12
6. Typical current-voltage dependence for photodiodes subject to illumination.....	16
7. Typical layer stack of perovskite photodiodes.....	19
8. Photoresist film thickness dependence on spin speed.....	26
9. Diazoquinone (DQ), one of the most common photoactive compounds in i-line and g-line exposure resists .....	28
10. Dose to clear swing curve for AZ5214-E photoresist.....	29
11. Setup of equipment used for MAAC synthesis .....	34
12. ITO (blue) pattern on glass substrates .....	35
13. From left to right, perovskite sample and template, template over perovskite sample, and scratched perovskite sample .....	36
14. 3-D printer converted into capping instrument for perovskite devices.....	37
15. From left to right, capped perovskite sample unaltered, with edges scratched off, with silver paint applied.....	37
16. SuSSMJB4 Contact Mask Aligner .....	39
17. Oxford ICP RIE Plasmalab 100.....	39

18. (a) Principle scheme of photolithographic patterning of $\text{CH}_3\text{NH}_3\text{PbI}_3$ films .....	40
19. Rigaku SmartLab X-Ray Diffractometer.....	42
20. XRD operation schematic.....	42
21. FEI Helios NanoLab 400 Scanning Electron Microscope.....	44
22. Block-diagram depicting cantilever deflection.....	46
23. AIST-NT SmartSPM Atomic Force Microscope .....	47
24. Bruker DektakXT Stylus Profilometer .....	48
25. Current-Voltage measurement equipment .....	49
26. Schematic of external quantum efficiency measurement setup.....	50
27. Statistical analysis of photovoltaic data recorded under AM1.5G illumination for varying ratios of $\text{PbI}_2$ to MAAc.....	52
28. Current-Voltage curves obtained from measurements taken under AM1.5G illumination for devices with varying ratios of $\text{PbI}_2$ to MAAc.....	53
29. Statistical analysis of photovoltaic data recorded under AM1.5G illumination for varying MAI concentrations .....	54
30. Current-Voltage curves obtained from measurements taken under AM1.5G illumination for devices with varying MAI concentrations.....	55
31. XRD spectra for $\text{PbI}_2$ -MAAc with various MAI concentrations.....	56
32. Statistical analysis of photovoltaic data recorded under AM1.5G illumination for varying levels of humidity during perovskite film annealing step .....	57
33. Current-Voltage curves obtained from measurements taken under AM1.5G illumination for devices with varying levels of humidity during perovskite annealing step.....	58
34. (a) J-V characteristics of the devices where the perovskite precursor films annealed under different humidity level at $90^\circ\text{C}$ for 2h.....	59
35. Power conversion efficiency variation with humidity .....	59

36. Statistical analysis of photovoltaic data recorded under AM1.5G illumination for varying levels temperature and time for perovskite annealing step.....	61
37. Statistical analysis of photovoltaic data recorded under AM1.5G illumination for initial test matrix developed for perovskite film thickness optimization.....	63
38. Statistical analysis of photovoltaic data recorded under AM1.5G illumination for new test matrix developed for perovskite film thickness optimization .....	65
39. XRD spectra of perovskite films grown with, and without MAAC .....	68
40. AFM surface scan of perovskite film grown using a standard one-step growth method.....	69
41. AFM surface scan of perovskite film grown using a standard two-step growth method.....	70
42. AFM surface scan of perovskite film grown using two-step growth method with MAAC adduct.....	71
43. SEM images of perovskite films grown (a) without MAAC, and (b) with MAAC .....	72
44. Higher magnification SEM images of perovskite films grown (a) without MAAC, and (b) with MAAC.....	72
45. Dark, and AM1.5G illuminated, Current-Voltage curves for a large area (6.25mm <sup>2</sup> ), single pixel perovskite photodetector made using our novel, MAAC containing, two-step process.....	74
46. Current-voltage analysis of champion devices fabricated with, and without, MAAC .....	75
47. External quantum efficiency and integrated current density measurements for an optimized device made using our novel two-step, MAAC containing, process....	76
48. Absorption spectrum of perovskite synthesized using two-step-solution-based spin coating with, and without, MAAC.....	77
49. Solvency tests of CH <sub>3</sub> NH <sub>3</sub> PbI <sub>3</sub> in various solvents with different polarity .....	78
50. XRD spectra of CH <sub>3</sub> NH <sub>3</sub> PbI <sub>3</sub> film after immersion in IPA solvent for 10 minutes.....	78

51. (a) PGMEA (propylene glycol methyl ether acetate) solvent, while overall being a poor solvent for $\text{CH}_3\text{NH}_3\text{PbI}_3$ does dissolve the film near the meniscus.....	79
52. (a) XRD spectra, (b) optical transmission spectra, (c) cross-sectional SEM image, (d) SEM image of surface, and (e) EDS of resist protected and unprotected portions of perovskite film after complete patterning process.....	81
53. Time dependence of characteristic optical transitions for atomic I, H, N, and F acquired from optical emission spectra of the plasma .....	83
54. Optical emission spectrum taken in-situ from gas-discharge plasma 20 sec after plasma ignition.....	84
55. Device structure of organic perovskite photodiode for (a) non-patterned reference device and (b) patterned device .....	87
56. Patterned perovskite.....	90

## ABSTRACT

Organohalide lead perovskite ( $\text{CH}_3\text{NH}_3\text{PbI}_3$ ) is a novel material with promising applicability for visible light photo-detectors. The ability to develop perovskite photodetector devices using a low temperature solution based process allows straightforward combinations with other materials, including traditional crystalline semiconductors, with minimal contributions to cost and process complexity. Lab-scale perovskite photodetectors and solar cells grown using traditional single, or multiple, precursor deposition steps are typically plagued by low film uniformity and reproducibility. This not only limits optimal device performance, but also provides for highly variable results. In traditional two-step processing, a film of layered lead iodide ( $\text{PbI}_2$ ) is grown, followed by application of methyl-ammonium iodide (MAI). These precursor compounds react uncontrollably before MAI can fully intercalate into the spaces separating the layers of  $\text{PbI}_2$ . This work presents a novel two-step perovskite growth technique which utilizes methyl-ammonium acetate (MAAc) to better control precursor reaction/perovskite crystallization, yielding thin films which have improved uniformity and reproducibility. Perovskite films grown using our novel two-step processing, as well as traditional growth techniques, are characterized using various metrology techniques. Additionally, devices fabricated with, and without, MAAc undergo current-voltage characterization under AM1.5G simulated solar light, as well as external quantum efficiency measurements. In addition to the need for more uniform and reproducible perovskite films, there is a need for high-resolution structuring of these

films to minimize cross-talk between neighboring detectors (pixels) for imaging purposes. This work presents a method to develop  $\text{CH}_3\text{NH}_3\text{PbI}_3$  thin films possessing high-resolution patterning, using lithography processing with hydrofluoroether solvents. The results presented herein confirm that, unlike the majority of traditional solvents utilized in conventional photolithography, hydrofluoroethers do not adversely affect  $\text{CH}_3\text{NH}_3\text{PbI}_3$  films, enabling photolithographic processing. Transfer of the resist pattern is achieved using a  $\text{SF}_6$  plasma functionalization process which extracts iodine and organic components from the film, converting the perovskite into  $\text{PbF}_2$ . This work also demonstrates that isolation of perovskite photodetecting pixels with a 20  $\mu\text{m}$ -wide stripe of  $\text{PbF}_2$  leads to a 4.5-fold reduction in the cross-talk between neighboring pixels. It is believed that our method will facilitate simple monolithic integration of perovskite photodiodes to the silicon backplane chip utilized in active-pixel sensor and charge-coupled device applications.

# 1. INTRODUCTION

## 1.1 Background and Motivation

Photodetectors have applications in a range of sophisticated technologies ranging from consumer electronics (digital cameras, smoke detectors, CD, DVD, and Blu-ray players, *ect.*) to medical imaging, automotive & transportation, and military equipment (low-light/night vision optics, biosensors, reconnaissance and surveillance devices, active armor, *etc.*). The market of visible photodetector arrays based for consumer applications currently exceeds \$6.0 billion USD (Figure 1).

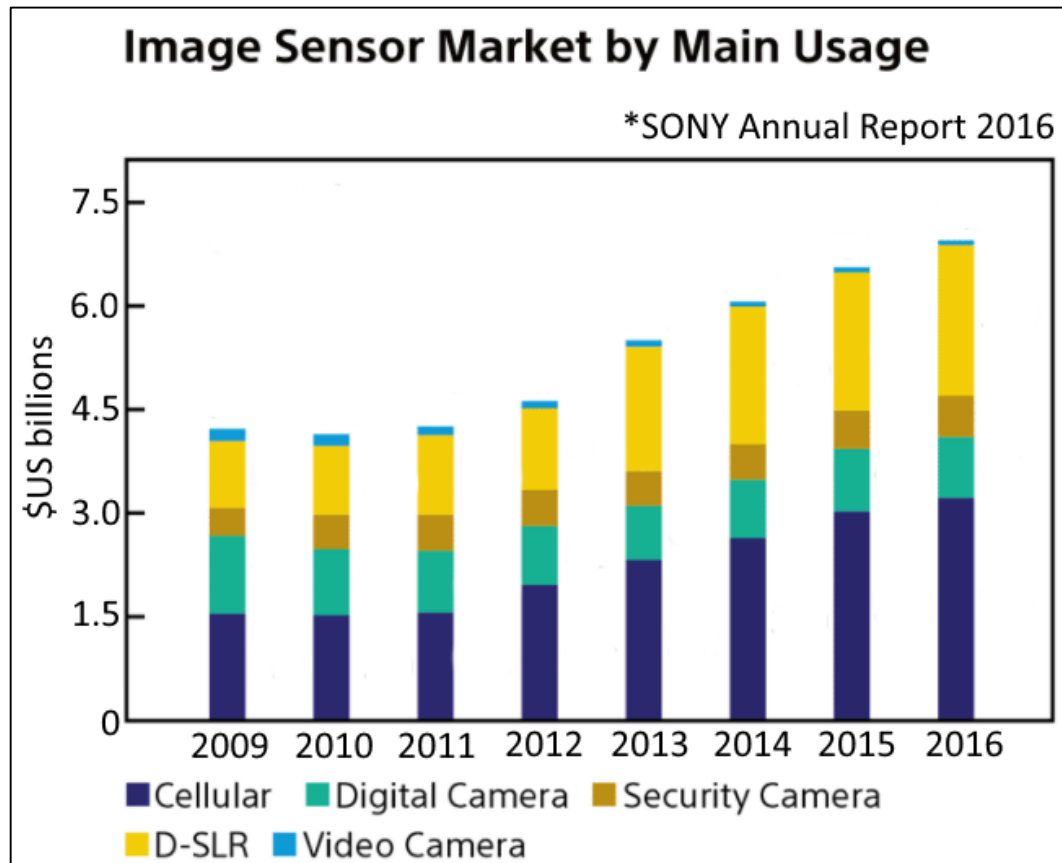


Figure 1: CCD and CMOS Image sensor market as reported by SONY.<sup>1</sup>

Currently, this market is dominated by Si-based technologies due to superior device fabrication protocols compared to all other options. Yet, silicon is an indirect

bandgap semiconductor with quite poor absorption. Thus, sensitivity of current image sensors is quite low and in many cases, this limits camera response times. Organic and hybrid organic-inorganic photodiodes are making strides to become viable, low-cost, flexible alternatives to traditional inorganic semiconductor based devices.<sup>2-5</sup> Reports of high sensitivities, low response times, high external quantum efficiencies over the entire visible spectral range, low-temperature solution processing, and low precursor costs make this class of materials very promising for the next generation of visible sensors.

Moreover, due to relaxed operational conditions (less exposure to bright light sources, less thermal stress) and lower utilization lifetime (average U.S. consumer replaces their cellphone every 2 years) when compared to solar cell devices, perovskite photodiodes might see expedited commercialization in the near future. However, to be able to make a functional photodiode array and integrate it with backplane electronics (i.e. based on CMOS-Complementary Metal-Oxide-Semiconductor technology) a reliable **high-resolution patterning method is urgently needed**. Whereas extensive lithographic processes and equipment are readily available for patterning of inorganic circuit components, micro-patterning, processing and integration of organic materials destined for optoelectronic systems remain among the most challenging engineering issues to be addressed. In this work, I explore a method called **Orthogonal Lithography** to be applied to structure perovskite pixels for photodetector arrays.<sup>6</sup> I also address fundamental mechanisms of perovskite device operation and study **structure-property relationships** for the novel perovskite film deposition method using methyl ammonium acetate (MAAc) adduct.

## 1.2 Organic Perovskites: Structures and Deposition Methods

Hybrid organic-inorganic perovskites (HP) are novel, promising semiconductors for **low cost** and **high performance** photovoltaic applications. Power conversion efficiencies (PCE) of HP solar cells has skyrocketed from 3.8% to **>22% in just five years**<sup>7</sup> and now rivals that of heavily developed conventional CIGS, CdTe, and Si-based solar cells. Unlike most organic semiconductors which have essentially amorphous structures, hybrid perovskites possess a well-defined crystal lattice with the structure of  $ABX_3$ . A diagram of this structure can be seen in Figure 2.

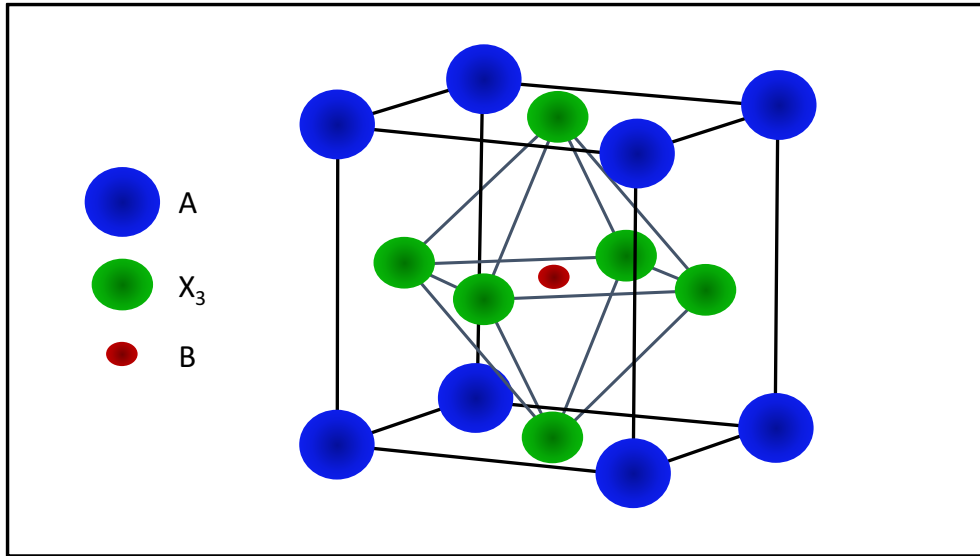


**Figure 2: Diagram of typical perovskite crystal structure with  $A=CH_3NH_3$ ,  $B=Pb$ , and  $X_3=I_3$ .**

Under ideal conditions, to maintain highly symmetric cubic structure ( $\alpha$ -phase), the ionic radii of  $r_A$ ,  $r_B$ , and  $r_X$  should satisfy so called Goldschmidt rule<sup>8</sup> for tolerance factor  $t$ :

$$t = \frac{r_A + r_X}{\sqrt{2}(r_B + r_X)} \approx 1 \quad (1)$$

Stable perovskites only form when  $0.8 < t \leq 1$ . For  $t < 1$ , lower symmetry tetragonal ( $\beta$ -

phase) or orthorhombic ( $\gamma$ -phase) structures are formed, whereas  $t > 1$  results in destabilization of the 3D network leading to formation of 2D layered structures.<sup>9</sup> For lead halide perovskites ( $B = \text{Pb}$ ) and ( $X = \text{I}$ ) to satisfy  $t \sim 1$ , the A ion must be much larger than the Pb ion. Cs, the largest stable group-I element in the periodic table, is not large enough<sup>9</sup> to make a thermodynamically stable structure ( $t = 0.8$ ). Therefore, a large organic cation is needed for the A site.

Amongst all organic perovskites explored so far, methylammonium-lead(II)-iodide ( $\text{CH}_3\text{NH}_3\text{PbI}_3$  or MAPbI), a carbon containing (organic or hybrid) compound, is becoming a staple in hybrid organic-inorganic photovoltaic research with the highest reported PCE. It is a strongly absorbing direct 1.6 eV bandgap semiconductor.<sup>10</sup> It is also an intrinsic semiconductor with high, and balanced, carrier mobilities,<sup>11</sup> shallow defect levels,<sup>12</sup> and large  $> 1 \mu\text{m}$  carrier diffusion lengths,<sup>13</sup> which are all critical metrics for high performing photonic devices.

Typical processing of perovskite devices involves solvation of precursor materials into “inks” that are applied to substrate in a one- or two-step method, via solution printing (e.g. spin coating), followed by thermal annealing to bake away residual solvents and to promote crystallization. To create thin films of  $\text{CH}_3\text{NH}_3\text{PbI}_3$ , lead (II) iodide ( $\text{PbI}_2$ ) and methylammonium iodide ( $\text{CH}_3\text{NH}_3\text{I}$ ) are dissolved either together in a single solvent (one-step method)<sup>14</sup>, or separately in two unique solvents (two-step method).<sup>15</sup> In single-step processing,  $\text{CH}_3\text{NH}_3\text{I}$  and  $\text{PbI}_2$  are typically dissolved in dimethylformamide (DMF) and spun together onto substrate. For two-step processing, lead (II) iodide in DMF is applied first, resulting in a thin film of  $\text{PbI}_2$ , a layered semiconductor with distinct yellow appearance.  $\text{CH}_3\text{NH}_3\text{I}$  in isopropanol (IPA)

is then applied via spin coating, during which time  $\text{CH}_3\text{NH}_3\text{I}$  molecules react with, and intercalate into spaces between discrete layers of, lead iodide. One-step processing typically yields larger grains but poor uniformity and coverage. Although devices made using two-step methods typically exhibit smaller grains, they provide more uniform films, resulting in higher power conversion efficiencies (PCEs).<sup>16</sup>

An already large and continuously growing list of techniques used to create perovskite thin films has allowed for exciting, rapid device performance improvements. However, this also illustrates that there remains a fundamental lack of understanding of basic properties associated with trihalide perovskites, namely, perovskite crystallization mechanisms. Each technique typically varies perovskite growth parameters in attempts to enhance performance, resulting in unknown, hard to measure changes in reaction/crystallization mechanisms. A fundamental connection between every technique, however, is performance dependence on film uniformity and quality.

Major implications in standard hybrid organic-inorganic device fabrication techniques arise from inefficient perovskite formation, likely due to uncontrollable precursor reaction rates. Other implications occur as result of large variability in perovskite film quality. Although there exist other implications, most of which are more relevant to distinct fabrication techniques, they are not of critical importance here. Several efforts which attempt to address these issues, such as solvent engineering and intermolecular exchange *via* utilization of alternate lead salts, enhance performances and expand what little is understood about reaction/crystallization mechanisms.<sup>17-19</sup> Another implication with perovskites is inability to effectively pattern  $\text{CH}_3\text{NH}_3\text{PbI}_3$  through standard photolithographic processing due to high solubility levels in traditional

photoresist developers and solvents. Without patterning capabilities, perovskite photodetectors are limited to devices with a low number of large pixels, making them impractical for modern photodetector device applications. Scalability and stability issues restrict perovskite devices to research-focused, lab-scale efforts. Cost-effective, commercial-level fabrication and integration of organic photovoltaics cannot be idealized until these challenges are overcome. The focus of this work is to address these processing complications, expand what is known about reaction/crystallization mechanisms, and develop organic photodetector and solar cell technologies to advance viable competitors with traditional inorganic semiconductor-based devices.

### **1.3 Photodetectors and Solar Cells**

Before we delve deeper into these processes and techniques, a brief overview of the physics of photodetectors and solar cells is necessary. These devices are based on semiconductors, which are a special class of material with unique electric properties. The defining characteristic of semiconductors is known as the band gap; a range of energy in which quantum phenomena forbids the presence of electrons. A band gap is typically a measure of difference between the bottom of the conduction band and the top of the valence band. Conduction and valence bands, as well as band gaps, are present in all semiconductors. In conduction bands, electrons are viewed as free particles, with no energy bounds restricting their movement. Valence bands are regions where electrons are bound within the atoms which make up the crystal structure of the semiconductor.

Through proper energetic stimuli, it is possible for electrons to transition from one band to the other. In determining if a certain stimulation will promote transition, the source of stimulation is irrelevant. What is of specific importance in this determination,

however, is the amount of energy the stimuli impart to the electrons in the semiconductor. Semiconductors can be thought of as intermediates between conductors and insulators. Conductors are materials which exhibit virtually no energy band gap, allowing for electrons to flow uninhibited. Insulators, conversely, have such enormous band gaps that it is highly improbable for any electrons to occupy unbound states in the material. Band gaps are typically different for differing materials and are determined by the material's unique atomic or molecular structure. An electron bound to the valence band can be promoted to the conduction band through electromagnetic (photons) or thermal (phonons) stimulation.

Solar cell and photodetector devices are contingent upon electromagnetic stimulation. The energy associated with a quanta of light, or photon, is given through the relation

$$E_{\text{photon}} = \frac{hc}{\lambda} \quad (2)$$

where  $h$  is Planck's constant,  $c$  is the speed, and  $\lambda$  the wavelength, of the light in vacuum. If a photon with energy greater or equal to that of a semiconductor's band gap encounters an electron in the valence band, it is possible for the bound electron to absorb the photon's energy and transition to a free state in the conduction band, leaving a vacancy (hole) in the valence band. Holes are described as free charge carriers similar to electrons in the conduction band. This is due to the ability of electrons bound to atoms which neighbor hole-containing atoms to fill these holes, leaving their original atoms with vacancies. Further discussion on electron and hole characteristics would become too narrow in scope, and is not necessary due to an abundance of literature pertaining to that topic.

Exciting a bound electron to the conduction band, and the vacancy it leaves behind is a process known as carrier generation. Electrons in the conduction band, and holes in the valence band, act as charge carriers and contribute to the current when the semiconductor is utilized in a device. However, electrons and holes possess opposite electric charges, causing an attractive force between them. If this force is strong enough, it can cause electrons to transition from the conduction band back down to occupy the holes they left. This process is called recombination, and when an electron-hole pair recombine, the electron transfers back to a lower energy state in the valence band, causing emission of a photon with energy equal to the band gap energy. This generation of photons through charge carrier recombination is known as photoluminescence (or radiative recombination). Figure 3 offers a visual representation for radiative generation and recombination mechanisms. Solar cells and photodetectors generate current through creation of electron-hole pairs and are designed to reduce free charge carrier recombination. Typically, an applied bias voltage creates an electric field which acts to separate these carriers, inhibiting instantaneous recombination.

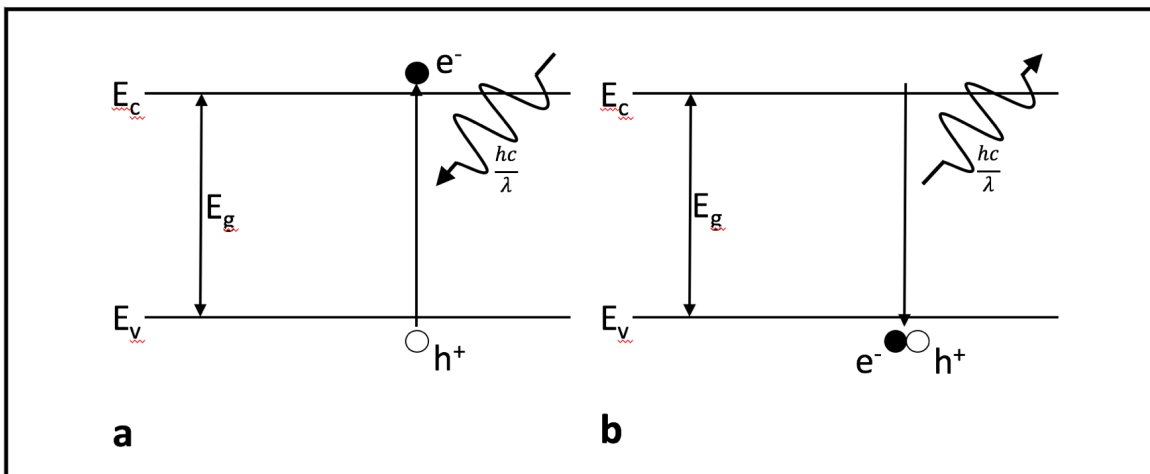


**Figure 3: Radiative (a) generation and (b) recombination mechanisms for an arbitrary semiconductor with an energy band gap of  $E_g$ .**

As previously noted, electromagnetic radiation can create electron-hole pairs in a semiconductor through radiative generation. While penetrating a semiconductor, light is absorbed at a rate dependent on the material in consideration. The absorption coefficient,  $\alpha$ , gives the ratio of photons absorbed per unit length of penetration. *Lambert-Beer's Law* gives a mathematical model for this absorption mechanism and is defined as

$$\Phi(d) = \Phi_0 e^{-\alpha d} \quad (3)$$

where  $\Phi(d)$  is the measure of photon flux at an arbitrary depth  $d$ , and  $\Phi_0$  is the photon flux measured at the surface. Using the above relation, it is easy to see that at a penetration depth of  $1/\alpha$ , only  $e^{-1}=36.8\%$  of the number of photons that hit the surface will remain. The absorption coefficient is strongly dependent on wavelength and is a material constant. To give a more concrete representation of how the absorption coefficient depends on wavelength, Figure 4 shows silicon's absorption coefficient as a function of wavelength.

Intrinsic silicon has an energy band gap of 1.11 eV at room temperature. Due to silicon's band gap, electromagnetic radiation with wavelength longer than 1.1  $\mu\text{m}$  in vacuum will not likely cause carrier generation in intrinsic silicon at room temperature. This is due to photons having less energy for longer wavelengths. When photons with insufficient energy pass through a semiconductor, they are very unlikely to be absorbed, resulting in high penetration depths. Photons with energies greater than or equal to a semiconductor's band gap, however, are much more likely to be absorbed in the creation of electron-hole pairs. Figure 4 shows that decreasing wavelength yields a gradual increase in absorption coefficient. For 850 nm light, the absorption coefficient of intrinsic silicon is  $0.038 \mu\text{m}^{-1}$ , 660 nm light gives an absorption coefficient of  $0.23 \mu\text{m}^{-1}$ ,

while 405 nm light yields  $7.5 \mu\text{m}^{-1}$ . The penetration depths associated with these absorption coefficients are:  $26.2 \mu\text{m}$ ,  $4.35 \mu\text{m}$ , and  $0.132 \mu\text{m}$ , respectively. These example wavelengths were chosen due to their common use in optical devices: 850 nm is typical for small optical links, 660 nm is ideal for polymeric optical fibers, and 405 nm is the wavelength used in Blu-ray devices.

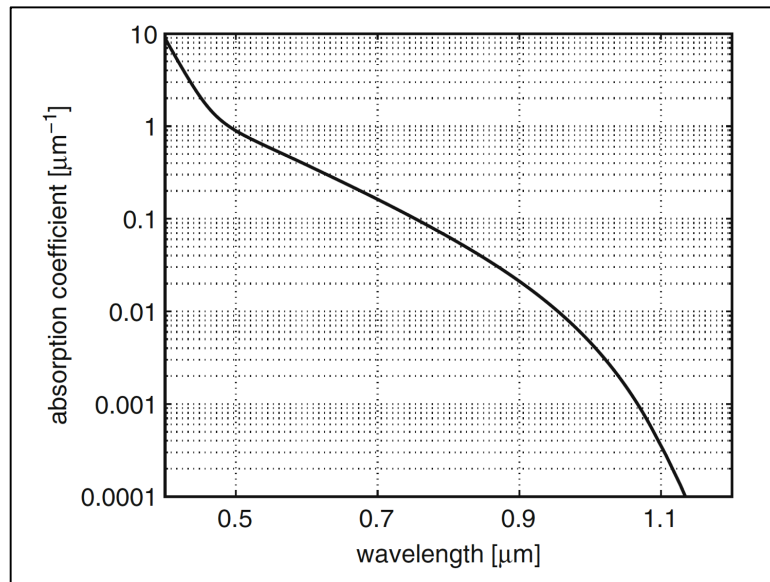


**Figure 4: Intrinsic silicon's absorption coefficient as a function of wavelength.<sup>20</sup>**

Silicon is utilized heavily in photovoltaic devices due to fantastically efficient manufacturing and yield. Silicon is, however, an indirect band gap semiconductor, meaning that the highest energy state of the valence band does not align with the minimum energy state of the conduction band. This corresponds to different electron momenta in these bands. This offset necessitates phonon interaction for effective electron-hole pair generation, causing indirect band gap semiconductors, such as silicon, to have longer penetration depths than direct band gap semiconductors. Consequently, direct band gap semiconductors typically exhibit greater radiative generation rates than indirect band gap semiconductors.

Although the crystal structures of semiconductor devices are typically highly ordered and uniform, there are inevitable defects found in most devices. Defects introduce states with energy levels within the material's band gap. These intermediate levels allow for electrons to transition between the valence and conduction bands in multiple steps instead of a single step. This process is known as Shockley-Read-Hall generation and recombination. Imperfections and impurities serve as recombination centers for photo-generated electron-hole pairs in photovoltaic devices. Some defects are present within the bulk of semiconductors; however, surface and interface defects are much more common. Defects within the bulk create discrete electronic states, while surface impurities cause a continuum of energy levels within the band gap. As such, surface and bulk recombination mechanisms must be treated individually. Both surface and bulk Shockley-Read-Hall recombination mechanisms are the dominant recombination processes in silicon and other indirect band gap photovoltaics.

After photo-generation of electron-hole pairs, it is necessary to collect these charge carriers before they can recombine. Due to the opposite charges associated with these carriers, an electric field can force carriers away from each other. Photoconductors, phototransistors, and photodiodes utilize this concept to convert light into useful electric signals. Photoconductors and phototransistors typically do not make for ideal photodetectors due to low conversion speeds and difficulty in efficiently implementing them in conjunction with standard CMOS technology.

Photodiodes typically exhibit an abrupt junction of an anode (p-type doped semiconductor) on one side, and a cathode (n-type doped semiconductor) on the other. Due to lack of balance of free charge carriers throughout the structure, diffusion occurs.

Electrons move from n-type side to p-type side, while holes migrate from p-type side to n-type side. This diffusion causes the n-type side to become positively charged, while the p-type region becomes negatively charged, effectively creating an electric field in both regions. This electric field induces a drift current, simultaneously forcing electrons back to the n-type side and holes to the p-type side, counterbalancing the diffusion currents. Zero net current flows once diffusion and drift currents are equivalent, and the device is in equilibrium.

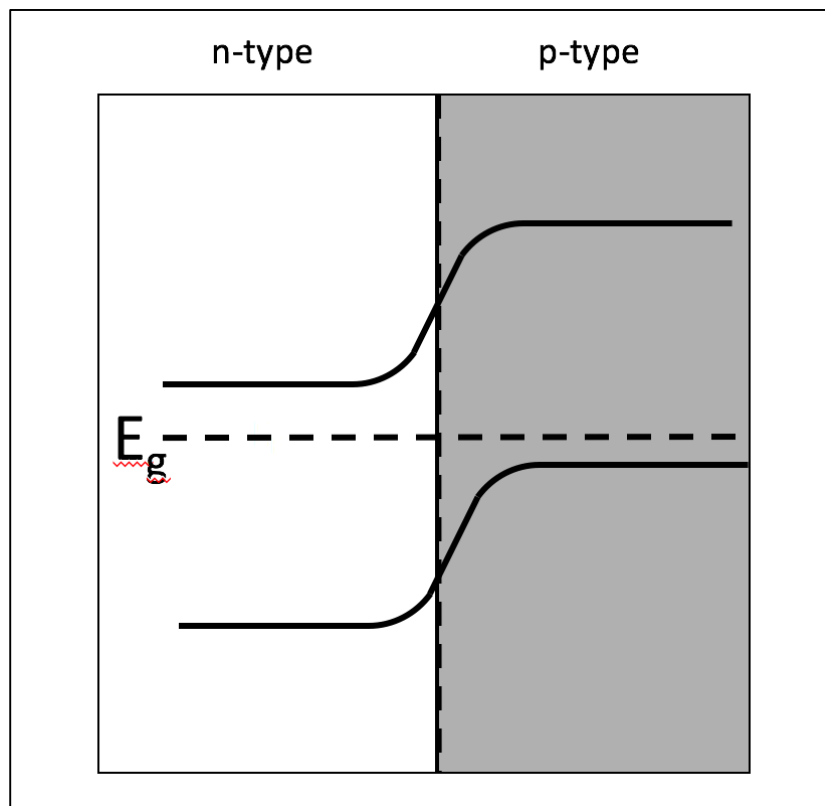


**Figure5: Band bending typically seen at junction of an n-type semiconductor and a p-type semiconductor.**

In addition to evoking drift currents, the electric field causes a variation in electric potential across the device, which causes band bending to occur around the junction of n-, and p-type regions. An example of this can be seen in Figure 5. In the region where the

electric field is present, there exists a nonzero net charge due to electrons and holes present in p-, and n-type regions, respectively. This area is commonly referred to as the depletion zone. The width of the depletion zone, as well as the extent to which it extends into each region, is dependent on doping concentrations in the n-, and p-type regions. For abrupt junctions, this relationship is given as:

$$W = \sqrt{\frac{2\varepsilon(N_A + N_D)}{qN_A N_D}} (V_i) \quad (4)$$

where  $W$  is depletion zone width,  $\varepsilon$  the material permittivity,  $N_A$  the p-type doping concentration,  $N_D$  the n-type doping concentration, and  $V_i$  the internal voltage. The internal voltage is also dependent on doping concentrations and is described as:

$$V_i = \frac{kT}{q} \ln \left( \frac{N_A N_D}{n_i^2} \right) \quad (5)$$

where  $k$  is Boltzmann's constant,  $T$  temperature, and  $n_i$  the intrinsic carrier concentration.

Because photodiodes are non-symmetrical, they respond to applied voltages in non-linear fashion. If a diode has higher voltage at its anode, it is forward biased, while if the voltage is higher at the cathode, it is reverse biased. Forward biasing tends to reduce the depletion zone width, while reverse biasing acts to widen it. This can be seen by a modification of Equation 4:

$$W = \sqrt{\frac{2\varepsilon(N_A + N_D)}{qN_A N_D}} (V_i - V_b) \quad (6)$$

where  $V_b$  is the biasing voltage.

The depletion zone acts as an insulating region between two conductive layers. Forward biasing a photodiode causes majority carriers to move from the depletion zone

into these layers, causing the depletion zone width to decrease. On the other hand, reverse biasing a photodiode increases the depletion zone width by moving charge carriers from the doped regions, into the depletion zone. This behavior is described as the junction capacitance, and, assuming an abrupt junction, is modeled by the following equation:

$$C_j = \left[ A \sqrt{\frac{q\epsilon N_A N_D}{2V_i(N_A + N_D)}} \right] \left( 1 - \frac{V_b}{V_i} \right)^{-\frac{1}{2}} \quad (7)$$

where the first term in brackets is the junction capacitance when no bias is applied.

Until now, we have only considered the case of PN-junction photodiodes.

However, it is common for a photodiode to utilize a third, intrinsic layer sandwiched between the two doped regions, which we refer to as a PIN photodiode. This intrinsic layer acts as a wider depletion zone, drastically reducing junction capacitance compared to PN-junction devices. In addition to being reduced, the junction capacitance for a PIN device is practically independent of bias voltage.

When photons of sufficient energy interact with a photodiode, electron-hole pairs are created in the doped regions as well as the depletion zone. The electric field in the depletion zone separates photo-generated electron hole pairs, producing a photocurrent between the anode and cathode. Electron-hole pairs generated in doped regions can diffuse into the depletion zone if they are generated close enough to its edge. For this to be a probable event, an electron hole pair needs to be generated within one minority carrier diffusion length of the depletion zone. An electron's (hole's) diffusion length in the p-type (n-type) region is given by:

$$L_{e(h)} = \sqrt{D_{e(h)}\tau_{e(h)}} = \sqrt{\mu_{e(h)}\tau_{e(h)}\frac{kT}{q}} \quad (8)$$

where  $D_{e(h)}$  is the electron (hole) diffusion constant,  $\mu_{e(h)}$  is the carrier mobility, and  $\tau_{e(h)}$  is the average carrier lifetime.

Diffusion length can be thought of as the average length a minority carrier can travel before recombining with a majority carrier. Due to lack of electric field in the doped regions, diffusion mechanisms dictate photo-generated carrier movement. Thus, electron-hole pairs generated near one diffusion length of the depletion zone are capable of adding to the photocurrent, while those generated further away typically recombine before encountering the electric field present within the depletion zone.

Current through a photodiode is exponentially dependent on the voltage across it, as shown in the following:

$$I_d = I_s \left( e^{\frac{qV_b}{kT}} - 1 \right) \quad (9)$$

where  $I_s$  is the photodiode saturation current. A photodiode typically has a very low saturation current which is dependent on carrier mobilities, junction cross-sectional area, and doping characteristics. Figure 6 shows typical photodiode current-voltage dependence.

Figure 6 also describes solar cell operational characteristics. Solar cell operation differs from that of photodiodes in that solar cells convert solar energy into electrical energy, while photodiode operation consumes power. The major difference in solar cell and photodiode operation is the biasing conditions: photodiodes operate in reverse bias, while solar cells function with no bias. This difference is illustrated in Figure 6, with photodiode operation occurring in the third quadrant, while solar cell operation takes

place in the fourth quadrant of the coordinate system.

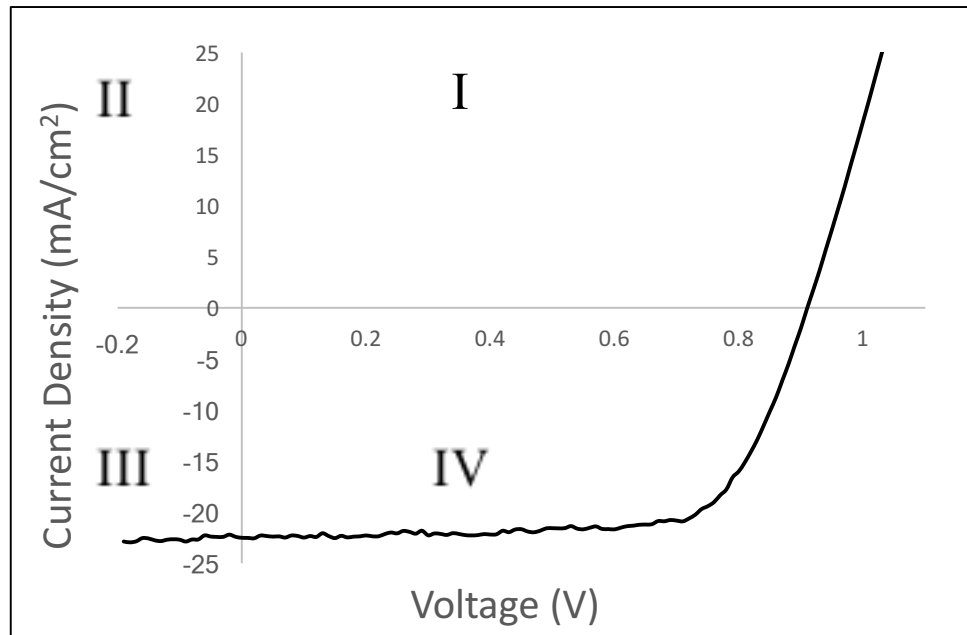


**Figure6: Typical current-voltage dependence for photodiodes subject to illumination.**

Traditional photodiodes utilize silicon as their photoactive layer, which makes it difficult to integrate them in CMOS technologies. This difficulty is largely due to silicon being an indirect band gap semiconductor with low absorption coefficient. Other complications arise in attempts to integrate silicon photodiodes in CMOS processes from limited junction freedom. Perovskite photodiodes, however, possess several characteristics which make them better suited for CMOS integration.

#### **1.4 Perovskite Photodiodes**

With a tunable, direct band-gap, perovskite shows capabilities to create high-performance photodiodes that can easily integrate into existing CMOS technologies.<sup>21,11</sup> Perovskite is also much more absorptive than silicon, which allows for sufficient carrier generation and collection to be achieved in films as thin as 350 nm.<sup>22</sup> These qualities

enable flexible devices with superior detection sensitivity. In addition, organohalide lead perovskites exhibit high carrier mobilities, long carrier diffusion lengths, and shallow defect levels.<sup>13,23,12</sup> These desirable properties, coupled with low-temperature solution processing of perovskite and compatible organic transport layers enables monolithic, cost-effective integration of these devices on CMOS backplanes.

Early perovskite-based optoelectronics utilized dye-sensitized device architectures. These devices utilized a mesoporous, charge-conducting scaffold, such as TiO<sub>2</sub>, on which perovskite was grown. In these early generation devices, photo-generated electrons in the perovskite layer transfer into the mesoporous sensitized layer before recombination mechanisms take over. Once in this layer, electrons move to the electrode, where they are extracted. While this architecture shows considerable potential, advancements in perovskite photodiodes and photovoltaics utilizing thin film architectures show more desirable characteristics. In addition to the fact that dye sensitized perovskite devices are prone to UV-induced degradation, it is difficult for perovskite layers to fully intercalate into the mesoporous scaffolding before reaction completion. Thin film architectures allow for perovskite monolayers possessing high uniformity to be coupled with organic charge transport layers to achieve highly efficient, flexible devices.

As described earlier, methylammonium iodide shows great capability in photodetector and solar cell applications. Introduction of mixed halides allows for precise control over band gap energies ranging from 1.6-2.3 eV. These simple tweaks to perovskite composition greatly expand its range of possible application. Modern perovskite devices exhibit electron and hole mobilities in excess of 2000 cm<sup>2</sup>/Vs and 300

$\text{cm}^2/\text{Vs}$ , respectively.<sup>11</sup> High mobilities, coupled with diffusion lengths up to 175  $\mu\text{m}$ , allow efficient carrier separation and collection to occur before recombination takes place.<sup>24,25</sup> These characteristics, combined with shallow defect levels, enable perovskite thin film architectures, where photo-generated carriers separate and travel through the perovskite layer, to surrounding charge transport layers.

Perovskite acts as the intrinsic, photoactive layer in pin photodiodes. Typically, it is sandwiched between an indium tin oxide (ITO) anode, and aluminum (Al), or silver (Ag) cathode. Al or Ag contacts are less desirable in silicon devices as they increase reflectivity, therefore lowering overall optical transmission and absorption, and thus detectivity. However, these highly reflective materials have clever application in inverted thin film devices. By orientating devices such that these contacts are at the back, light which is not absorbed in perovskite layers reflects back through, offering another chance for absorption. This essentially doubles the effective photoactive layer, without physically increasing its thickness.

In addition to  $\text{CH}_3\text{NH}_3\text{PbI}_3$ , anode, and cathode, hybrid organic-inorganic photodetectors typically utilize electron and hole transport layers. These layers increase mobilities of photo-generated charge carriers while reducing recombination effects. Poly(3,4-ethylenedioxythiophene) polystyrene sulfonate (PEDOT:PSS) or 2,2',7,7'-Tetrakis-(N,N-di-4-methoxyphenylamino)-9,9'-spirobifluorene (Spiro-OMeTAD) are commonly used as hole transport layers (HTL), which allows for rapid transit of holes excited in the perovskite layer to the cathode, while blocking electrons. Similarly, materials such as Buckminsterfullerene ( $\text{C}_{60}$ ) and phenyl-C70-butyric acid methyl ester ( $\text{PC}_{70}\text{BM}$ ) function as electron transport layers (ETL). Another common addition to

perovskite photodiodes is a thin (~7.5 nm) layer of bathocuproine (BCP), which helps reduce hysteresis seen between forward and reverse scanning of illuminated current-voltage characterization.<sup>26</sup> Figure 7 shows the cross-sectional, block diagram view of a typical perovskite photodiode.

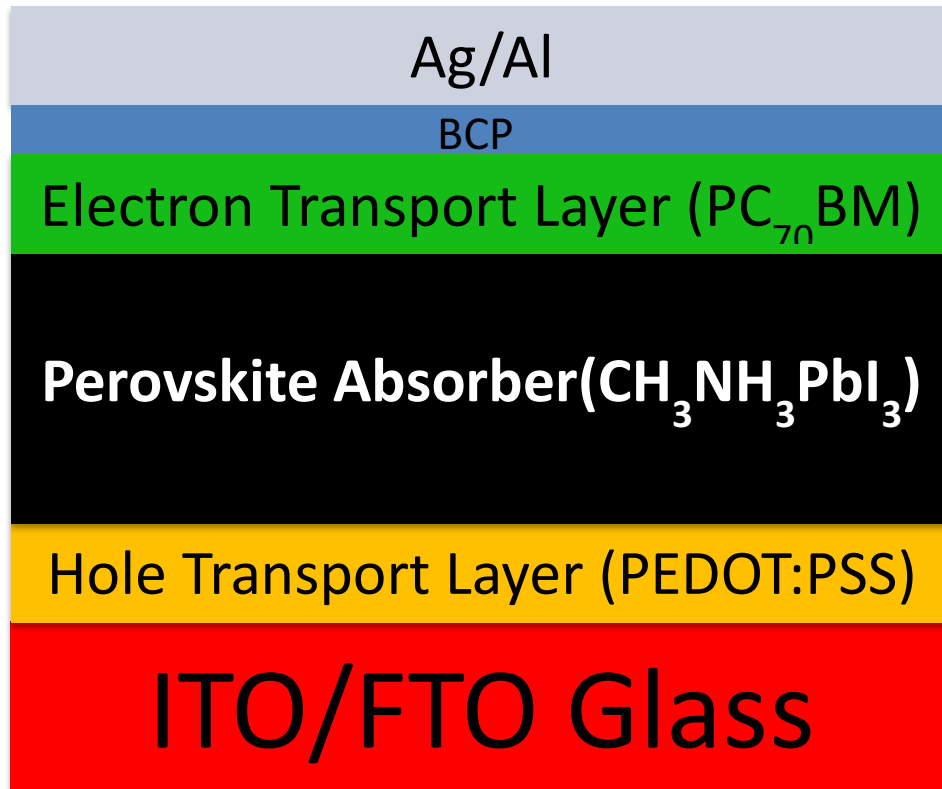


**Figure 7: Typical layer stack of perovskite photodiodes. Note that this scheme, which is representative of devices made in this study, depicts inverted device structures, meaning light is incident upon ITO/FTO side during operation.**

Although simple, low-temperature, solution processing makes perovskite-based devices attractive as cost-effective alternatives to traditional silicon photodiodes, it places limitations on film quality, device performance, and reproducibility. Reaction of precursor constituents (PbI<sub>2</sub> and MAI) occurs rather unpredictably. This uncontrollable reaction typically results in highly variable film qualities. Poor film qualities such as: high roughness, small grains, and areas of unreacted precursors, result in performance

degradation.

Recent reports show performance and reproducibility improvements through techniques such as solvent engineering to better control reaction/crystallization rates.<sup>19</sup> Solvent engineering typically creates an intermediate phase which allows for better control of precursor reaction, and perovskite crystallization rates. While some instances of solvent engineering seek to slow down these rates, other growth techniques require more rapid rates.<sup>19,27</sup> Another approach to better control and understand reaction and crystallization mechanisms is intermolecular exchange. In one instance, lead-halide salts are replaced by other lead salts, such as lead acetate (PbAc).<sup>28</sup> Intermolecular exchange occurs in the presence of excess MAI, which bonds to the acetate, allowing for other MAI molecules to react with newly freed Pb atoms. More rapid removal of both the acetate and excess MAI leaves behind dense, high quality CH<sub>3</sub>NH<sub>3</sub>PbI<sub>3</sub> films.<sup>29</sup> Other studies show clever manipulation of various compounds and solvents to better understand and control reaction/crystallization kinetics.<sup>30</sup>

Our efforts to improve perovskite reaction kinetics involves addition of methylammonium acetate (MAAc) to PbI<sub>2</sub> ink. We hypothesize that MAAc's presence in thin films of PbI<sub>2</sub> causes the interlayer "gallery" spacing to increase, allowing MAI to fully intercalate through before reaction completion. This adduct is removed along with excess MAI during a thermal annealing process following the two-step perovskite deposition procedure.

## **1.5 Figures of Merit**

With many different types of photodetectors made to target specific operational/performance requirements, it becomes difficult to determine if one device is

superior to another. Photodetector performance is characterized through several distinct operational metrics. These figures of merit include: detectivity, responsivity, noise equivalent power, external quantum efficiency, and linear dynamic range, among others. Through these, operational benchmarks can be established, allowing for succinct evaluation of any photodetector device, regardless of its targeted area of use.

A major qualifier for photodetectors is sensitivity; devices with greater sensitivities can detect weaker optical signals. Sensitivity is dependent on photocurrent, and the basic figure of merit here is quantum efficiency. Quantum efficiency ( $\eta$ ) is a measure of the number of charge carriers produced per photon:

$$\eta = \frac{I_p}{q\Phi} = \frac{I_p hf}{qP} \quad (10)$$

where  $I_p$  is photocurrent,  $\Phi$  photon flux, and  $P$  is the optical power. Ideally, quantum efficiency is unity, however incomplete absorption, reflection, recombination, *etc.* typically lower this value. Quantum efficiency is typically broken into two subgroups, external quantum efficiency (EQE) and internal quantum efficiency (IQE). The major difference between these two efficiencies, is that IQE describes the ratio of generated carriers to the number of photons which are absorbed, while EQE gives the ratio of generated carriers to the number of photons that interact with the device. Similar to quantum efficiency is responsivity ( $\mathcal{R}$ ), a metric which relates photocurrent to optical power,

$$\mathcal{R} = \frac{I_p}{P} = \frac{\eta q}{hf} \quad (11)$$

with units of A/W.

Quantum efficiency and responsivity describe levels of photocurrent that a device

can utilize as useful signal. Some devices employ amplifiers or internal gain mechanisms to increase this signal. Unfortunately, these also increase device noise, which limits the minimum detectable signal strength. Due to such a wide variety of signal and noise level requirements and tolerances among devices, it is convenient to link them in a signal-to-noise ratio. Dark current is noise seen when a photodetector is placed under bias, but not exposed to light. Internal device mechanisms such as thermal (Johnson) noise, shot noise, flicker noise, *etc.* add to the total noise. Johnson noise occurs when free charge carriers are generated due to thermal excitation. Shot noise is associated with statistical fluctuations in the discrete events of photon absorption/carrier excitation, making it more important for lower optical intensity applications. Flicker noise is due to surface traps and the random effects they incur. Flicker noise typically exhibits 1/f behavior, especially at lower frequencies and is thus often referred to as 1/f noise.

All these sources of noise are independent of each other and can be added together to give the total noise. The figure of merit associated with total noise is noise-equivalent-power (NEP) which gives the incident root mean square (rms) optical power in a 1-Hz bandwidth necessary to produce a signal-to-noise ratio of one. This can be thought of as minimum detectable light power, which leads us to our last figure of merit, detectivity ( $D^*$ ), which is equivalent to the signal-to-noise ratio when electromagnetic radiation with power of one watt is incident on a 1 cm<sup>2</sup> device while noise is measured over a bandwidth of 1-Hz:

$$D^* = \frac{\sqrt{AB}}{NEP} \quad (12)$$

where A is device area and B the bandwidth. Detectivity has units of cm-Hz<sup>1/2</sup>/W and is normalized to area because noise is typically proportional to the square root of the device

area. Detectivity is dependent on a device’s sensitivity, spectral response, and noise, making it a function of wavelength, modulation frequency, and bandwidth.

Figures of merit for several state-of-the-art photodetectors based on various materials are provided in Table 1. While these values are representative of commercially available products for some technologies (Si, GaAs, Germanium), photodetectors based on organohalide lead perovskite and CdTe are currently limited to lab-scale devices and testing. Values for photodetectors in the former case are representative of average manufacturable values, while those for the latter are more indicative of highest-reported values found in literature.

**Table 1: Typical values of commercially available (Si, GaAs, Germanium), and lab-scale (CdTe, perovskite) photodetectors.**

Semiconductor	Bandgap	Spectral range	Responsivity	Response time	NEP	Cost
Si <sup>31</sup>	1.1 eV Indirect	600-1100 nm	0.5 A/W	5-10 ns	0.01-0.1 pW/Hz <sup>1/2</sup>	\$250-400 USD
GaAs <sup>32</sup>	1.4 eV Direct	350-950 nm	0.5 A/W	30 ps	35 pW/Hz <sup>1/2</sup>	\$1000-2500 USD
CdTe <sup>33-35</sup>	1.5 eV Direct	400-800 nm	0.4 A/W	10 s	10 <sup>-20</sup> W/Hz <sup>1/2</sup>	N/A
Germanium <sup>36</sup>	0.7 eV indirect	800-1700 nm	0.7 A/W	1-2 ns	0.7 pW/Hz <sup>1/2</sup>	\$500-1000 USD
Organohalide lead perovskites <sup>37</sup>	1.4 – 2.2 eV Direct	300 – 900nm	320 A/W	<10 μs	4.2 pW/Hz <sup>1/2</sup>	N/A

## 1.6 Photolithography

Photolithography is a process used to pattern areas of thin films or substrate bulk to create more complex semiconductor devices. Typically, geometric patterns are transferred from a photomask to a light-sensitive layer of photoresist on the sample.

Chemical treatment of exposed photoresist engraves the mask pattern into, or allows patterned deposition of new material onto, the sample. This process can be repeated many times with different masks to create multiple patterned layers, resulting in devices capable of performing higher level functions.

Aligners are instruments used in optical lithography to expose photoresist coated samples to reproduce a mask image in a particular layer, as well as to align that layer with other patterned layers. There are two main types of aligners commonly used in modern photolithography, contact and projection printers.<sup>38</sup> Contact printers are the simplest type of aligners, making them much less expensive than projection systems which typically require high-precision, large optical pieces. Projection aligners are typically not found in academic research labs, making further discussion of these systems beyond the scope of this work.<sup>39</sup>

Although contact aligners can inexpensively produce fairly small size features, they provide opportunity for significant levels of defect generation due to hard contact between wafer and mask. Proximity printers, a subclass of contact printers offer similar imaging capabilities while drastically reducing defect generation. Proximity printing systems use a gas buffer that allows the photomask to float between 10-50  $\mu\text{m}$  above the resist-coated sample. The major disadvantage with proximity aligners is a reduction in resolution.

Resolution is one of three main measures of an aligner's performance. The resolution of an aligner dictates the minimum feature size that can be produced. Resolution is largely dependent on photoresist technology and is not a fixed value for each machine.<sup>40</sup> Resolutions are typically reported as a minimum feature size which can

be resolved while maintaining a specified feature tolerance. Registration, the second aligner performance metric, is a measure of overlay accuracy between layers.

Commercial fabs typically have fully automated systems, allowing for higher levels of registration, limited only by the system's ability to identify alignment markers and wafer/mask uniformity. Academic research labs typically require manual alignment which introduces significant opportunity for operator error. The last of the three main figures of merit for aligner performance is throughput, or an instrument's ability to quickly pattern wafers while maintaining alignment and feature tolerances.

Contact and proximity aligner systems typically use mercury arc lamps as the optical source for exposure purposes. Although not state of the art, mercury arc lamps are cost-effective, reliable, and well understood.<sup>41</sup> Most systems filter out all but one single wavelength of the plasma discharge, with g-line and i-line (436 nm, and 365 nm, respectively) systems being most common. For a more detailed discussion of mercury arc lamps and their operation in aligner systems, refer to Stephen A. Campbell's *Fabrication Engineering at the Micro- and Nanoscale*.<sup>42</sup>

Another significant component of photolithography is the photosensitive material, photoresist, often referred to simply as resist. Most commonly, photoresists are categorized by their polarity. After exposure, resist coated samples are immersed in a developer solution. Positive resists react in developer such that exposed regions dissolve quicker than regions shielded by the photomask. Negative resists respond oppositely when developed, *i.e.* exposed regions are unaffected while masked regions dissolve. Typically, positive photoresists have higher resolutions than their negative counterparts.

Most commercial photoresists are comprised of a base resin material, a

photoactive compound (PAC), and a solvent. The solvent component of photoresists keeps the resist in a liquid state, and controls the overall viscosity, a major factor for determining photoresist film thicknesses. Figure 8 shows film thickness dependence on spin speed for several common, commercially available resists.

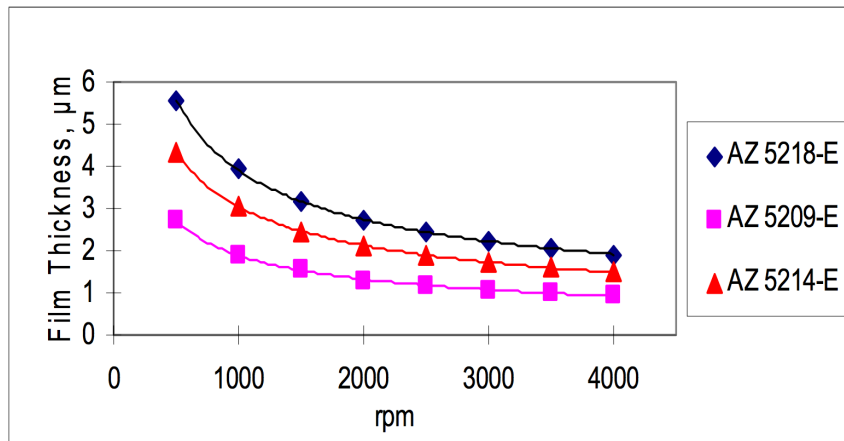


**Figure 8: Photoresist film thickness dependence on spin speed**

For positive photoresists, prior to exposure, the PAC acts as an inhibitor, limiting the resist's solubility in the developer solution. Once exposed, the PAC becomes a sensitizer, increasing the resist's solubility in the developer. The two most important photoresist performance metrics are resolution and sensitivity. Resist sensitivity determines the exposure energy necessary to fully convert the PAC from inhibitor to sensitizer. Photoresists with higher sensitivities will undergo this change more rapidly, reducing exposure time, thus increasing throughput. Resolution is a measure of the smallest feature size which can be reproduced with an acceptable tolerance in the resist. Like aligner resolution, resist resolution bears considerable uncertainty.

Two of the main compounds found in photoresists are classes of carbon-based compounds: aromatic rings and long-chain polymers. Aromatic rings are planar hexagonal structures consisting of six carbon atoms. Benzene, the simplest of aromatic

ring has a one hydrogen atom bonded to each of the carbon atoms. Simple variations made to a benzene ring allow for creation of a wide variety of compounds, such as carboxylic acid, which is particularly important when considering positive photoresists. Carboxylic acid is formed when a carboxyl group (COOH) is added to a benzene ring. Polymers are made from linking together many smaller molecules known as monomers. Many polymers are carbon based due to carbon's ability to easily bond to itself. Polyethylene, the simplest polymer, consists of CH<sub>2</sub> monomers linked in a long chain. Polymers can also be branched chains or cross-linked. Branched chain and cross-linked polymers are typically stronger and less soluble. When considering positive resists, exposure of the PAC results in polymer chain scission, making the polymer more soluble in the developer solution. For negative resists, exposure induces polymeric cross-linking, making exposed regions less soluble in developer solution.

A class of compounds known as DQN have shown significant use in positive photoresists. These resists contain diazoquinone (DQ) and novolac as photoactive compound and resin, respectively. Although not current state of the art, DQN is a dominant formulation for i-line and g-line exposures. A significant advantage of DQN resists is unexposed areas undergo almost zero change in the presence of developer solution, which allows the resist to maintain sharp resolution. Another advantage results from the resin (novolac) being a long chain aromatic ring, making the resin significantly more resistant to chemical degradation. As a result, the photoresist pattern can be utilized as a mask for subsequent plasma or chemical etching.

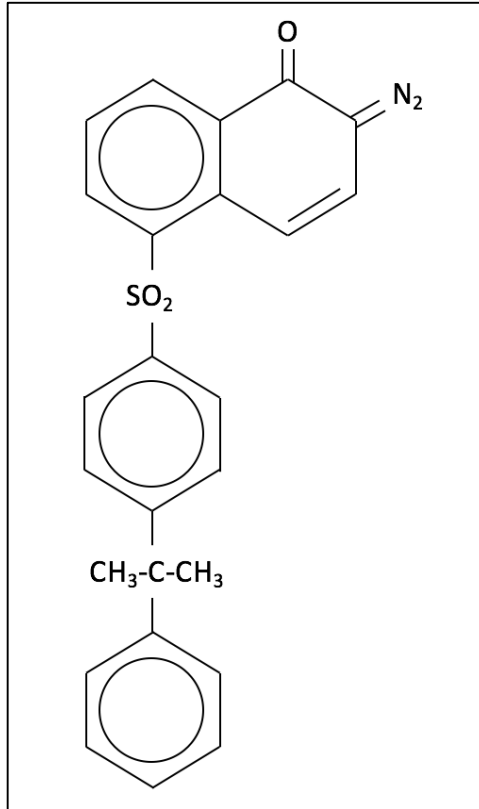


**Figure9: Diazoquinone (DQ), one of the most common photoactive compounds in i-line and g-line exposure resists.**

Typically, negative resists undergo polymeric cross-linking during exposure. This cross-linking makes the large resin molecules attach to each other, becoming larger, and denser, making them less soluble in the developer. Although negative resists have very high photo-speeds and superior adhesions, they are more prone to swelling, which hinders resolution. Another common problem associated with negative resists is formation of pinholes.

Depending on what photoresist is being used, as well as its thickness, determines exposure parameters. Both under-, and over-exposure can result in a variety of issues, from resolution degradation to complete removal of photoresist, *etc.* Therefore, it is necessary to know proper exposure conditions, which are usually provided by photoresist

manufacturers in the form of dose to clear (DTC) swing curves. An example of a DTC swing curve is shown in Figure 10.

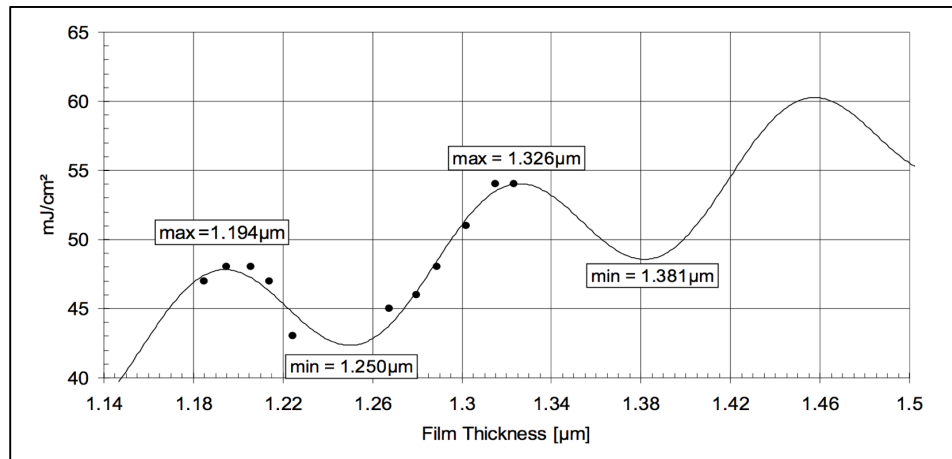


**Figure 10: Dose to clear swing curve for AZ5214-E photoresist**

Following exposure, a developer solution is utilized to remove regions that have (positive resist) or have not (negative resist) been exposed, leaving the desired pattern on the sample. At this point, it is possible to deposit a patterned layer of new material on top of the sample, or to etch away exposed regions of the sample. Both cases are followed by removal of remaining resist, usually through use of 1-Methyl-2-pyrrolidone (NMP) solvent. Typically, a sample will undergo multiple cycles of photolithographic processing, complex integrated circuits typically require samples to undergo photolithographic processing up to 50 times throughout the duration of the entire fabrication process.

Without photolithographic processing, fabrication of complex integrated circuits (ICs) would not be possible. In some instances, patterning of ultra-high precision nano-scale features is achieved through electron beam patterning. However, compared to traditional photolithography, E-beam patterning is much more expensive and time

consuming. The ability to create complex micron, and sub-micron level structures allows for exploitation of unique electrical properties that are not typically present in uniform (non-patterned) thin films. Typically, a very complex, precise process, photolithography accounts for a significant portion of modern semiconductor device fabrication expenses. High costs and significant maintenance requirements of traditional photolithographic patterning equipment continue to encourage researchers to develop cost-effective alternatives. These alternative patterning techniques are collectively referred to as soft lithography.

Although photolithography is well developed and effective in patterning inorganic semiconductor devices, its utilization of solvents limits its applicability to perovskites. Standard photoresist developers attack organic constituents of perovskites, causing decomposition to occur before films can be effectively patterned. Soft lithography techniques have shown limited capabilities to pattern perovskite films. A common approach for organic semiconductor patterning *via* soft lithography is to utilize a rigid mold, or template, during growth of perovskite films. Micromolding in capillaries (MIMIC) and template-assisted spin-coating are two such methods.

Micromolding in capillaries is capable of producing line or stripe-like patterns in perovskite films.<sup>43</sup> When solvated precursors are applied to a substrate with a capillary containing mold on top, the solutions wick through the mold under the influence of capillary action. Upon removal of solvent(s) and mold, the resulting perovskite film will retain the straight-line pattern design of the mold. This process results in comb-like features, with regions of patterned perovskite stripes, separated by void areas where no perovskite is present. Stripes are connected to each other by a section of uniform

perovskite film, where no mold was present during film growth. A relatively straightforward method for patterning perovskites, MIMIC is largely limited to simple line geometries.

Template-assisted spin coating is a similarly easy patterning technique, and, as such, has limitations in the associated geometries which it can produce. A recent effort shows the ability to create an inverse-opal (IO) structure in perovskite films through template-assisted spin coating.<sup>44</sup> In this procedure, a monolayer of polystyrene microspheres was placed on top of the substrate during spin-coating of precursor solutions. Following perovskite film growth, the polystyrene spheres are dissolved in toluene. Variations in sphere diameter cause unique differences in optical and electrical properties of resulting patterned perovskite films and associated devices.

While processes such as MIMIC and template-assisted spin coating offer cost-effective alternatives for patterning of materials, such as perovskite, that are unable to survive traditional photolithographic processing, they provide little commercial viability due to limitations in geometries which they can effectively pattern. Another effort, a modified focus ion beam (FIB) etching process, is beginning to show greater capabilities in high-resolution patterning of more complex features in perovskite films.<sup>45</sup> Unfortunately, this process is much more complicated and requires exotic, hazardous materials, such as  $\text{XeF}_2$ , to reduce damage caused to perovskite films during FIB exposure. A fledgling technology, perovskite thin films have received few other considerations for patterning purposes.

Orthogonal photolithography is a process used for patterning materials, such as perovskite, which are not compatible with traditional photoresist developers. This

procedure utilizes photoresists and developer solutions that are chemically orthogonal to compounds that typically can't be patterned through traditional lithography. Specialty resists and highly fluorinated solvents, such as OSCoR1000 negative photoresist, HFE7300 developer, and HFE 7100 stripper, are chemically orthogonal to perovskite films, which allows for high-resolution patterning of perovskite thin films without inducing significant decomposition.<sup>6</sup> Although orthogonal photolithography does little to combat high costs associated with traditional lithography, it allows for production of perovskite thin films possessing high-resolution, complex patterning using traditional photolithography equipment, which is standard in almost all semiconductor device fabs.

## 2. METHODS

Now that we have introduced properties of photodiodes, perovskite crystal structures, and hybrid photodetectors, we proceed by discussing device fabrication, from materials preparation through device completion and testing; as well as characterization techniques used in this study. Optimized fabrication parameters will be given in this discussion, with a discussion concerning optimization efforts given in the following chapter. Multiple instruments and techniques were utilized throughout this study to determine film parameters such as thickness, uniformity, crystal structure, grain size, roughness, *etc.* Other characterization processes, such as J-V and EQE measurements, focus on device characterization.

### 2.1 Device Fabrication

While most materials used in this study are commercially available, it was necessary for us to synthesize MAAC ourselves, as it was not commercially available. To synthesize MAAC, we connect two flasks with a chemical column filled with sodium hydroxide (NaOH), making a closed system as shown in Figure 11. In one flask, we add 10 ml acetic acid and 200 ml toluene. Next, we add 200 ml methylamine and approximately 20 tablets of NaOH to the other flask. Using magnetic stir bars in each flask, we stir both sides at full speed and begin to open all valves in the system starting on the side with flask containing methylamine and NaOH. Shortly after, bubbling starts to occur in the flask containing acetic acid and toluene and a cloud of vapor forms over the liquid. This process is let run until bubbling stops, at which point, more NaOH or methylamine is added to the other flask to continue bubbling. Continue this process until MAAC precipitation occurs in acetic acid and toluene containing flask. Reaction

completion occurs when no acetic acid remains in this flask, which we test using pH paper. Once no acetic acid remains, we stop the process, dispose of remaining NaOH and are left with MAAC.

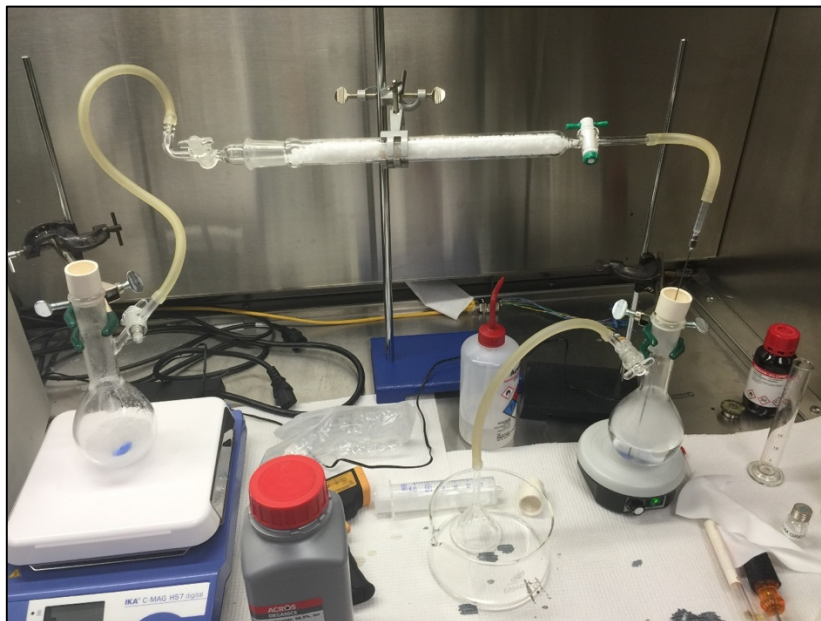


**Figure 11: Setup of equipment used for MAAC synthesis.**

We start by cleaning glass substrates with thin, patterned films of indium tin oxide (ITO), the ITO pattern can be seen in Figure 12. Substrates undergo a ten-minute ultrasonic bath using a solvent solution consisting of 475 ml deionized water and 25 ml Deconix OP121 detergent. Following this ultrasonic bath, substrates undergo ten additional minutes of sonication in deionized water (DI H<sub>2</sub>O) and are dried using a CO<sub>2</sub> gun. Once dry, substrates are placed in a pressure chamber where they are subjected to seven-minutes and thirty-seconds of oxygen plasma (Harrick Plasma, Pdc-32G) as the last step of the cleaning procedure. After cleaning, we grow a hole transport layer by applying 200  $\mu$ l of filtered poly(3,4-ethylenedioxythiophene) polystyrene sulfonate (PEDOT:PSS), allowing it to sit for thirty-seconds and then spinning at 4000 rpm for

thirty seconds. Substrates are then annealed at 145 °C for ten-minutes.

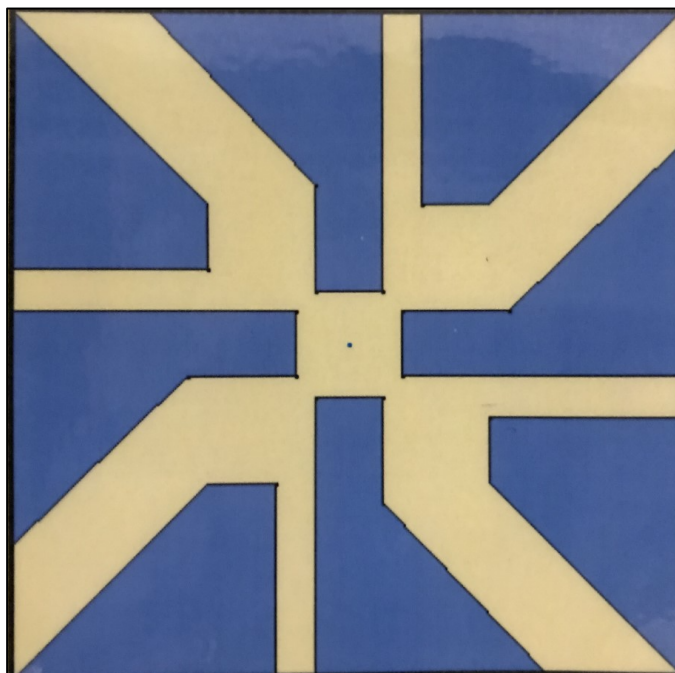


**Figure 12: ITO (blue) pattern on glass substrates.**

We then move to a wet nitrogen glovebox for perovskite film growth using a two-step deposition method. 85  $\mu\text{l}$  of 1.2 molar  $\text{PbI}_2\text{-MAAc}$  in DMF is applied and spun at 2500 rpm for sixty-seconds. Samples then sit for ten-minutes before undergoing an application of 300  $\mu\text{l}$  MAI in IPA at a concentration of 60  $\mu\text{g}/\mu\text{l}$  to fully cover the sample surface. After sitting for 30 seconds, these samples are spun at a speed of 4000 rpm for 40 seconds. Following this deposition, samples sit in the glovebox for six-minutes before being transferred to the fume hood or humidity control chamber where they are annealed at 100 °C for thirty-minutes at a relative humidity of 30%. After annealing, samples are transferred back to the wet glove box for  $\text{PC}_{70}\text{BM}$  deposition.  $\text{PC}_{70}\text{BM}$  in chlorobenzene is heated to 70 °C to allow complete solvation. 50  $\mu\text{l}$   $\text{PC}_{70}\text{BM}$  in chlorobenzene at a concentration of 20  $\mu\text{g}/\mu\text{l}$  is spun at 1500 rpm for forty-seconds, followed by twenty-

minutes annealing at 80°C.

Next, we move to a dry nitrogen glove box, where we start by scratching away contact areas (Figure 13). Once contact areas are removed, samples are loaded into a Trovato evaporator for bathocuproine (BCP) and aluminum (Al) deposition.

Approximately 75 Å BCP is deposited through an organic layer mask at a rate of 1 Å/s.

The organic layer mask is then changed to a contact mask and 1000 Å aluminum is deposited at a rate of 2 Å/s.

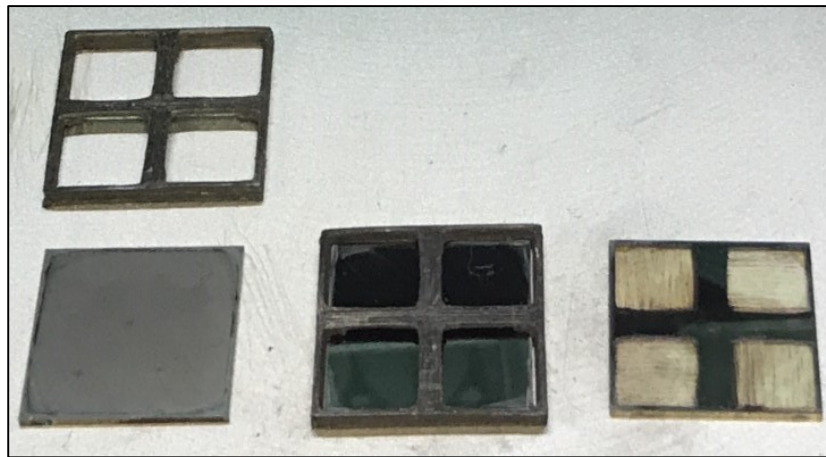


**Figure 13: From left to right, perovskite sample and template, template over perovskite sample, and scratched perovskite sample.**

Samples are then capped inside the dry glove box using a recessed glass cover and UV-curable epoxy adhesive (capping set-up shown in Figure 14).

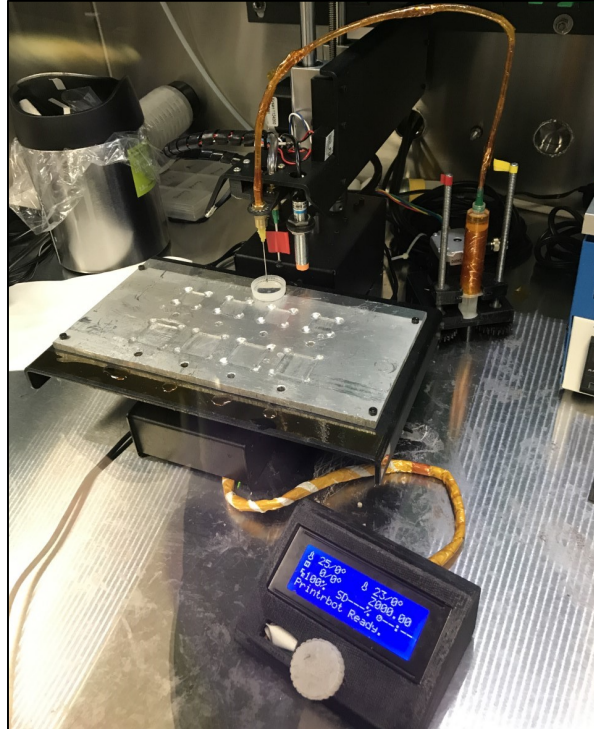


**Figure 14: 3-D printer converted into capping instrument for perovskite devices.**

We finish our fabrication procedure by moving our devices to the fume hood where exposed edges are stripped of remaining films and coated with silver paint as shown in Figure 15.

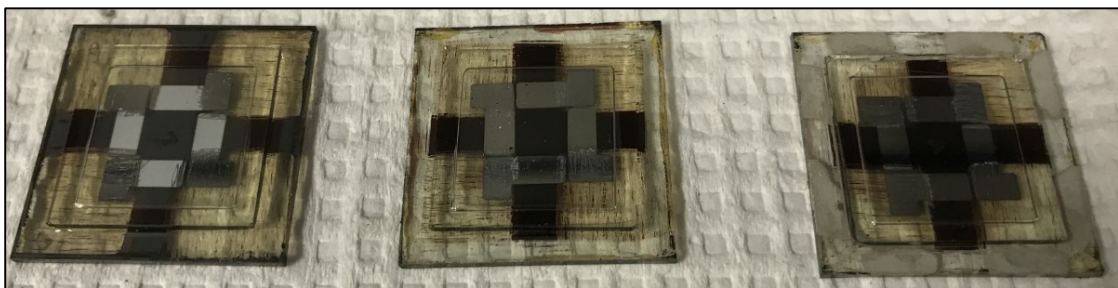


**Figure 15: From left to right, capped perovskite sample unaltered, with edges scratched off, with silver paint applied.**

In our efforts to pattern perovskite films, we follow the previously noted device fabrication procedure through perovskite film annealing step. To create patterned devices, we apply OSCoR1000 negative photoresist, via spin coating, to annealed perovskite films. After photoresist application, we initiate a pre-exposure bake for 1 minute at 90 °C. This bake is followed by a selective exposure to broadband UV light ( $90 \text{ mJcm}^{-2}$ ) using a SuSS MJB4 Contact Mask Aligner (Figure 16). A 1 minute, 90 °C post-exposure bake is then followed by resist development in HFE7300 for 5 minutes. To transfer mask pattern from resist to perovskite film, we expose resist-unprotected regions of perovskite film to a reactive ion etch (RIE) with  $\text{SF}_6$  plasma for 1 minute (pressure 40 mTorr, 750 W AC (ICP) + 75 W DC (RIE) bias) using an Oxford ICP-RIE Plasmalab 100 (Figure 17). Regions with no protection from the photoresist transform into insulating  $\text{PbF}_2$ , while regions protected by the resist are unaffected. Our final step, following pattern transfer, is to strip the remaining photoresist from our patterned film using HFE7100. Figure 18 provides a visual step-by-step representation of our patterning process, as well as an optical micrograph which depicts a patterned region of perovskite film.

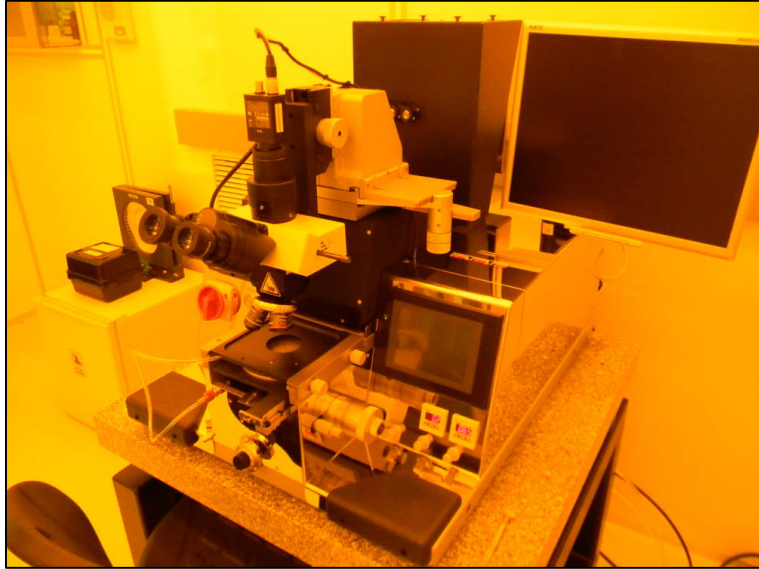


**Figure 16: SuSSMJB4 Contact Mask Aligner**



**Figure 17: Oxford ICP RIE Plasmalab 100**

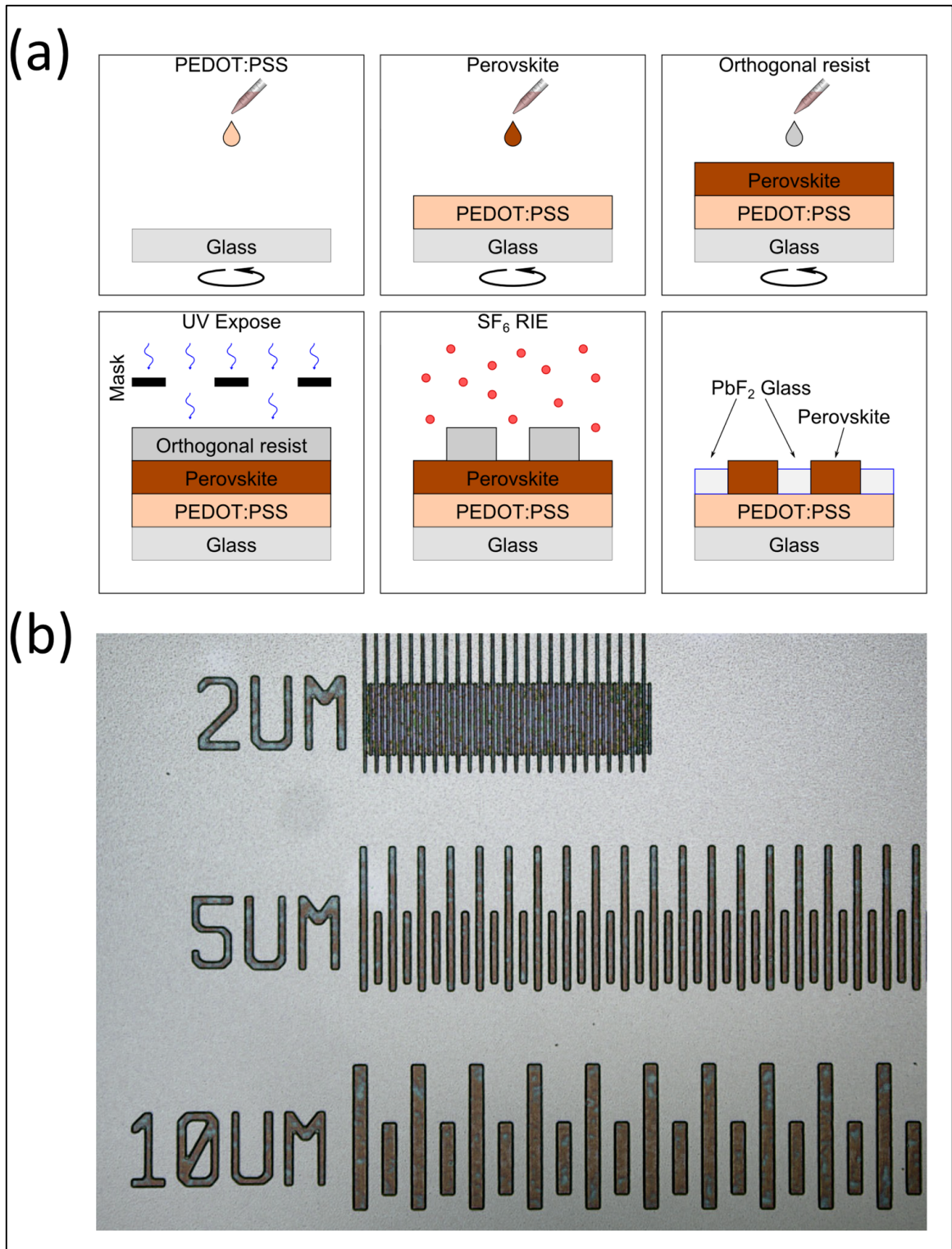


Figure 18: (a) Principle scheme of photolithographic patterning of  $\text{CH}_3\text{NH}_3\text{PbI}_3$  films. (b) Optical micrograph of patterned perovskite film. Clear field corresponds to unprotected areas of resist.

## 2.2 X-Ray Diffraction

X-ray diffraction is widely used in the study of crystal structures due to similarities in x-ray wavelengths ( $10^{-2}$  to 10 nm) and spacing of atoms and planes in crystal lattices. In 1913, it was discovered that a three-dimensional crystal lattice can behave similarly to a diffraction grating, yielding intensity peaks of transmitted x-rays dependent on wavelengths and incident angles. This phenomenon is described by Bragg's Law, which describes intensity maxima as a condition of incident angle, and is given by:

$$2d \sin \theta = n\lambda \quad (13)$$

where  $d$  is interplanar or atomic spacing,  $\theta$  is angle of incidence,  $n$  is an integer, and  $\lambda$  is the wavelength.

X-ray diffraction can be used to determine a myriad of crystal structure and thin film characteristics. However, we use x-ray diffraction in this study to determine formation of  $\text{CH}_3\text{NH}_3\text{PbI}_3$  from  $\text{CH}_3\text{NH}_3\text{I}$  and  $\text{PbI}_2$ , as well as detection of  $\text{PbI}_2$ . The presence of  $\text{PbI}_2$  indicates one of two possibilities: either incomplete reaction, or perovskite degradation. Being a layered crystal structure, lead (II) iodide possesses a unique diffraction pattern with peaks that do not overlap with those seen in the diffraction pattern associated with  $\text{CH}_3\text{NH}_3\text{PbI}_3$ . We utilize x-ray diffraction to confirm full perovskite crystallization, as well as to study if, and how, MAAC affects the perovskite crystal orientation. X-ray diffraction is also used to confirm conversion of perovskite into  $\text{PbF}_2$  as a result of our orthogonal photolithographic patterning process.



**Figure 19: Rigaku SmartLab X-Ray Diffractometer.**

In this study, we perform x-ray diffraction measurements using a Rigaku SmartLab X-Ray Diffractometer (Figure 19). Due to difficulty in making single-crystal perovskite samples, we utilize the Bragg-Brentano powder diffraction setting. Powder x-ray diffraction is useful when dealing with polycrystalline samples with random orientations. During operation, diffracted x-rays are measured while the sample is fixed and the source and detector arms are varied. A schematic representation of this operation is shown in Figure 20. Results are presented in plots of normalized, or relative, intensity (x-ray counts) vs. measurement angle ( $2\theta$ ).

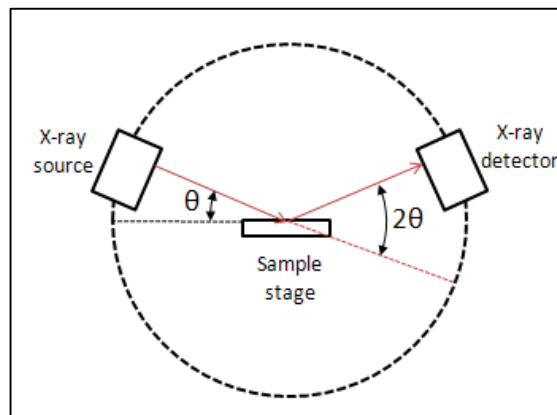


**Figure 20: XRD operation schematic.**

### 2.3 Scanning Electron Microscopy

To gain a more complete understanding of perovskite film properties, we employ scanning electron microscopy (SEM) which has resolution high enough to study surface grain size and boundaries. In addition to ultra-high resolution imaging, the SEM is capable of 45 & 90° cross-sectional imaging. These capabilities, coupled with an energy dispersive x-ray analysis (EDX) unit, allow us to more fully characterize surface and bulk perovskite morphologies, as well as elemental composition. Scanning electron microscopes utilize a focused electron beam which interacts with the atoms of samples being investigated. Typically, the electron beam moves in a raster pattern, while a detector collects electrons emitted/scattered by atoms of the sample. The microscope combines beam position and information from the detector to produce a high-resolution image of the sample. Although some SEMs use multiple receivers to detect other signals such as reflected electrons, X-ray photons, current absorbed by the sample, or transmitted electrons, secondary electron detectors are standard in most SEMs.

When dealing with semiconducting materials, SEMs offer a unique advantage for studying optoelectronic properties, due to beam electrons injecting charge carriers into the semiconductor. High energy electrons from the SEM lose energy when they excite electrons from the valence band to the conduction band. Direct band-gap semiconductors, such as organohalide lead perovskites, are subject to cathodoluminescence when electron-hole pairs, generated by the electron beam, recombine. When beam electrons interact with a sample, they can excite characteristic x-rays. These characteristic x-rays can be detected and analyzed through EDX, which allows us to map the distribution and abundance of elements in the sample.

We utilize a Helios NanoLab 400 scanning electron microscope (Figure 21) to study surface grain sizes and boundaries through high-resolution imaging. In addition, we make use of the NanoLab's cross-sectional imaging and EDX capabilities to provide a more complete understanding of perovskite film morphology and composition. Due to high energies associated with the electron beam, it is rather difficult to properly image perovskite films before degradation rapidly alters the sample. To circumvent this issue, we drop the output current drastically, focus on one area of the sample to achieve a sharp image, move the beam to an unaffected area still in focus, and then begin the imaging process.



**Figure21: FEI Helios NanoLab 400 Scanning Electron Microscope.**

## **2.4 Atomic Force Microscopy**

Atomic force microscopy has proven invaluable in thin film semiconductor characterization. Through use of mechanical probe, an atomic force microscope (AFM) can provide detailed nano-meter scale analysis for a wide range of sample characteristics such as: adhesion, friction, hardness, topography, surface potential, *etc.* AFM operation

does not necessitate use of complex lenses or beam irradiation common to optical and electron microscopes. Therefore, AFMs are not limited in resolution by aberrations or diffraction limits, nor do they pose as high a risk of sample alteration due to high beam energies.

AFMs operate by measuring force between a cantilever mounted probe and sample. When the probe is near the sample's surface, forces between tip and surface cause cantilever deflection. Imaging resolution is achieved by measuring vertical and lateral deflections of the cantilever. Cantilever deflections are measured by reflecting a laser off the cantilever to a spatially sensitive photodetector, as shown in Figure 22. A variety of forces (van der Waals, capillary, electrostatic, mechanical contact, *etc.*) can be attributed to this deflection. In most cases, a feedback loop is used to maintain a constant force interaction between probe and sample. In addition to the variety of forces that can cause cantilever deflection, there are multiple imaging modes that can be chosen: static (contact), tapping, and frequency modulation (non-contact). The mode of operation used dictates feedback loop input.

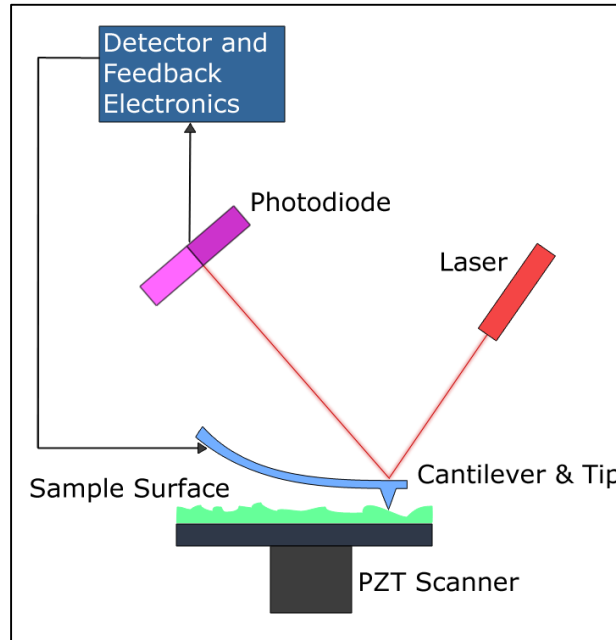


**Figure 22: Block-diagram depicting cantilever deflection.**

When operating in static mode, the tip or sample is raster scanned in the xy-plane with feedback input being cantilever deflection. During this process, the feedback loop output controls the distance between probe and sample, continuously adjusting to variations from surface contours to maintain constant deflection. In tapping mode, the cantilever is made to oscillate at, or near, its resonant frequency. When the probe tip is brought close enough to the sample, interaction forces cause changes in the amplitude of oscillation. As scanning occurs, the feedback loop adjusts cantilever height relative to the sample's surface to maintain constant amplitude of oscillation. Tapping mode is generally favored over contact mode due to a reduction in damage done to the surface of the sample by shortening the duration in which an applied force is necessary. Similar to tapping mode, non-contact imaging requires the cantilever to be driven to its resonance frequency, while the feedback loop adjusts the relative distance between probe and surface to maintain constant amplitude or frequency of oscillation.

In this study, we perform measurements with an AIST-NT SmartSPM atomic force microscope, shown in Figure 23. With a fully automated 1300 nm IR laser photodiode alignment, 100  $\mu\text{m}$  piezo sample scanning range, and multiple force modes (electrical, electrochemical and piezo), this AFM provides for rapid, high-resolution imaging. We rely on this instrument to provide information regarding perovskite surface uniformity, smoothness, and quality.

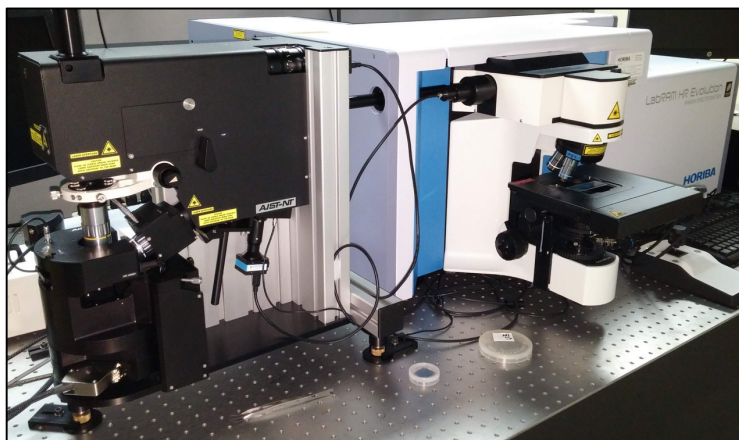


**Figure 23: AIST-NT SmartSPM Atomic Force Microscope.**

## **2.5 Profilometry**

In our device optimization efforts,  $\text{PbI}_2$ -MAAc and perovskite film thicknesses play critical roles. If perovskite films are too thick, charge carrier recombination mechanisms limit performance. Films that are too thin, in contrast, are unable to achieve full absorption, and thus performance falls due to inefficient carrier generation. Another issue affected by film thickness is perovskite crystallization. Thicker  $\text{PbI}_2$  and  $\text{PbI}_2$ -MAAc films result in difficulties for complete perovskite crystal formation to occur once MAI is introduced.

In this study, we utilize a surface profilometer to provide rapid and accurate information regarding various film thicknesses. A type of scanning probe microscope

(SPM), surface profilometers offer faster thickness determinations than other SPMs, without sacrificing precision. However, surface profilometers typically cause significant damage to samples during analysis. Although this could be an issue when dealing with exotic materials such as GaN, perovskite samples have such low materials costs and fabrication times that sacrificial samples are not of major concern.

A relatively new addition to the family of metrology equipment at Texas State University, Bruker's DektakXT Stylus Profilometer (Figure 24) provides rapid step-height measurements with angstrom level resolution and high repeatability.

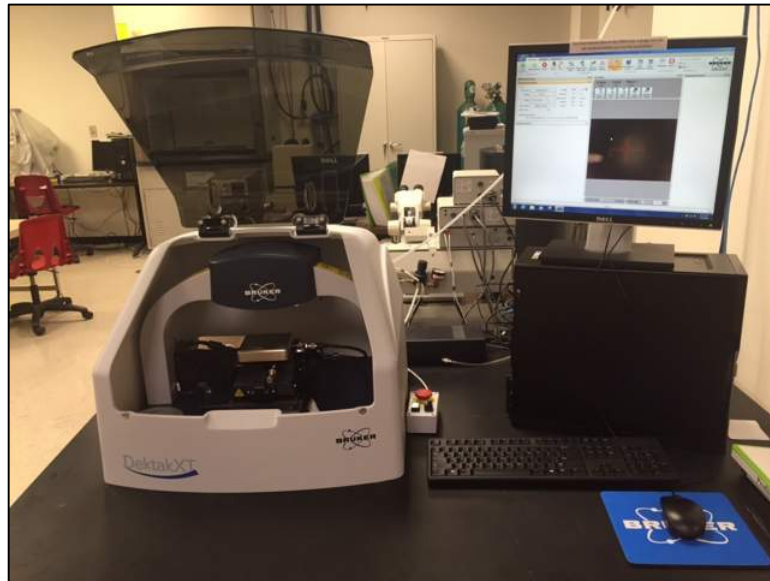


**Figure 24: Bruker DektakXT Stylus Profilometer.**

## **2.6 Current-Voltage Measurements**

Photovoltaic device performance can be characterized by measuring relationships between current, voltage, and power output. Using a solar simulator and simple circuitry, we can apply a variable load to our devices to determine characteristic current-voltage responses. Current-voltage analysis is made using a Keithly 2400 source-measure unit while devices are illuminated using an Oriel ABA solar simulator equipped with an AM

1.5G filter at a calibrated intensity of  $100 \text{ mW/cm}^2$  (Figure 25). We begin our measurements with an applied load of  $-0.1 \text{ V}$ . This voltage is incrementally increased in steps of  $0.1 \text{ V}$ , until maximum bias of  $1.1 \text{ V}$  is achieved. A LabView program measures, logs, and graphs current and voltage at every step. Using the characteristic J-V curves, we can determine factors such as:  $J_{SC}$ ,  $V_{OC}$ , fill factor (FF), and power conversion efficiency (PCE), for our devices. Unfortunately, there exist many factors of this procedure which make its results unreliable.<sup>46</sup> To combat this reliability issue, researchers can have their devices tested and certified at the National Renewable Energy Labs (NREL), however this is a rather time consuming and costly process. Another option to combat reliability issues, is to compare results to external quantum efficiency measurements to verify that efficiencies in each test are normalized to raw device performance.



**Figure25: Current-Voltage measurement equipment.**

## 2.7 External Quantum Efficiency Measurements

Another technique we utilize in this study to more completely and reliably determine device performance is external quantum efficiency (EQE) measurement. A monochromator allows us to see how our devices perform when subject to specific wavelengths of electromagnetic radiation. We use these data, in conjunction with our J-V measurements to gain a more complete understanding of our devices, as well as to confirm performance benchmarks. A xenon arc lamp provides modulated light which is sent through sorting filters and a monochromator, giving a monochromatic light output. This light is then focused to a well-defined area. During measurements, the monochromator scans over a range of wavelengths. In our testing, we scan from 300-850 nm. Figure 26 shows the EQE measurement system utilized in this study.

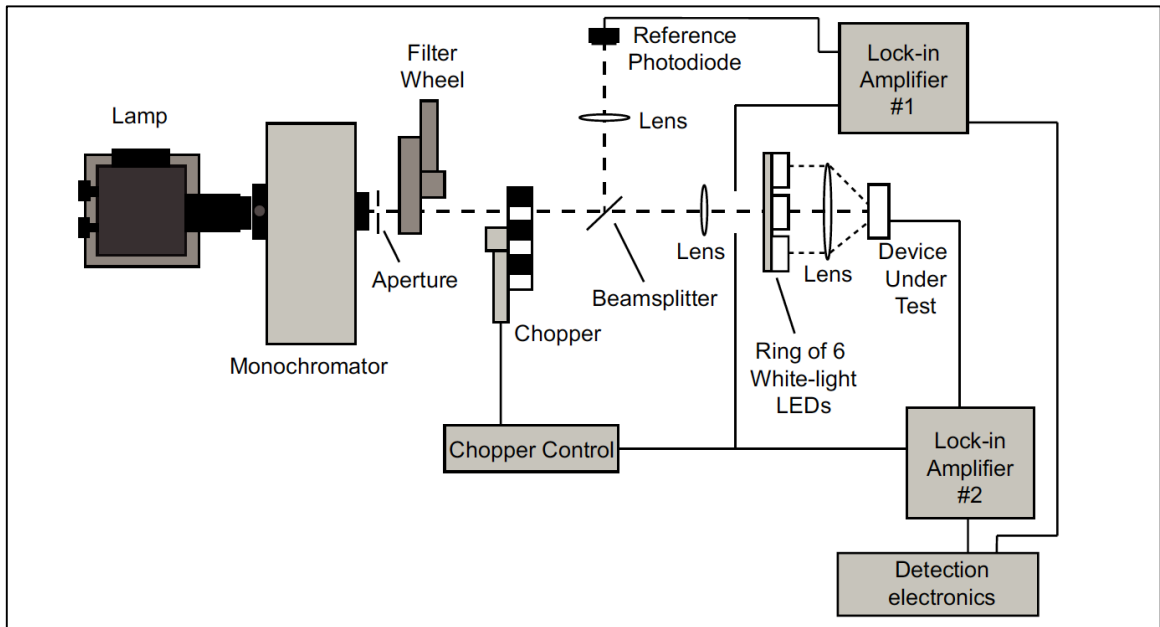


Figure 26: Schematic of external quantum efficiency measurement setup.<sup>47</sup>

### 3. RESULTS

Our initial analysis efforts will cover the individual studies conducted to determine optimal device fabrication conditions and parameters. A chronological presentation of these individual studies will help show how optimization efforts led to our final results. In addition, we will show how these studies compare to similar cases in literature. We will then give a comparative analysis of devices made with MAAC adduct, and those without.

#### 3.1 Device Optimization

Our initial analysis efforts will cover the individual studies conducted to determine optimal device fabrication conditions and parameters. Our initial study towards device optimization tests various ratios of  $\text{PbI}_2$  to MAAC in DMF. As a control, the molar concentration of  $\text{PbI}_2$  in DMF is held at 1.0 M, with the molar concentration of MAAC ranging from 0.8 M to 1.2 M, in increments of 0.1 M. Four devices for each ratio are fabricated and tested under as close to identical conditions as possible. Testing involves a current-voltage analysis of each device subjected to AM1.5G illumination. Average values and standard deviations of power conversion efficiency (PCE), open circuit voltage ( $V_{OC}$ ), short circuit current ( $I_{SC}$ ), and fill factor (FF) for each ratio are provided in Table 2. In addition, Figures 27 and 28 provide further statistical analysis, and current-voltage curves, respectively.

**Table 2: Average values of device PCE,  $V_{OC}$ ,  $I_{SC}$ , and FF for varying ratios of  $PbI_2$  to MAAC.**

Precursor Ratio Study				
$PbI_2$ :MAAc (M)	PCE (%)	$V_{OC}$ (V)	$I_{SC}$ ( $mA/cm^2$ )	FF (%)
1:0.8	5.49±0.36	0.80±0.03	15.00±0.29	45.78±2.28
1:0.9	6.64±0.39	0.83±0.01	15.68±0.72	50.80±2.24
1:1	11.09±0.94	0.96±0.01	18.30±1.07	63.09±2.21
1:1.1	9.85±0.40	0.96±0.01	16.01±0.30	64.08±1.78
1:1.2	6.00±0.90	0.83±0.07	14.73±0.29	49.53±2.06

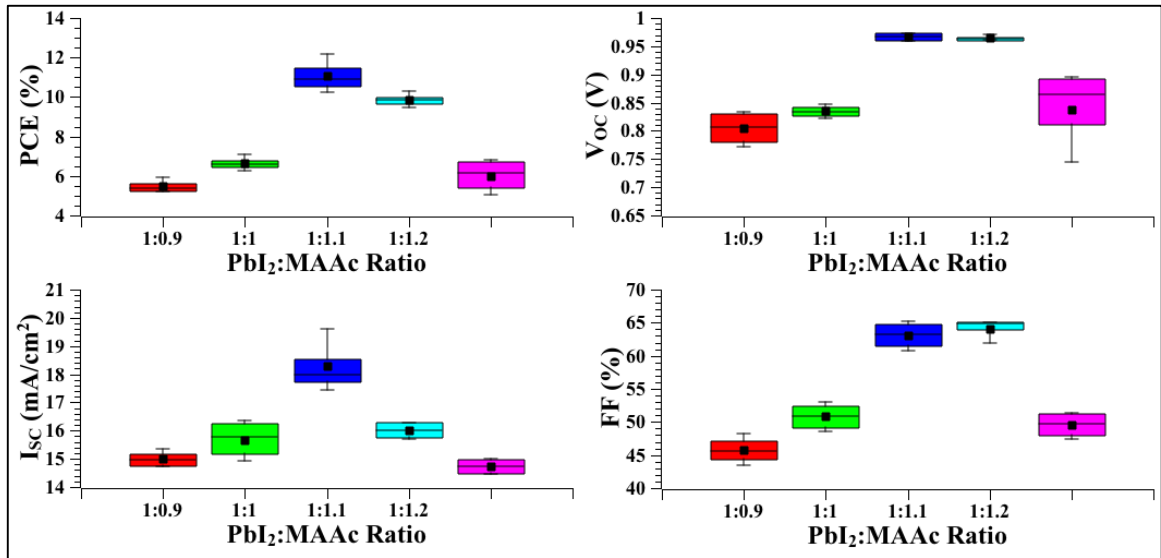


**Figure 27: Statistical analysis of photovoltaic data recorded under AM1.5G illumination for varying ratios of  $PbI_2$  to MAAC.**

As can be seen in Table 2 and Figure 27, there is a clear peak in device performance when a  $PbI_2$  to MAAC ratio of 1:1 is used. We suspect that insufficient levels of MAAC found in devices made with 1:0.8 and 1:0.9 molar ratios create variability in inter-planar spacing of layered  $PbI_2$  throughout the samples. This, in turn, causes less uniform perovskite films to be achieved, thus reducing overall device performance. Similarly, devices made with excess MAAC most probably suffer from non-uniform perovskite films due to excess MAAC, which we suspect causes improper

precursor reaction.

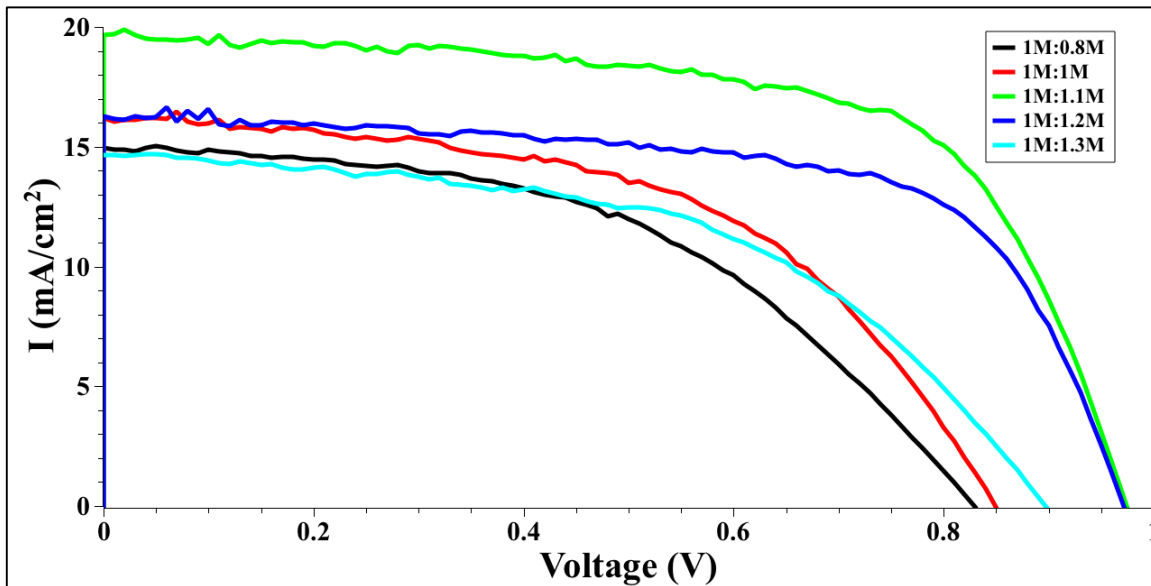
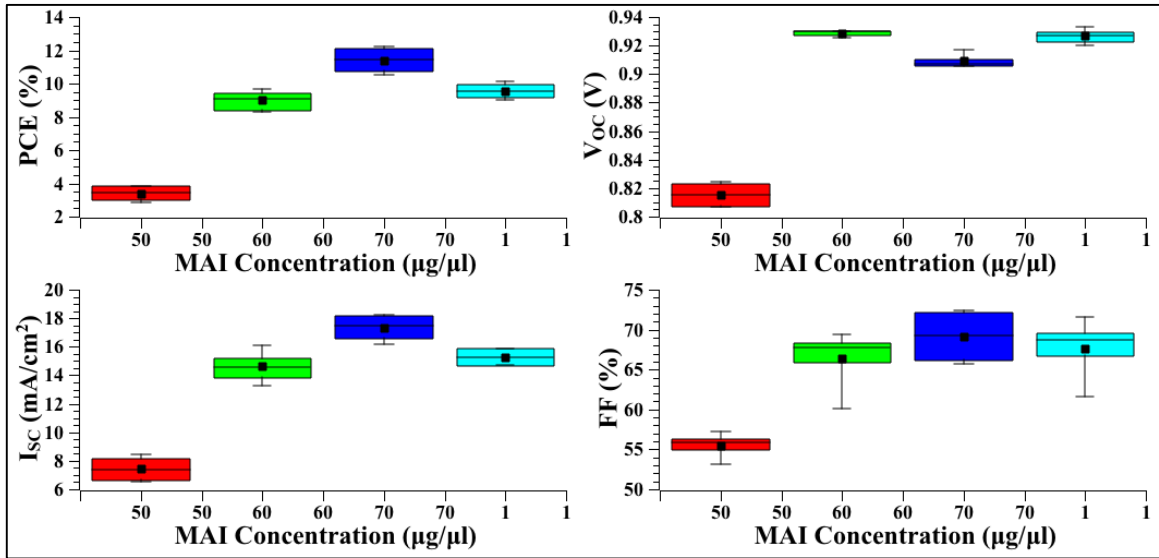


Figure 28: Current-Voltage curves obtained from measurements taken under AM1.5G illumination for devices with varying ratios of  $\text{PbI}_2$  to MAAc.

Our second study varies MAI concentrations, ranging from  $40 \mu\text{g}/\mu\text{l}$  to  $70 \mu\text{g}/\mu\text{l}$  in IPA. As previously noted, a concentration of  $50 \mu\text{g}/\mu\text{l}$  provides optimal results for typical two-step devices fabricated in a similar fashion, minus the addition of MAAc. However, the high level of influence this adduct has on reaction kinetics between MAI and  $\text{PbI}_2$  necessitate further study into MAI concentration to assure full optimization. As with the previous study, devices fabricated with various MAI concentrations are tested under AM1.5G illumination. Results from current voltage analysis of these devices are given in Table 3. In addition, Figures 29 and 30 provide further statistical analysis, and current-voltage curves, respectively. Figure 31 provides results of XRD analysis of samples made with various MAI concentrations, which helps confirm which MAI concentrations provide sufficient perovskite formation without leaving an excess of MAI or unreacted  $\text{PbI}_2$ , which both act to lower device performance.

**Table 3: Average values of device PCE,  $V_{OC}$ ,  $I_{SC}$ , and FF for varying MAI concentrations.**

MAI Concentration Study				
MAI Concentration ( $\mu\text{g}/\mu\text{l}$ )	PCE (%)	$V_{OC}$ (V)	$I_{SC}$ ( $\text{mA}/\text{cm}^2$ )	FF (%)
40	3.39 $\pm$ 0.51	0.81 $\pm$ 0.01	7.44 $\pm$ 0.97	55.45 $\pm$ 1.97
50	9.56 $\pm$ 0.46	0.93 $\pm$ 0.01	15.28 $\pm$ 0.58	67.62 $\pm$ 3.83
60	11.39 $\pm$ 0.85	0.90 $\pm$ 0.01	17.33 $\pm$ 1.07	69.13 $\pm$ 3.66
70	8.99 $\pm$ 0.56	0.93 $\pm$ 0.01	14.61 $\pm$ 1.07	66.37 $\pm$ 3.89



**Figure 29: Statistical analysis of photovoltaic data recorded under AM1.5G illumination for varying MAI concentrations.**

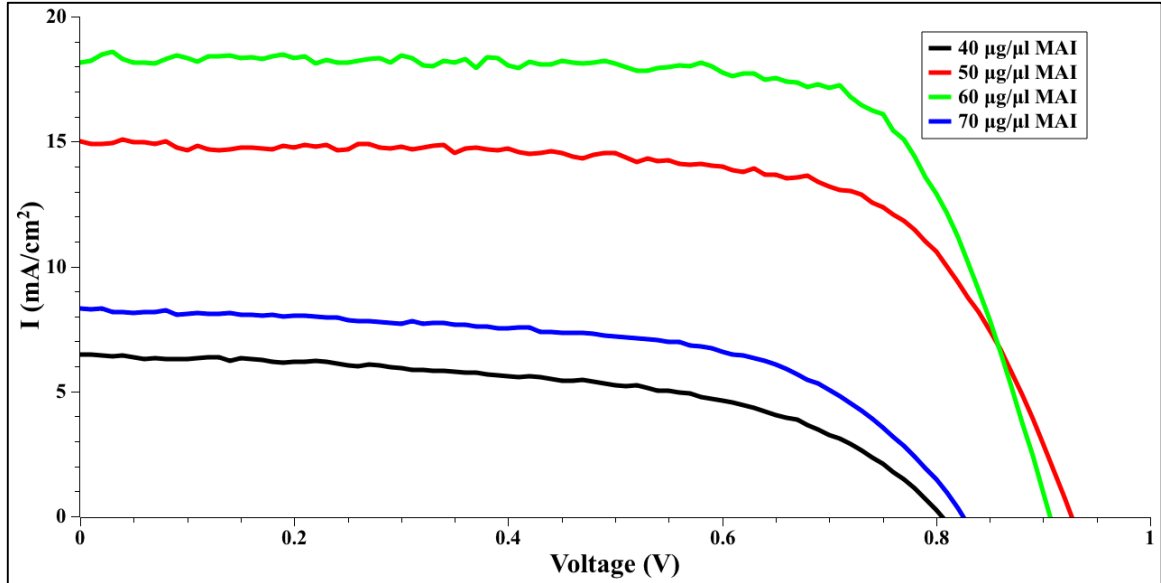


**Figure 30: Current-Voltage curves obtained from measurements taken under AM1.5G illumination for devices with varying MAI concentrations.**

As can be seen in Figure 31, higher MAI concentrations provide perovskite films with no trace of  $\text{PbI}_2$ . Although this is true for samples made with 70 mg/ml concentration MAI, associated device performance shows a drastic decrease when compared to 60 mg/ml, most probably due to excess MAI, which is an electrically insulating material. While perovskite films made with 60 mg/ml MAI show slightly less order when compared to films made with 70 mg/ml MAI, they do show an improvement when compared to films made with 50 mg/ml MAI. Device performances also confirm that an MAI concentration of 60 mg/ml is optimal.

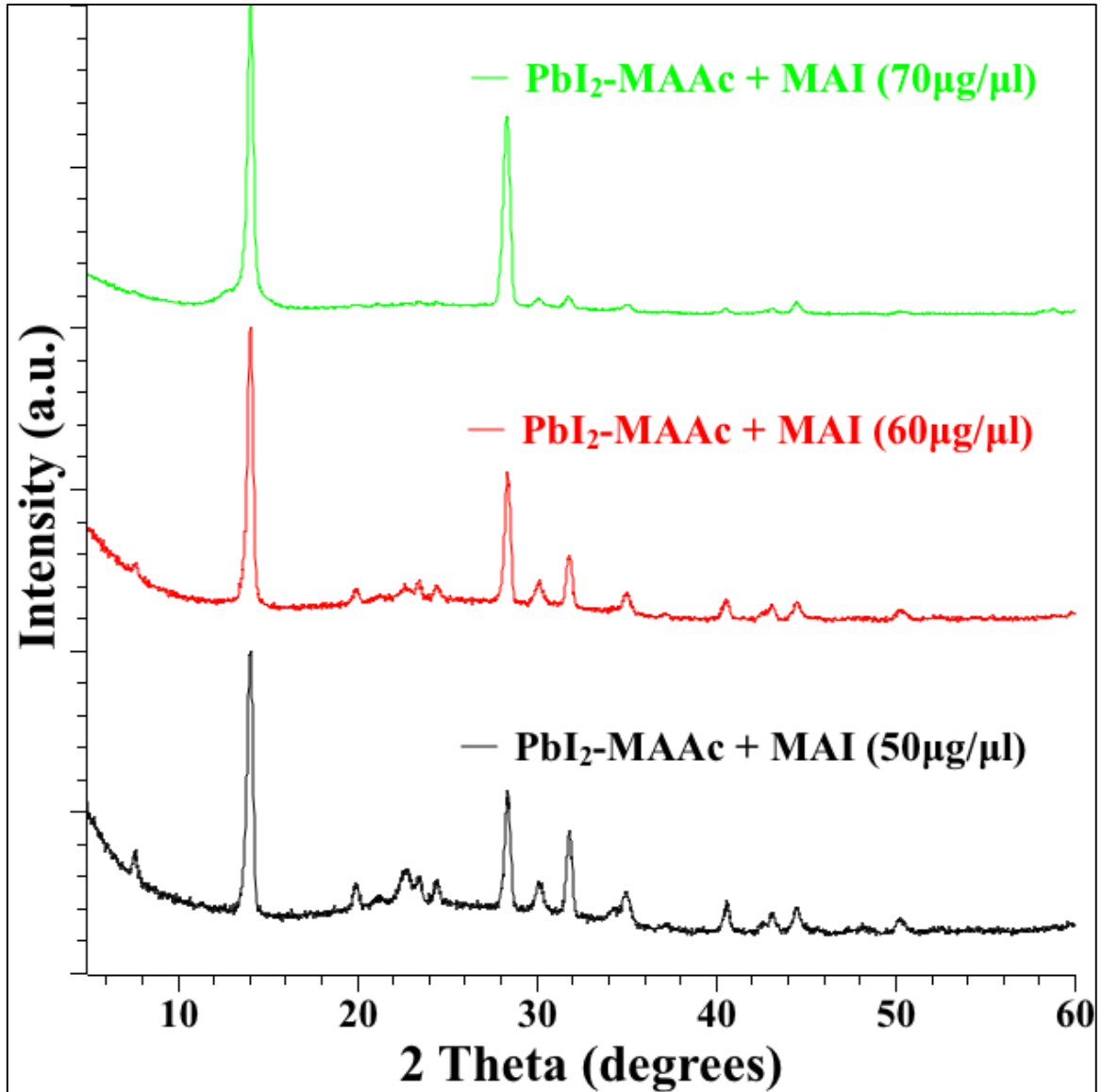


Figure 31: XRD spectra for PbI<sub>2</sub>-MAAc with various MAI concentrations.

Our next optimization efforts focused on humidity levels during perovskite film annealing. Recent studies show improvements in device performance and stability when perovskite films are annealed in ambient air. Using a humidity control chamber, we can fine tune humidity levels for perovskite annealing. In this study, we compare devices annealed in the dry nitrogen glove box, which effectively has a relative humidity of 0%, to devices annealed in our humidity control chamber. Relative humidity levels between

20-80% are tested to determine optimal levels for annealing. Results from current-voltage testing of these devices under AM1.5G illumination are shown in Table 4, while Figure 32 provides further statistical analysis of these results. In addition, Figure 33 provides current-voltage curves for these devices.

**Table 4: Average values of device PCE,  $V_{OC}$ ,  $I_{SC}$ , and FF for varying levels of humidity during perovskite film annealing step.**

Humidity Study				
Humidity (%)	PCE (%)	$V_{OC}$ (V)	$I_{SC}$ (mA/cm <sup>2</sup> )	FF (%)
0	4.92±1.80	0.59±0.05	18.26±0.80	46.22±12.05
20	10.52±1.56	0.94±0.02	18.80±0.10	66.35±9.97
30	13.50±0.11	0.95±0.01	20.55±0.11	70.90±0.36
40	11.60±0.91	0.95±0.05	18.92±1.53	66.63±3.86
50	11.95±0.90	0.91±0.03	19.73±0.65	67.13±3.33
60	11.21±1.88	0.91±0.10	20.27±0.46	62.07±4.88
70	10.71±2.03	0.93±0.08	18.87±0.54	62.79±11.57
80	10.48±0.17	0.99±0.02	17.12±0.65	66.09±1.01

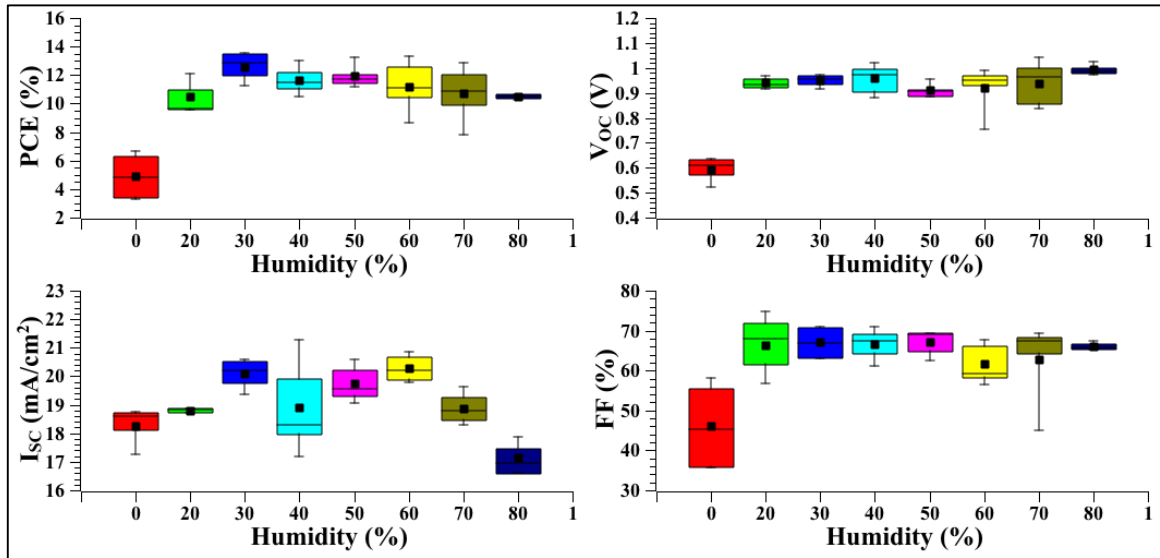


**Figure 32: Statistical analysis of photovoltaic data recorded under AM1.5G illumination for varying levels of humidity during perovskite film annealing step.**

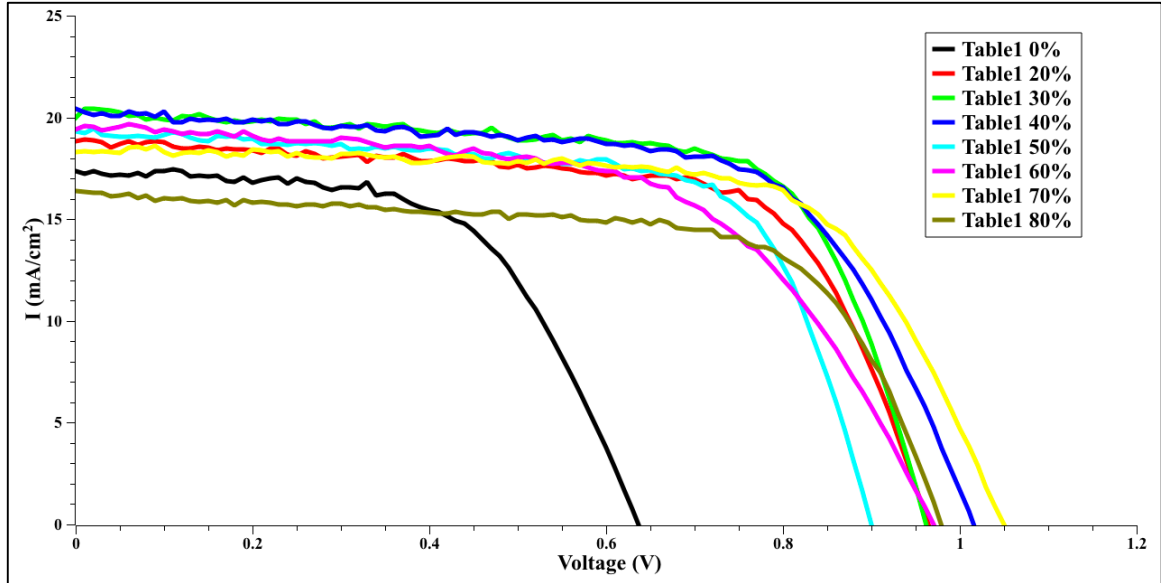


**Figure 33: Current-Voltage curves obtained from measurements taken under AM1.5G illumination for devices with varying levels of humidity during perovskite annealing step.**

As can be seen in Figures 32 and 33, perovskite films annealed between 30-60% relative humidity show better performance when tested under AM1.5G illumination. Fill factors remain fairly uniform regardless of humidity during perovskite annealing. When films are annealed in environments with <30% relative humidity, however, they suffer from reduced  $J_{SC}$  and  $V_{OC}$  values, resulting in poor PCEs. This is most likely due to insufficient moisture present during annealing, creating films with lower uniformity. Although perovskite is known to rapidly degrade when subjected to atmospheric moisture, studies are finding that perovskite films annealed in humid conditions perform better than those annealed in dry environments.<sup>48</sup> This moisture-assisted perovskite growth results in films with larger grains, resulting in fewer pinholes, and more uniform films. This process is also used for crystal growth in other crystal systems, where moisture is absorbed within grain boundaries, causing grain boundary creep.<sup>49</sup> Films which are annealed above 60% relative humidity show reductions in  $J_{SC}$ , but retain good

$V_{OC}$  levels. Annealing films in relative humidity levels above 60% induce perovskite degradation, resulting in presence of  $PbI_2$  in resultant films.<sup>48</sup>

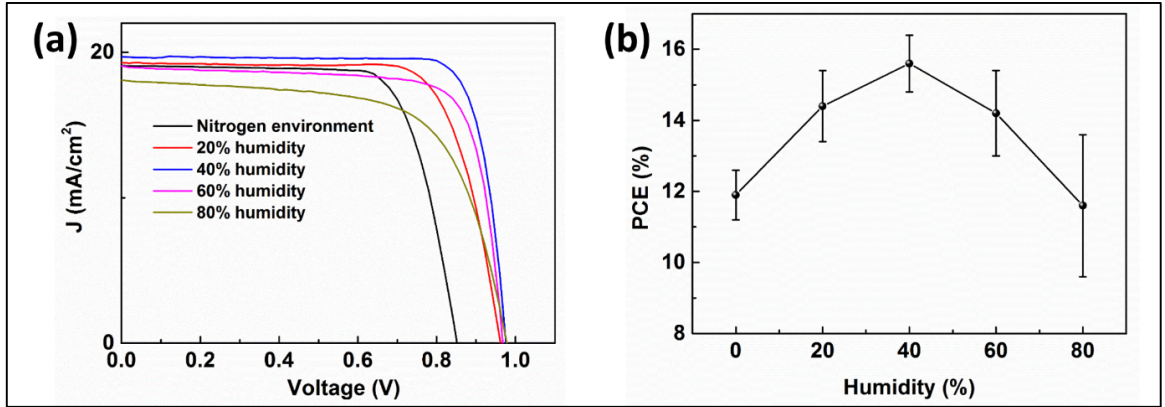


**Figure 34: (a) J-V characteristics of the devices where the perovskite precursor films annealed under different humidity level at 90°C for 2h. (b) Power conversion efficiency variation with the humidity. The error collected for 8 devices for each condition.<sup>48</sup>**

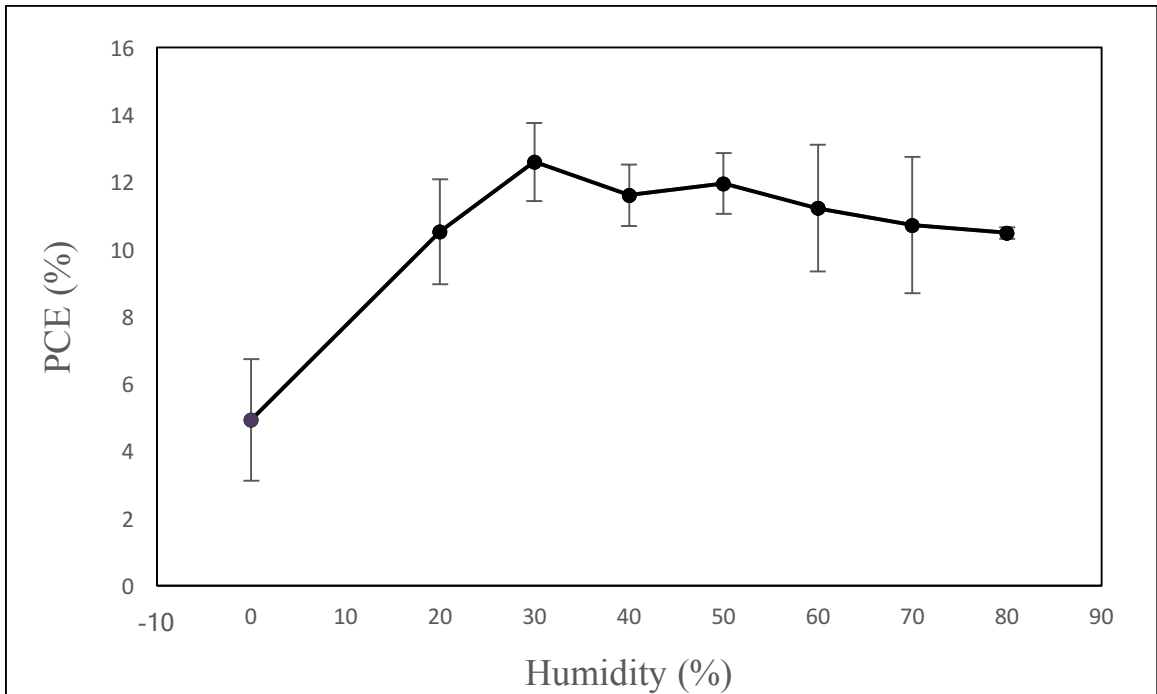


**Figure 35: Power conversion efficiency variation with humidity. Standard deviation error collected for 4 devices for each condition.**

Figure 34b shows results from a separate study in which various levels of humidity were used during annealing. Figure 35 shows results from our humidity study

in similar fashion. While there is a more pronounced drop in PCE for devices annealed at 80% relative humidity in the study of You *et al.* there is similarity in low humidity PCEs, and similar peak levels between 30-40%. Lack of significant change in performance of our devices which are annealed at 80% relative humidity might suggest that perovskite films made using our novel sequential, MAAC containing, processing possess a greater resilience to moisture.

Following our humidity study, we proceed with further optimization of annealing conditions. For this study, we vary annealing temperatures and times to find what produces best performing devices. Annealing temperatures vary between 80°C and 150°C, in 10°C increments. Annealing times of 15, 30, and 60 minutes are studied for each annealing temperature to provide a more full understanding of how the two parameters (temperature and time) are interrelated. Table 5 and Figure 36 show results from current-voltage testing under AM1.5G illumination for devices made in this study.

**Table 5: Average values of device PCE,  $V_{OC}$ ,  $I_{SC}$ , and FF measured under AM1.5G illumination for varying temperatures and times of perovskite annealing step.**

Annealing Conditions Study					
Temp. (°C)	Time (min)	PCE (%)	$V_{OC}$ (V)	$I_{SC}$ (mA/cm <sup>2</sup> )	FF (%)
80	15	0.23±0.21	0.16±0.11	4.04±0.18	31.20±8.26
80	30	3.57±0.17	1.02±0.01	5.24±0.34	66.95±1.21
80	60	5.41±3.93	0.59±0.33	15.02±0.86	53.27±24.04
100	15	6.06±0.54	0.77±0.01	13.67±1.08	58.33±2.83
100	30	12.89±0.31	0.89±0.01	19.51±0.25	74.32±0.77
100	60	11.34±0.17	0.91±0.01	17.80±0.25	70.29±0.85
120	15	7.56±0.81	0.97±0.01	10.54±1.37	74.26±1.61
120	30	12.36±0.11	0.87±0.01	19.17±0.48	73.83±0.94
120	60	9.06±0.31	0.97±0.01	12.39±0.34	75.27±0.53
150	15	6.22±0.36	0.77±0.03	13.23±1.02	61.07±3.32
150	30	9.61±0.41	0.93±0.02	14.86±0.56	69.85±1.54
150	60	7.35±0.44	0.78±0.01	14.93±1.05	62.91±1.91

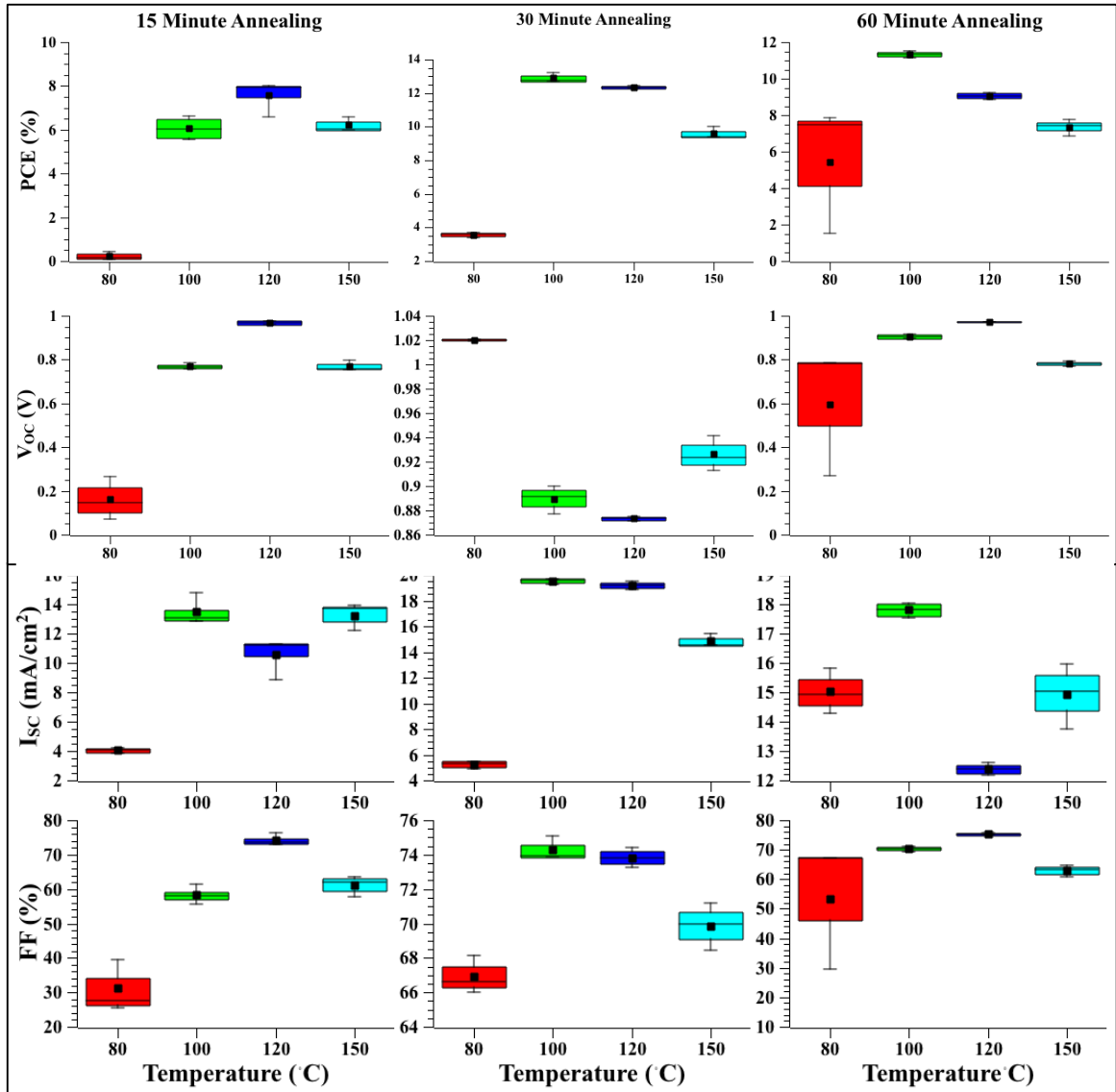


Figure 36: Statistical analysis of photovoltaic data recorded under AM1.5G illumination for varying levels temperature and time for perovskite annealing step. Graphs in the left-hand side column depict values for devices annealed for 15 minutes, while graphs in the central, and right-hand side columns depict values for devices annealed for 30, and 60 minutes, respectively.

As can be seen in Table 5 and Figure 36, optimal annealing occurs at 100°C for 30 minutes. Devices which are annealed below 100°C suffer due to inability to incite perovskite crystallization, even after an hour of annealing. As temperatures are increased above 100°C, thermal degradation of perovskite films becomes more detrimental to device performance, especially for longer annealing times.

We follow up our annealing conditions study with a test on spin speeds, however we take a slightly different approach in this study. It would take a plethora of devices with various spin speeds for each precursor deposition step for full optimization. Precursor spin speeds largely determine final perovskite film thickness, a key parameter for device optimization. Films that are too thin will not absorb sufficient light, while films that are too thick suffer from recombination effects, as well as possibility of incomplete precursor reaction. Although our second study found an optimal MAI concentration, we feel it a necessary variable to include with precursor spin speeds to achieve fully optimized perovskite film thickness. Having three independent variables to test for this optimization effort makes use of a design of experiments (DOE) attractive. Using JMP Pro 12, an initial test matrix was developed, which can be seen in Table 6.

**Table 6: Initial test matrix developed using JMP Pro 12 design of experiments software.**

<b>Initial DOE Test Matrix</b>		
<b>PbI<sub>2</sub>-MAAc Spin Speed (rpm)</b>	<b>MAI Spin Speed (rpm)</b>	<b>MAI Concentration (μg/μl)</b>
<b>3000</b>	<b>4000</b>	<b>50</b>
<b>3000</b>	<b>6000</b>	<b>50</b>
<b>2500</b>	<b>5000</b>	<b>50</b>
<b>3500</b>	<b>5000</b>	<b>50</b>
<b>3000</b>	<b>5000</b>	<b>60</b>
<b>3000</b>	<b>5000</b>	<b>40</b>

Results from illuminated current-voltage analysis for this initial study are shown in Table 7. While Figure 37 provides associated box plots for further statistical analysis.

**Table 7: Average values of device PCE,  $V_{OC}$ ,  $I_{SC}$ , and FF for varying concentrations of MAI and varying spin speeds of  $PbI_2$ -MAAc and MAI depositions.**

Initial DOE Perovskite Film Thickness Study						
$PbI_2$ -MAAc Spin Speed (RPM)	MAI Spin Speed (RPM)	MAI Concentration ( $\mu\text{g}/\mu\text{l}$ )	PCE (%)	$V_{OC}$ (V)	$I_{SC}$ ( $\text{mA}/\text{cm}^2$ )	FF (%)
3000	4000	50	12.99±0.50	0.84±0.05	22.75±0.63	68.52±2.62
3000	6000	50	8.54±0.88	0.75±0.03	18.38±1.27	62.30±4.03
2500	5000	50	11.80±0.42	0.80±0.02	21.26±0.51	69.06±2.22
3500	5000	50	8.91±0.53	0.76±0.02	18.00±0.34	65.39±2.17
3000	5000	60	14.28±0.50	0.91±0.02	21.73±0.97	72.32±1.95
3000	5000	40	7.83±0.24	0.69±0.01	17.79±0.48	64.13±2.10

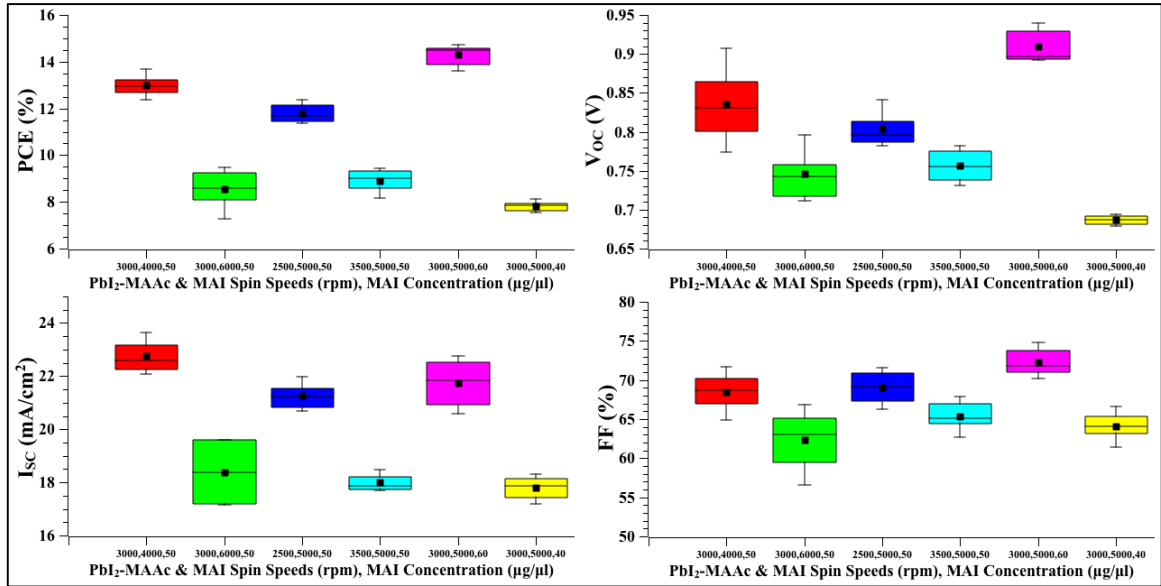


**Figure 37: Statistical analysis of photovoltaic data recorded under AM1.5G illumination for initial test matrix developed for perovskite film thickness optimization.**

Table 7 and Figure 37 show that in our initial DOE testing, an MAI concentration of 60  $\mu\text{g}/\mu\text{l}$  provides optimal performance, as in our previous study, however devices with 50  $\mu\text{g}/\mu\text{l}$  concentrations show considerable improvements when compared to the previous study. Furthermore, it is apparent that raising MAI spin speeds causes a

reduction in device performance. While it is possible to guess more using these data, it is more appropriate to use these results in conjunction with our DOE program to create a new test matrix which takes these initial results into account. The new test matrix developed using JMP Pro 12 and results from our initial test matrix, is shown in Table 8.

**Table 8: New test matrix developed using JMP Pro 12 design of experiments software and results from initial test.**

Updated DOE Test Matrix		
PbI <sub>2</sub> -MAAc Spin Speed (rpm)	MAI Spin Speed (rpm)	MAI Concentration (µg/µl)
2500	4000	40
2500	4000	60
2500	6000	40
2500	6000	60
3500	4000	40
3500	4000	60
3500	6000	40
3500	6000	60

Results from illuminated current-voltage analysis for this new test matrix are shown in Table 9. While Figure 38 provides box plots for further statistical analysis.

**Table 9: Average values of device PCE, V<sub>OC</sub>, I<sub>SC</sub>, and FF for varying concentrations of MAI and varying spin speeds of PbI<sub>2</sub>-MAAc and MAI depositions.**

Second DOE Perovskite Film Thickness Study						
PbI <sub>2</sub> -MAAc Spin Speed (RPM)	MAI Spin Speed (RPM)	MAI Concentration (µg/µl)	PCE (%)	V <sub>OC</sub> (V)	I <sub>SC</sub> (mA/cm <sup>2</sup> )	FF (%)
2500	4000	40	4.71±1.22	0.87±0.01	9.27±1.80	57.14±8.48
2500	4000	60	14.14±0.38	0.91±0.01	22.03±0.40	70.88±1.83
2500	6000	40	3.09±0.55	0.89±0.02	5.79±1.25	60.64±3.24
2500	6000	60	9.68±0.77	0.75±0.02	20.03±0.72	63.95±1.90
3500	4000	40	5.41±0.43	0.80±0.03	10.83±0.90	62.63±3.90
3500	4000	60	11.49±0.67	0.99±0.01	16.55±0.65	70.05±3.18
3500	6000	40	2.23±0.35	0.86±0.02	4.36±0.71	59.41±5.38
3500	6000	60	11.54±0.73	0.80±0.03	20.67±0.70	69.92±1.69

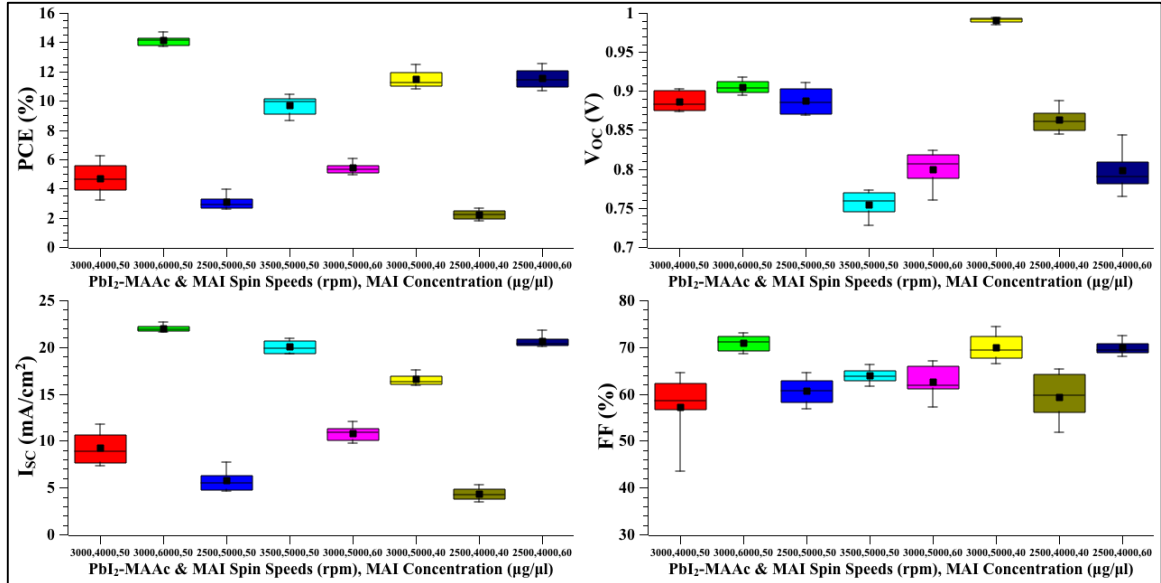


**Figure 38: Statistical analysis of photovoltaic data recorded under AM1.5G illumination for new test matrix developed for perovskite film thickness optimization.**

These results from the new test matrix show clear inability for MAI concentrations below 50  $\mu\text{g}/\mu\text{l}$  to yield efficient devices. We note that these results also confirm our previous assumption that increasing MAI spin speeds reduces device performance. In addition, we see here that lower  $\text{PbI}_2$  spin speeds are more desirable. To provide more insight on how these parameters change perovskite film thicknesses, we use profilometry to measure  $\text{PbI}_2$ -MAAc films grown at various spin speeds, as well as final perovskite film thicknesses with various MAI spin speeds.

**Table 10: Profilometer Measurements.**

<b>PbI<sub>2</sub>-MAAc Spin Speed (rpm)</b>	<b>MAI Spin Speed (rpm)</b>	<b>MAI Concentration (<math>\mu\text{g}/\mu\text{l}</math>)</b>	<b>Thickness (nm)</b>
<b>1500</b>	<b>0</b>	<b>0</b>	418.6 $\pm$ 20.0
<b>3000</b>	<b>0</b>	<b>0</b>	349.5 $\pm$ 20.4
<b>4000</b>	<b>0</b>	<b>0</b>	289.1 $\pm$ 13.5
<b>6000</b>	<b>0</b>	<b>0</b>	240.9 $\pm$ 14.5
<b>7000</b>	<b>0</b>	<b>0</b>	304.1 $\pm$ 14.1
<b>3000</b>	<b>3000</b>	<b>50</b>	462.3 $\pm$ 27.1
<b>3000</b>	<b>3000</b>	<b>70</b>	496.3 $\pm$ 27.9
<b>3000</b>	<b>7000</b>	<b>50</b>	371.2 $\pm$ 7.8
<b>3000</b>	<b>7000</b>	<b>70</b>	474.7 $\pm$ 13.2

Efforts to estimate optimal perovskite solar cell efficiencies show that for a  $\sim 0.5$   $\mu\text{m}$  thick  $\text{CH}_3\text{NH}_3\text{PbI}_3$  absorber, the theoretical maximum PCE is 21%.<sup>50</sup> In addition, calculations on theoretical limits for  $J_{\text{SC}}$  and  $V_{\text{OC}}$  are found to be  $19.2 \text{ mA cm}^{-2}$  and  $1.19 \text{ eV}$ , respectively.<sup>9</sup> While  $J_{\text{SC}}$  and  $V_{\text{OC}}$  values are agreeable with experimental results for a  $0.33 \mu\text{m}$  thick device ( $21.5 \text{ mA cm}^{-2}$ , and  $1.07 \text{ eV}$ ),<sup>51</sup> there is considerable discrepancy in experimental and theoretical PCEs (15.4% and 21%, respectively). This disparity is largely due to low FF (67%), which is believed to be limited by band offsets between perovskite absorber and interfaces at transport/contact layers. As seen in our efforts to optimize perovskite layer thickness, we are able to achieve a 14.9% efficient device with a  $J_{\text{SC}} \sim 24 \text{ mA cm}^{-2}$ ,  $V_{\text{OC}}$  of  $0.91 \text{ eV}$ , and 72% FF, with a  $0.5 \mu\text{m}$  thick perovskite layer. Of notable importance, is that estimations of perovskite performance as functions of absorber thickness show that a thickness of  $\sim 0.75 \mu\text{m}$  is needed for such a high  $J_{\text{SC}}$ . In addition, these estimations show that as absorber thickness is increased, there is a decrease in  $V_{\text{OC}}$  ( $1.19 \text{ eV}$  at  $0.3 \mu\text{m}$  to  $1.17 \text{ eV}$  at  $0.75 \mu\text{m}$ ) and FF (89.7% at  $0.3 \mu\text{m}$  to

89.5% at 0.75 $\mu\text{m}$ ). Although our FF is similar to that achieved from devices using mixed halides, it is still much lower than the theoretical limit. Also, our  $V_{\text{OC}}$  is significantly lower than both experimental results and theoretical maximum. If similar  $J_{\text{SC}}$  and FF can be achieved with a  $V_{\text{OC}}$  comparable to other high-performance devices,<sup>51</sup> a PCE of 18.3% can be achieved. If these parameters are coupled with a  $V_{\text{OC}}$  near theoretical maximum, a PCE of 20.4% is achievable. If our  $J_{\text{SC}}$  is coupled with theoretical max values for  $V_{\text{OC}}$  and FF for a 0.5  $\mu\text{m}$  thick perovskite layer, resultant PCE would be 21.7%, which is in close agreement to calculated ideal values.

Another consideration to be had from these theoretical models, is that  $J_{\text{SC}}$  is highly dependent on perovskite thickness, while  $V_{\text{OC}}$  and FF show little dependence.<sup>9</sup> For example, in these models,  $J_{\text{SC}}$  ranges from 12  $\text{mA cm}^{-2}$  at a thickness of 0.2  $\mu\text{m}$  to 29  $\text{mA cm}^{-2}$  for a 3  $\mu\text{m}$  thick perovskite layer. Contrast this with  $V_{\text{OC}}$  values of 1.21 eV and 1.15 eV, and fill factors of 89.7% and 89.4%, at the respective thicknesses of 0.2  $\mu\text{m}$  and 3  $\mu\text{m}$ .

### 3.2 Comparative Analysis

A In this section, we compare perovskite films made using various deposition techniques. Perovskite films made using typical one-step and two-step processing without MAAC are compared to films made using our enhanced two-step deposition method with MAAC. Our initial comparison is made using XRD measurements. There are well known peaks corresponding to  $\text{CH}_3\text{NH}_3\text{PbI}_3$ , as well as  $\text{PbI}_2$ . By analyzing these peaks, we can determine properties such as crystalline phase, incomplete perovskite formation and perovskite degradation. Our initial use of XRD, as seen in Figure 31, helped determine what MAI concentration allowed for full conversion of  $\text{PbI}_2$  into

perovskite without leaving an excess of insulating MAI. Here, we compare XRD peaks for perovskite films grown with, and without, MAAc, to determine in what ways this adduct might change resultant crystal structures. Notable changes could result in presence of new, or absence/shift of typical, peaks. Figure 39 offers normalized XRD scans for two perovskite films, one with, and one without MAAc.

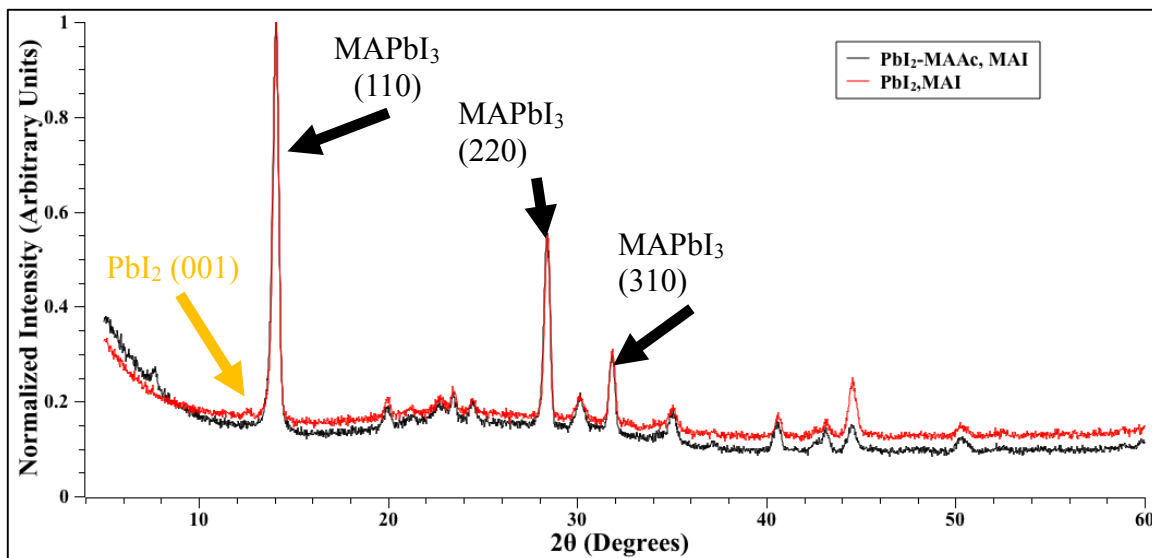


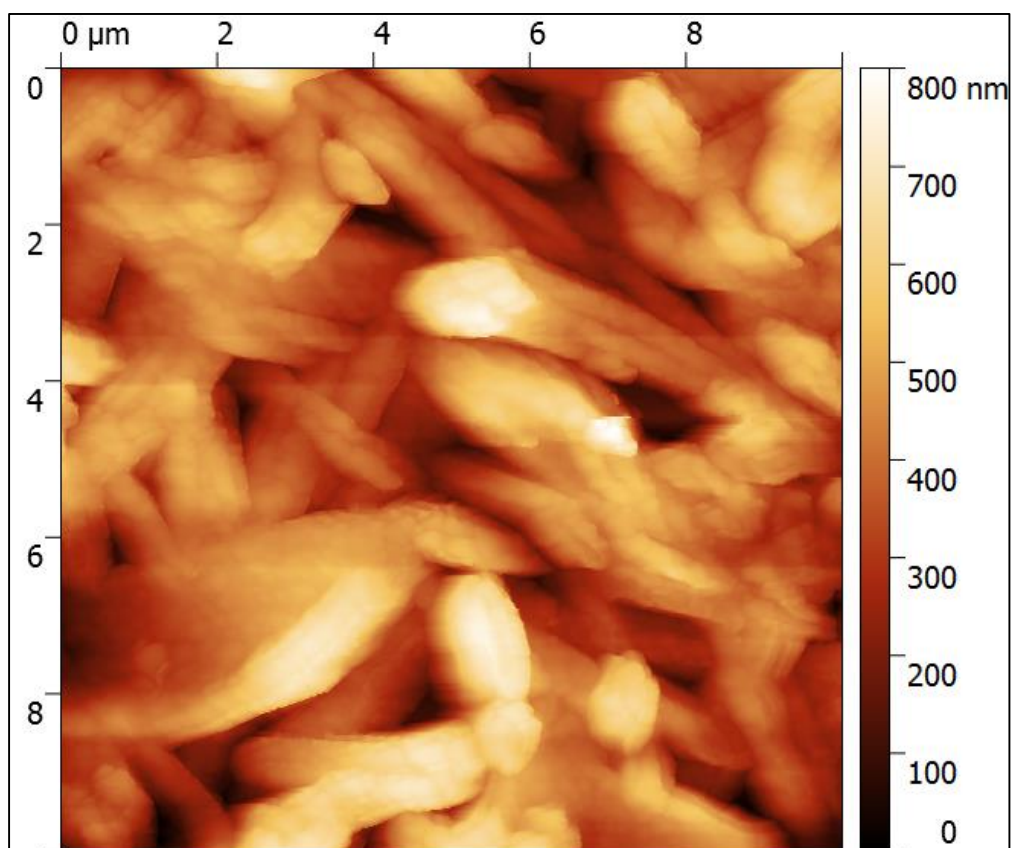
Figure 39: XRD spectra of perovskite films grown with, and without MAAc.

As is evident in Figure 39, both films possess dominating peaks centered around  $\sim 14.2$  degrees, which is typical of 1 1 0 oriented tetragonal perovskite.<sup>52</sup> Aside from a small peak around 7.7 degrees, likely due to unreacted acetate, and a decrease in relative intensity in the peak centered around 44.6 degrees, there seems to be no significant differences. This helps confirm the fact that MAAc adduct allows for better reaction control, resulting in smoother perovskite films, without altering crystal structures of resultant films.

XRD analysis provides a lot of insight towards crystal structures and their orientations for our perovskite films. Although AFM and SEM imaging can't provide

information on crystal structures like XRD analysis, they provide sufficient information concerning film properties.

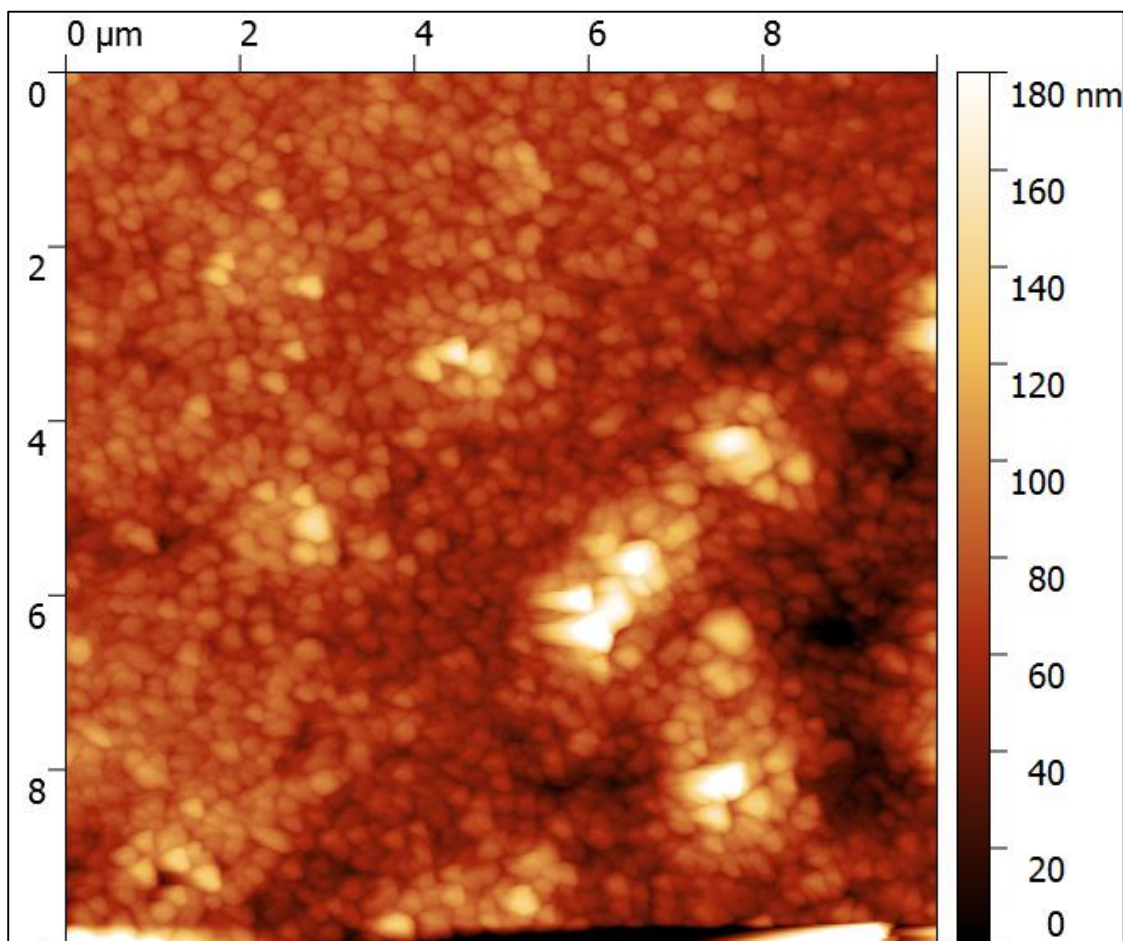
To gain a confident understanding of perovskite film quality, we use AFM surface scans to learn about roughness and uniformity. We analyze perovskite films made using traditional one, and two, step processing, as well as films made using our novel sequential MAAC adduct containing deposition method. Figure 40 shows an AFM surface scan of a perovskite film made using a one-step deposition technique (no MAAC).



**Figure 40: AFM surface scan of perovskite film grown using a standard one-step growth method.**

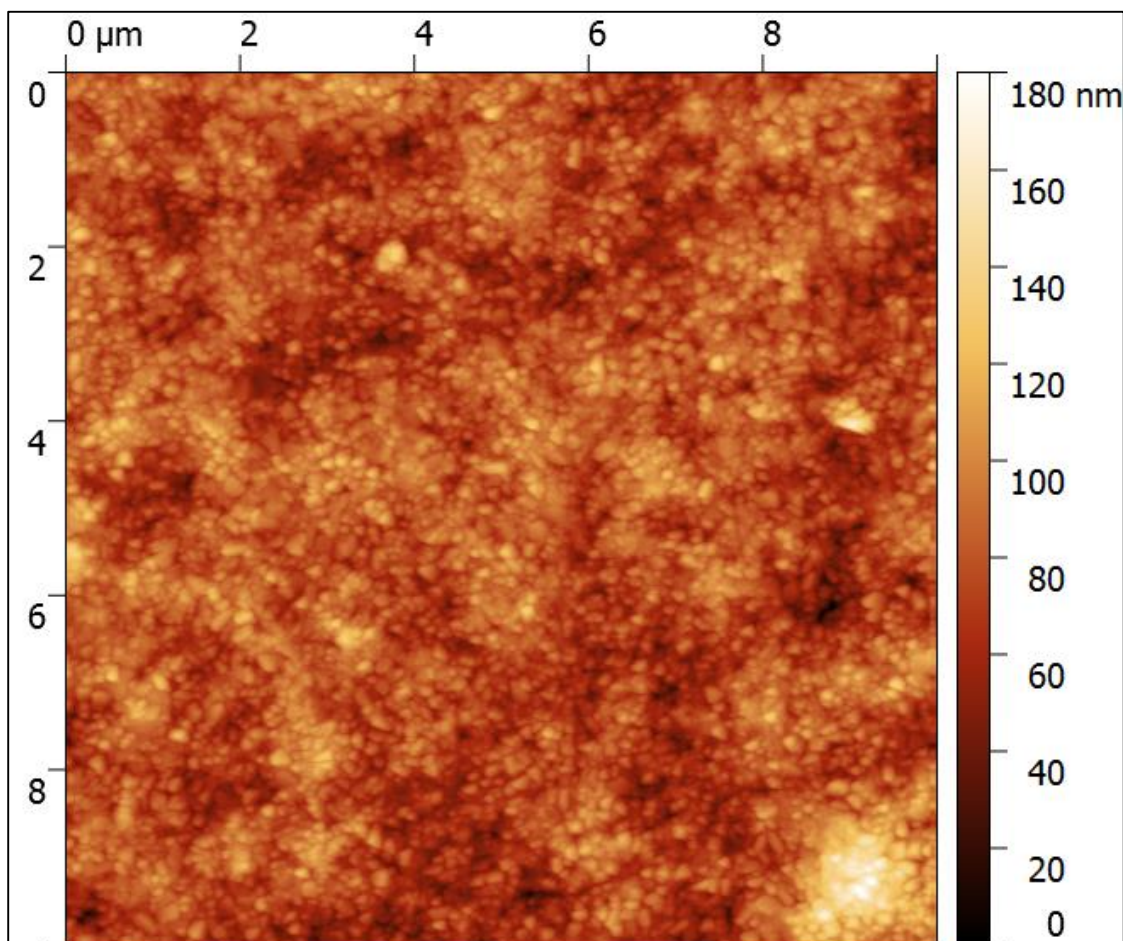
As can be seen from Figure 40, one-step methods provide very low control over crystal growth formation. Large crystals with poor uniformity, incomplete film coverage and very high surface roughness are typical of this processing. Root Mean Square (RMS)

of surface roughness for one-step perovskite film is  $133\pm 27$  nm. Figure 41 provides a similar AFM scan of a perovskite film, sans MAAC, made with a standard sequential deposition (two-step) method.



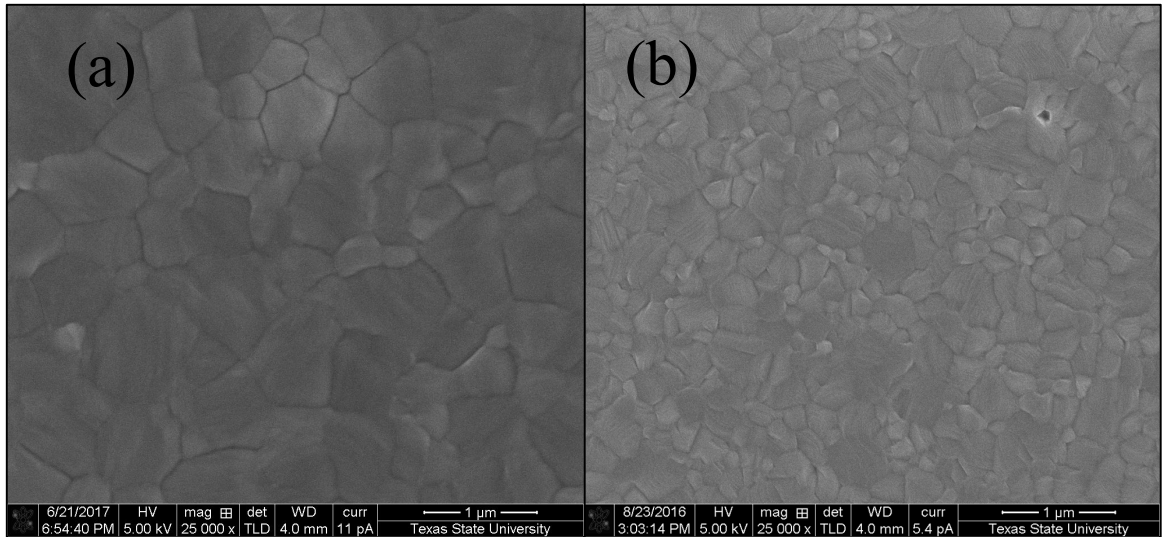
**Figure 41: AFM surface scan of perovskite film grown using a standard two-step growth method.**

Figure 41 shows that sequential deposition methods yield more uniform perovskite films due to better control of film properties and crystal growth.  $\text{PbI}_2$  films act as a template or scaffold, allowing for more controlled, uniform perovskite growth. While film coverage and surface roughness ( $\text{RMS}=25\pm 20\text{nm}$ ) is better for two-step methods than single-step processing, there is still poor repeatability and significant morphological defects in the film.



**Figure 42: AFM surface scan of perovskite film grown using two-step growth method with MAAc adduct.**

Our improved two-step deposition method possessing MAAc adduct facilitates smooth film growth due to MAAc widening spaces between  $\text{PbI}_2$  layers (Figure 42). This allows MAI molecules to fully intercalate into these regions before reaction completion. In addition, MAAc inhibits precursor reaction until it is slowly removed from the film during annealing. Although crystalline size is smaller for this method, film uniformity, smoothness, and reproducibility are all increased. A RMS surface roughness of  $17 \pm 4$  nm is seen in perovskite films made with our improved processing.



**Figure 43: SEM images of perovskite films grown (a) without MAAc, and (b) with MAAc.**

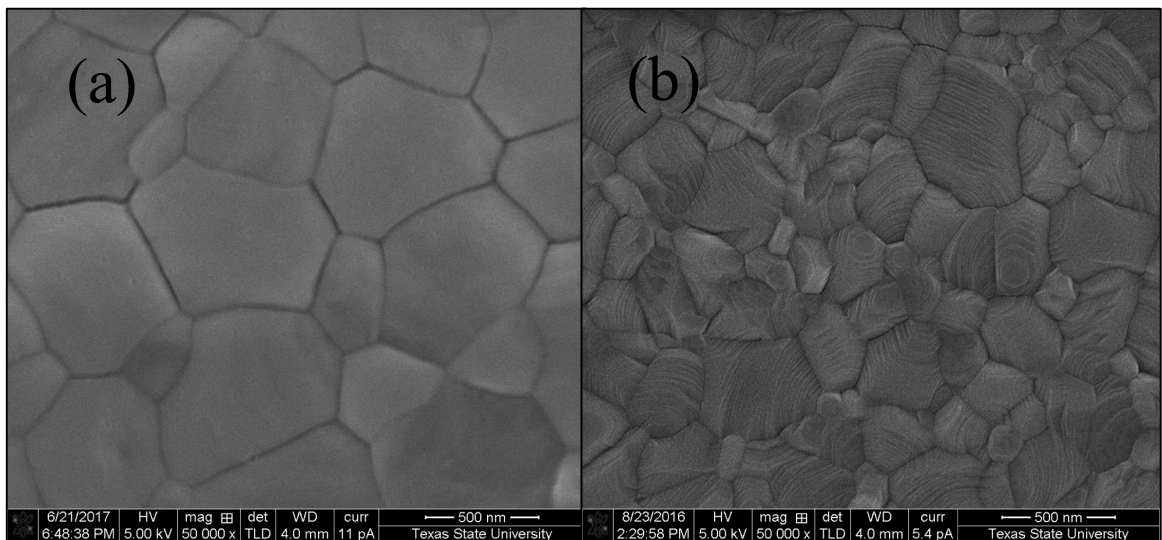


**Figure 44: Higher magnification SEM images of perovskite films grown (a) without MAAc, and (b) with MAAc.**

As can be seen from high-resolution SEM imaging (Figures 43 & 44), perovskite films grown using our novel sequential step, MAAc adduct containing, deposition process are more uniform and smooth than those made using standard two-step processing. This, and the realization that our new technique yields films with smaller grains, is in agreement with our AFM analysis. In traditional polycrystalline

semiconductors, grain boundaries provide for deep defect levels, offering significant recombination sites, and are thus highly undesirable. Decreasing grain sizes provides more grain boundaries and would typically cause a severe reduction in optical semiconductor device performance. However, results from measuring electron beam induced current (EBIC) contrast from polycrystalline perovskite grain boundaries show that the EBIC contrast of the grain boundaries is no different than that of the actual grains. These results mean that grain boundaries in polycrystalline perovskite films are electrically invisible, and do not share the detrimental effects of their traditional polycrystalline semiconductor counterparts.<sup>53</sup> This helps explain why our method is capable of producing higher performance devices with smaller grain sizes (more grain boundaries) in the polycrystalline perovskite layers.

Results from current-voltage analysis taken under AM1.5G illumination for optimized devices made with and without MAAC are given in Table 11. These results show measurements taken from a total of 16 devices: eight made with MAAC, and eight without.

**Table 11: Optimized device performance values for perovskite films grown with and without MAAC.**

	<b>With MAAC</b>	<b>Without MAAC</b>
<b>PCE (%)</b>	14.11±0.59	11.79±0.39
<b>I<sub>SC</sub> (mA)</b>	22.08±0.80	19.83±0.79
<b>V<sub>OC</sub> (V)</b>	0.90±0.02	0.88±0.04
<b>FF (%)</b>	70.98±2.94	68.01±2.18

Figure 45 shows logarithmic current density-voltage curves taken in the dark, and under AM1.5G illumination for an optimized perovskite solar cell device made using MAAC. Although the dark current is not as low as typical CH<sub>3</sub>NH<sub>3</sub>PbI<sub>3</sub> photodetectors,

these measurements were made for an optimized solar cell device. Further testing of optimized perovskite photodetectors made using MAAC should provide a more accurate representation of dark current levels for these devices. Although these results are not fully comparable with standard perovskite photodetectors made using traditional two-step methods, they still illustrate clear ability for perovskite devices made using our novel two-step deposition to outperform state of the art silicon photodetectors for visible spectrum imaging.

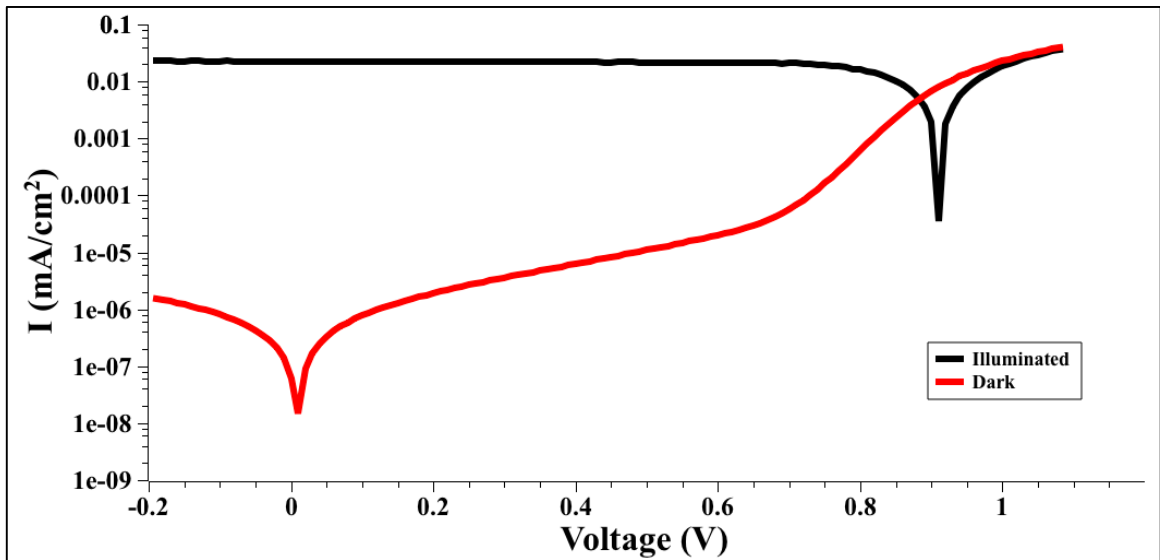
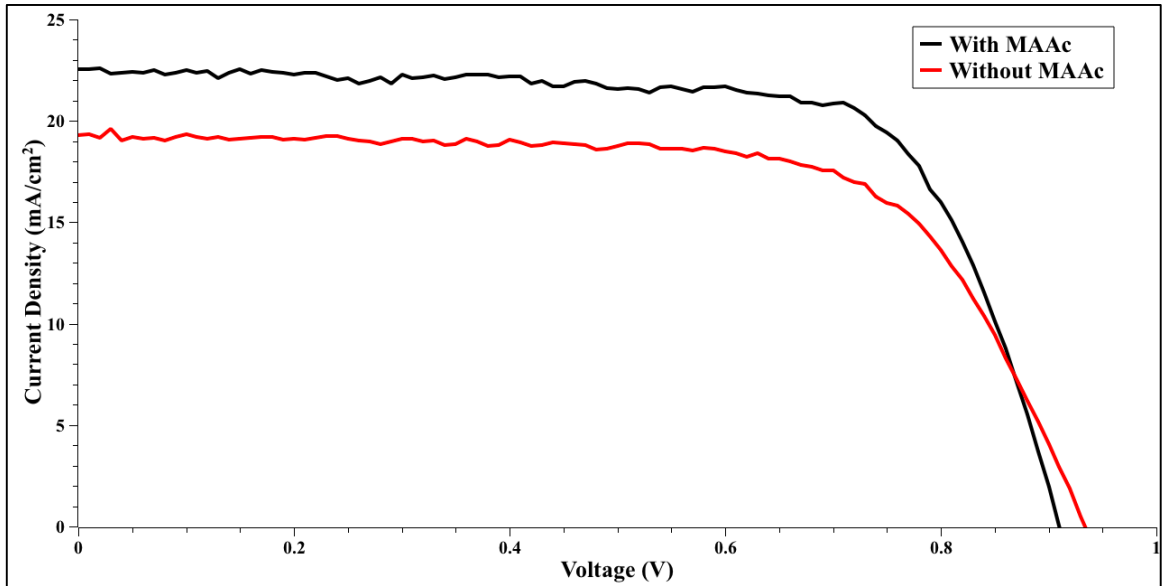


Figure 45: Dark, and AM1.5G illuminated, Current-Voltage curves for a large area (6.25mm<sup>2</sup>), single pixel perovskite photodetector made using our novel, MAAC containing, two-step process.

Figure 46 shows current-voltage measurements taken under AM1.5G illumination for highest performing devices made with, and without, MAAC. While the “champion” device made using traditional two-step processing exhibits a higher open circuit voltage, the highest performing device made using our MAAC-containing two-step perovskite deposition procedure has a significantly higher short circuit current. Additionally, open circuit voltage is a metric which is more important for solar cell performance, while having a higher short circuit current is more attractive for photo-detecting applications.

Furthermore, our optimization efforts focused on perovskite films, and further optimization of transport layer properties can provide for higher open circuit voltages.



**Figure 46: Current-voltage analysis of champion devices fabricated with, and without, MAAC.**

Results from EQE testing of an optimized MAAC-containing device is shown in Figure 47, along with integrated current density as a function of wavelength. EQE analysis is consistent with typical, high-efficiency perovskite solar cells reported elsewhere in literature.<sup>54</sup> This not only confirms results from our current-voltage analysis, it also reiterates the fact that our optimized perovskite absorbers have superior performance in the visible spectrum than state of the art Si.

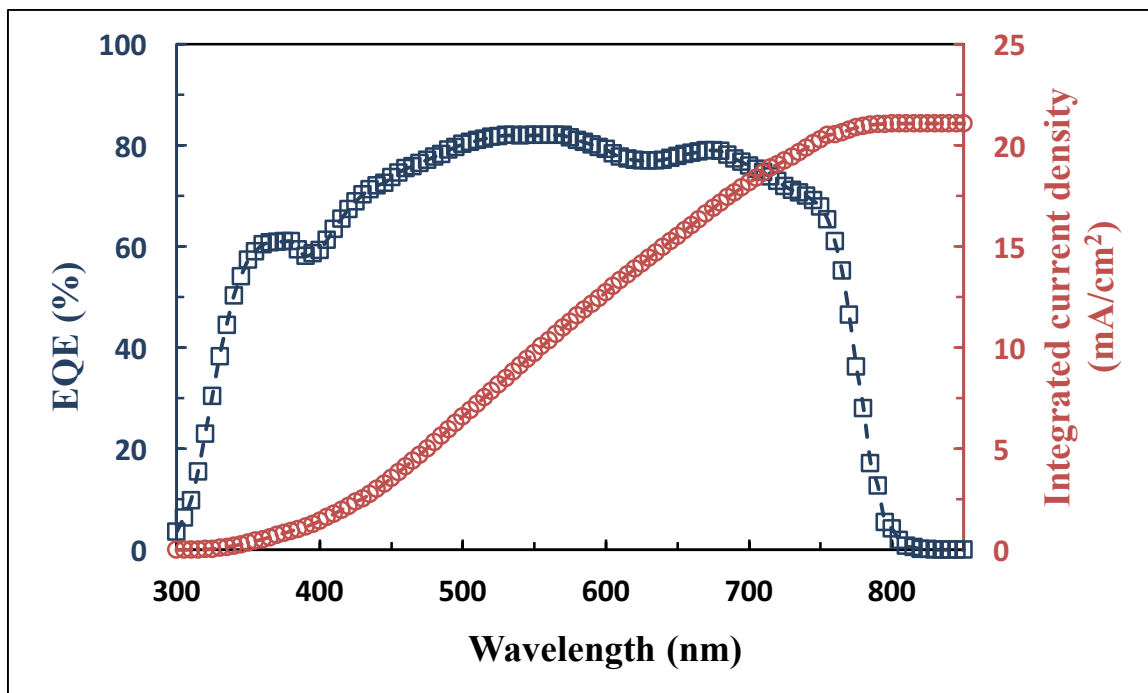


**Figure 47: External quantum efficiency and integrated current density measurements for an optimized device made using our novel two-step, MAAC containing, process.**

Figure 48 shows spectral results from UV-Vis absorption characterization. While overall pattern of absorbance is nearly identical, films made with MAAC show slightly less absorbance from 300-500 nm than films made without. In addition, films made with MAAC show superior absorption for wavelengths > 600 nm, when compared to films made without.

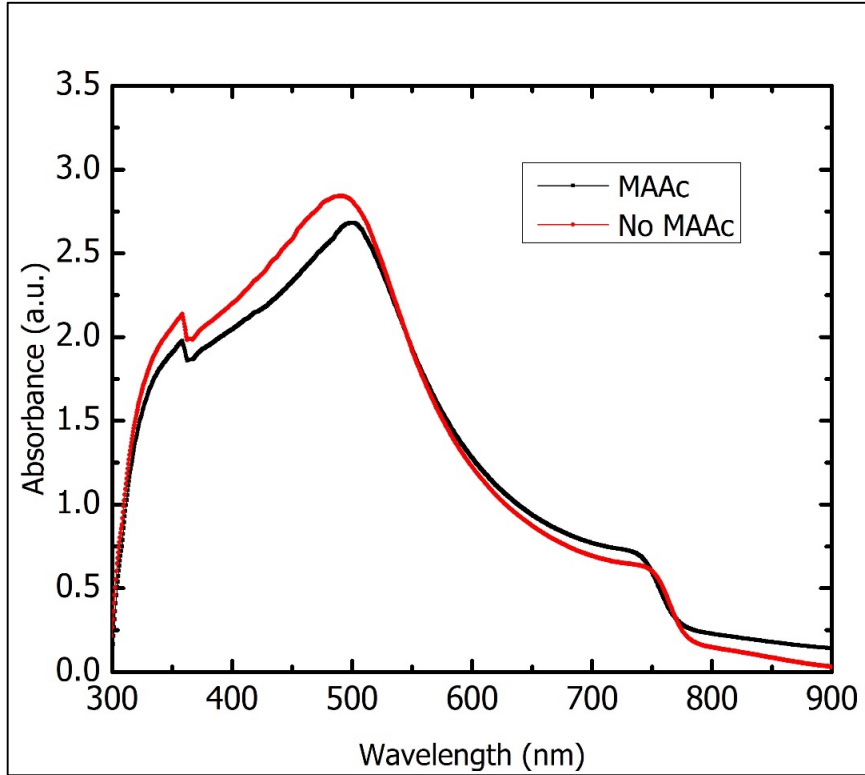


Figure 48: Absorption spectrum of perovskite synthesized using two-step-solution-based spin coating with, and without, MAAC.

### 3.3 Patterning Results

$\text{CH}_3\text{NH}_3\text{PbI}_3$  films are not typically patterned by conventional photolithography due to their high solubility in polar solvents utilized in photoresist processing, including water-based developers (tetramethylammonium hydroxide, sodium hydroxide, acetone, isopropanol (IPA), and n-methyl-2-pyrrolidone (NMP)). The latter is often used as a native solvent for perovskite precursor ink. This point is further illustrated in Figure 49, which shows perovskite films on glass substrates partially immersed in various solvents. Solvents such as water and acetone, which possess high dielectric constants ( $\epsilon$ ), completely dissolve the perovskite film. It is also evident that IPA, being less polar, only dissolves the organic part of the film, resulting in yellow discoloration as the perovskite is reduced to  $\text{PbI}_2$ . These results are confirmed by XRD analysis, as shown in Figure 50.



**Figure 49: Solvency tests of  $\text{CH}_3\text{NH}_3\text{PbI}_3$  in various solvents with different polarity. Photographs of samples were taken after 10 min of immersion (10 s in the case of acetone).**

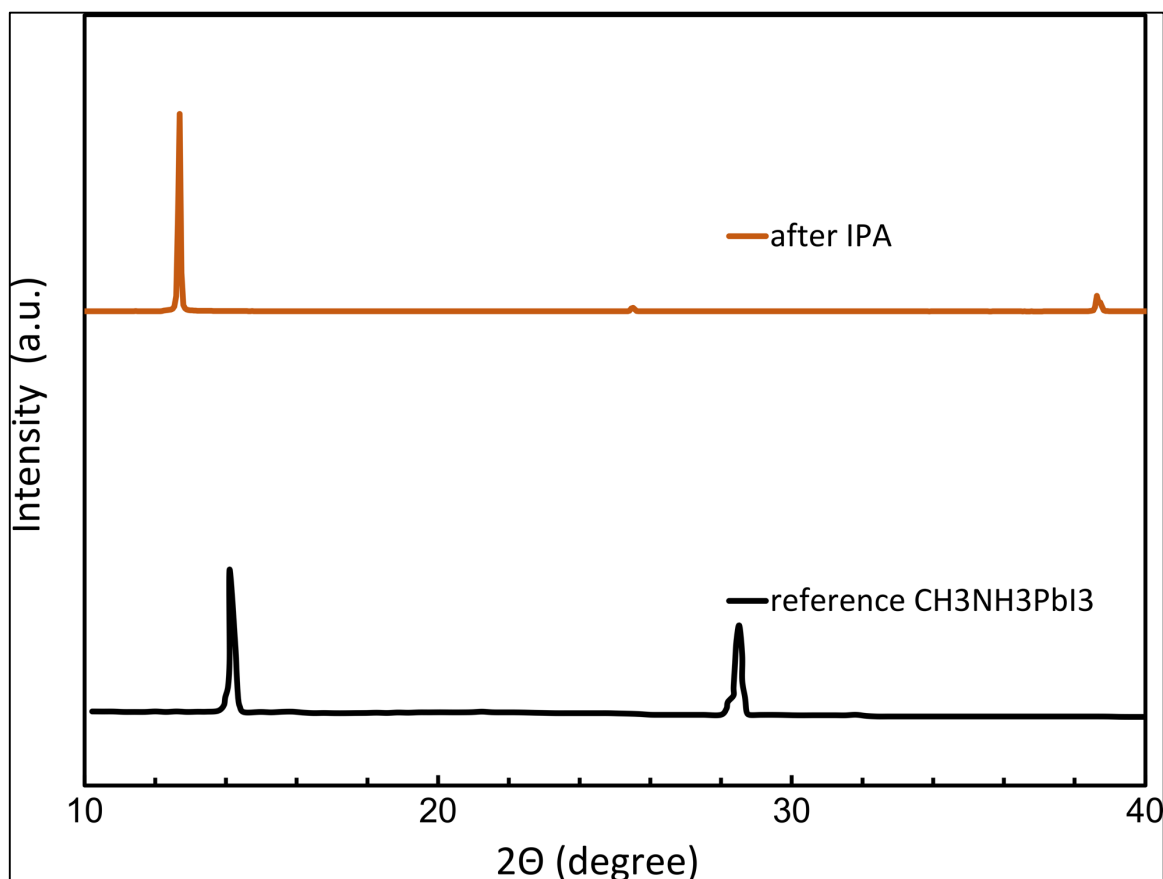


**Figure 50: XRD spectra of  $\text{CH}_3\text{NH}_3\text{PbI}_3$  film after immersion in IPA solvent for 10 minutes. It can be seen that the organic component is completely removed from the film, leaving only  $\text{PbI}_2$ .**

Propylene glycol methyl ether acetate (PGMEA), a commonly used native solvent for most commercial resists, degrades perovskite films at the solvent– air interface (Figure 51), and is likely due to surface tension-related effects. While non-polar toluene does not readily dissolve perovskite films, and is even used to assist in growth of

perovskite films, prolonged immersion of samples in toluene does eventually destroy perovskite films.

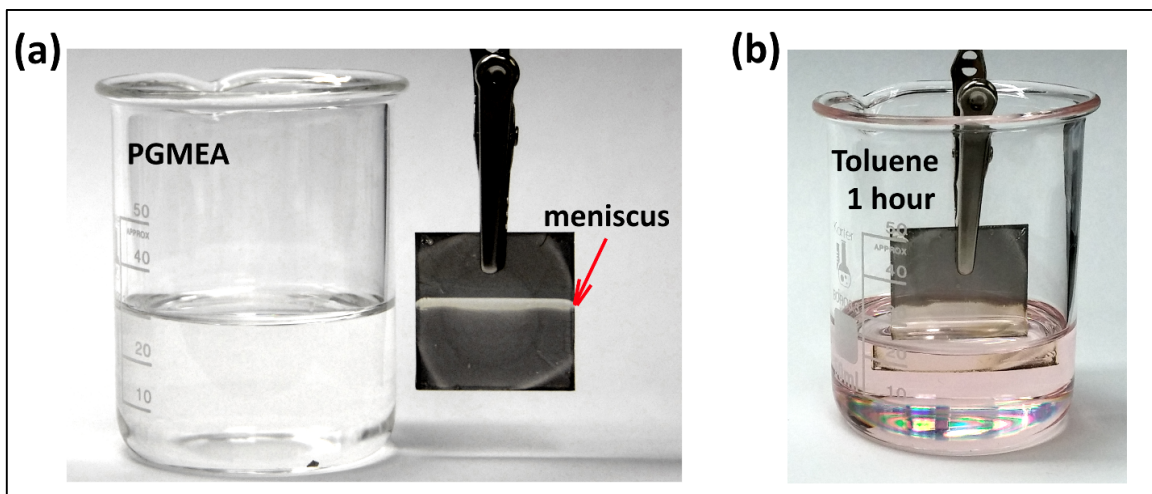


**Figure 51: (a) PGMEA (propylene glycol methyl ether acetate) solvent, while overall being a poor solvent for  $\text{CH}_3\text{NH}_3\text{PbI}_3$  does dissolve the film near the meniscus. (b) Perovskite film deposited on glass/PEDOT:PSS is dissolved (possibly delaminated due to swelling of PEDOT:PSS) in toluene after 1 hour immersion**

There are no visible changes (swelling, cracking, color change, etc.) in perovskite films exposed to the fluorinated solvents we utilize in this study: HFE7100 (methoxyperfluorobutane, a mixture of normal and iso-butyl isomers) and HFE7300 (3-methoxyperfluor-2-methylpentane) for up to 10 h. These results suggest HFE solvents are chemically orthogonal to  $\text{CH}_3\text{NH}_3\text{PbI}_3$  films. This stability of  $\text{CH}_3\text{NH}_3\text{PbI}_3$  in HFE solvents enables implementation of photolithographic processing based upon these solvents. We refer to this method as “orthogonal photolithography” and it is also employed to fabricate organic semiconductor devices such as organic light emitting diodes,<sup>55</sup> organic transistors,<sup>56</sup> and organic biosensors.<sup>57</sup>

Evaluations of structural and optical properties of exposed and unexposed device regions confirm that perovskite film converts into  $\text{PbF}_2$  (Figure 52). XRD spectra of reference (non-patterned) and resist protected perovskite films are nearly identical

(Figure 52a). These results support our conclusion that 1.5  $\mu\text{m}$  thick resist is sufficient protection from  $\text{SF}_6$  plasma treatment. XRD spectrum of unprotected film is strikingly dissimilar from original perovskite film, and appears to be comparable to that of  $\text{PbF}_2$  glass.<sup>58</sup> This spectrum reveals several broad peaks which correspond to cubic  $\beta\text{-PbF}_2$  crystalline phase.

Estimations of crystalline sizes are made using Scherrer's equation:

$$D = \frac{K\lambda}{\beta \cos(\theta)} \quad (14)$$

where  $D$  is the crystal size,  $\lambda$  the X-ray wavelength,  $\beta$  the diffraction peak half-width,  $\theta$  the Bragg angle, and  $K$  is a dimensionless shape factor ( $\sim 1$ ). The mean particle size of  $\text{PbF}_2$  crystallites is calculated to be  $\sim 8$  nm. It is also observed that  $\text{SF}_6$  plasma treatment of unprotected perovskite films yielded dramatic changes to the film's appearance and morphology. In contrast, protected  $\text{CH}_3\text{NH}_3\text{PbI}_3$  films retain their brown color (with optical bandgap  $\sim 1.6$  eV) while  $\text{SF}_6$  modified films are predominately transparent in the optical region with a broad absorption peak at 430 nm. This is believed to be a result of color centers related to oxygen impurities.<sup>59</sup> SEM imaging of  $\text{SF}_6$  modified film surfaces reveals a morphology with high defect concentrations and average thicknesses of approximately 200 nm. In comparison, resist-protected perovskite films average 350nm and retain a smooth, continuous morphology after patterning (Figure 52c and d).

Energy dispersive X-ray spectroscopy (EDS) spectra of protected and unprotected regions of perovskite film is shown in Figure 52e, with respective areas denoted as areas "A" and "B" in Figure 52d. Chemical analysis of both areas is consistent with our conclusion that  $\text{SF}_6$  plasma treatment of perovskite films, protected by photoresist, has no effect on the chemical composition of the perovskite film, while unprotected

$\text{CH}_3\text{NH}_3\text{PbI}_3$  transforms into  $\text{PbF}_2$ .

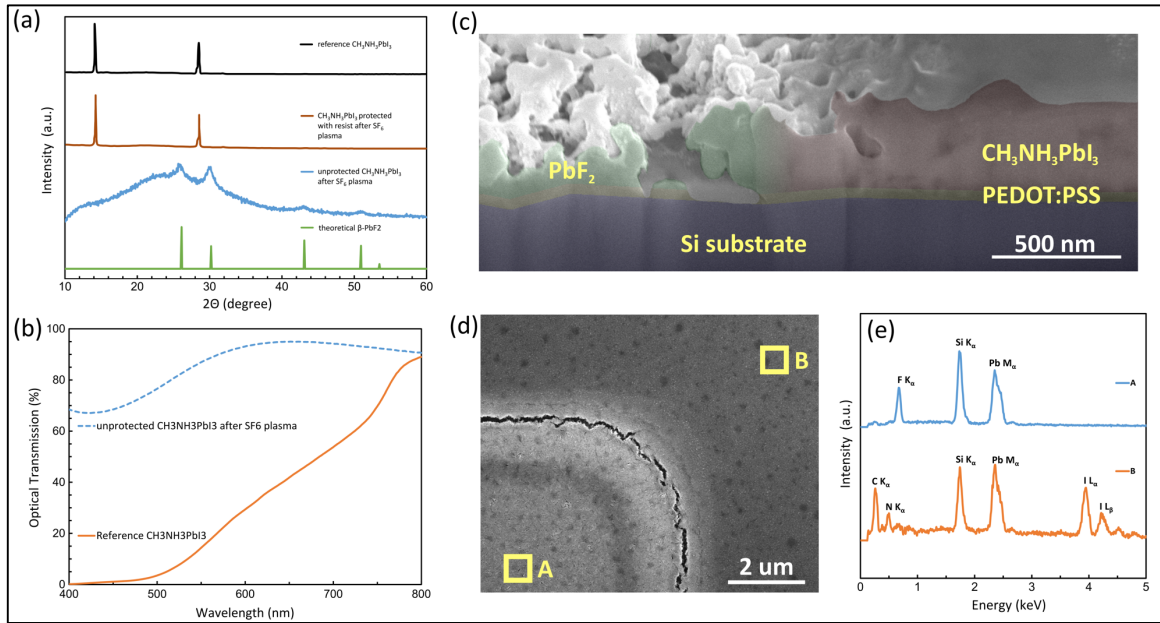


**Figure 52: (a) XRD spectra, (b) optical transmission spectra, (c) cross-sectional SEM image, (d) SEM image of surface, and (e) EDS of resist protected and unprotected portions of perovskite film after complete patterning process.**

We find it difficult to dry etch  $\text{CH}_3\text{NH}_3\text{PbI}_3$  due to heavy lead molecules which do not easily form volatile compounds with halogens. While RIE protocols exist for similar compounds (e.g., lead zirconate titanate (PZT))<sup>60</sup> they often require either hard contact between mask and resist, or high aspect ratio resists due to low resist selectivity and slow etch rates.<sup>61</sup> Argon ion milling is not a suitable alternative to etch organic perovskites due to resist carbonization, which produces insoluble reaction products.<sup>62</sup> It is also not possible to etch resist with  $\text{O}_2$  plasma because it tends to chemically attack and degrade the organic component of perovskite films. Instead, a dry patterning process is employed in this work to etch the organic constituencies of perovskite films, while replacing iodine with fluorine. Our functionalization approach, and resulting products, are confirmed using *in situ* optical emission spectra of gas-discharge plasma in close

proximity to the device (ca. 5 mm above the surface). Characteristic emission lines of I, H, N, and F are provided in Table 12, while their time evolutions are provided in Figure 53. The complete optical spectrum is more complex as can be seen in Figure 54, however its characteristic emission lines are used to trace main transformations in the system.

**Table 12: Atomic spectra of I, H, N, and F.**

Element	Atomic transition	Wavelength, nm	Reference
I	$5s^25p^5 - 5s^25p^4(^3P_2)6s$	206.2	63
	$5s^25p^3(^2D^\circ)6s - 5s^25p^3(^2D^\circ)6p$	534.0	64
	$5s^25p^3(^4S^\circ)6s - 5s^25p^3(^4S^\circ)6p$	562.6	64
H	$2s - 3p (2p - 3d)$	486.1	65
	$2s - 4p (2p - 4d)$	656.3	65
N	$2s^22p3s - 2s^22p3p$	399.5	66
	$2s^22p3s - 2s^22p3p$	648.2	66
F	$2s^22p^4(^3P)3s [4P] - 2s^22p^4(^3P)3p [^4D^\circ]$	685.6	67
	$2s^22p^4(^3P)3s [^2P] - 2s^22p^4(^3P)3p [^2P^\circ]$	703.7	67

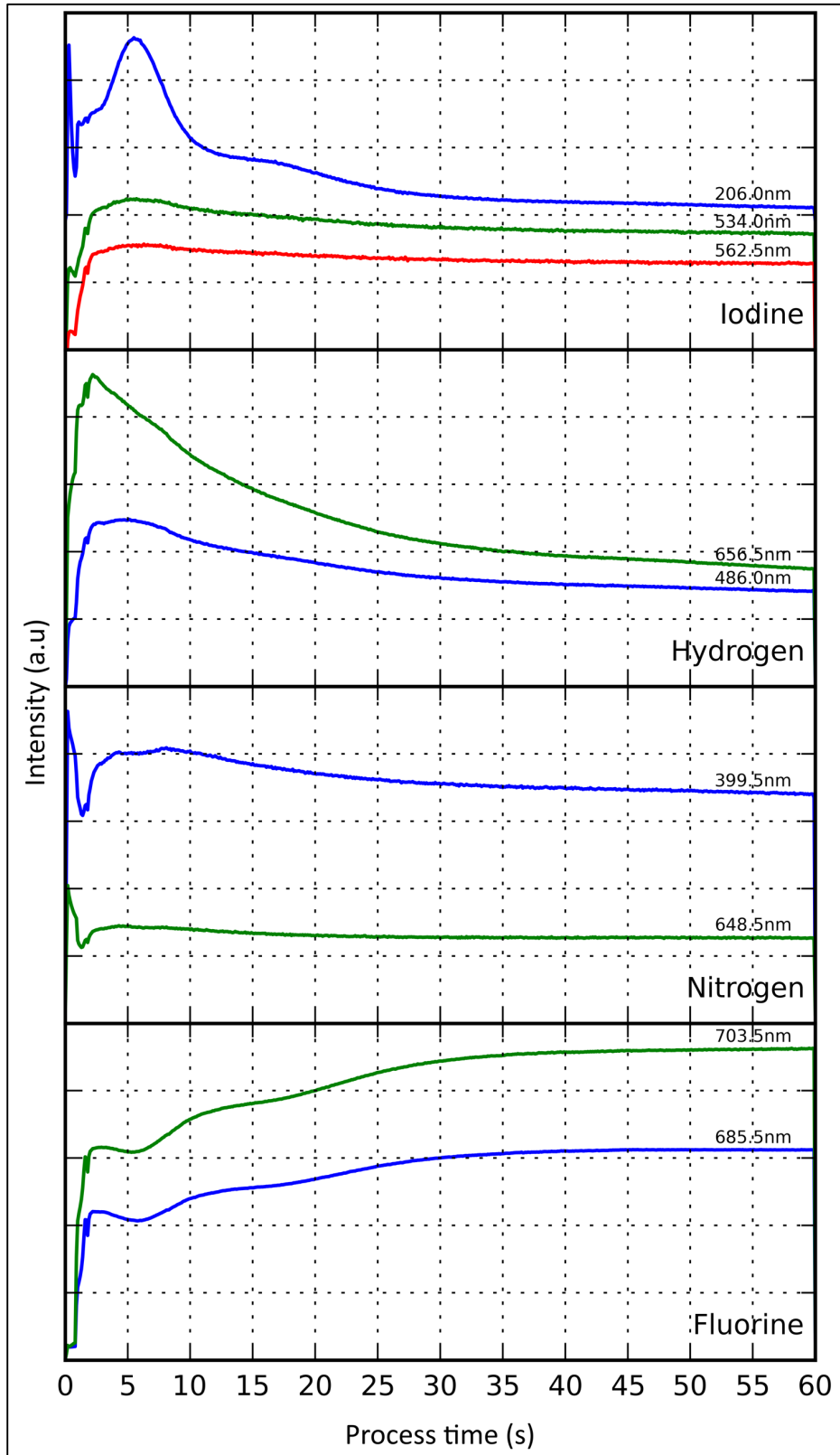
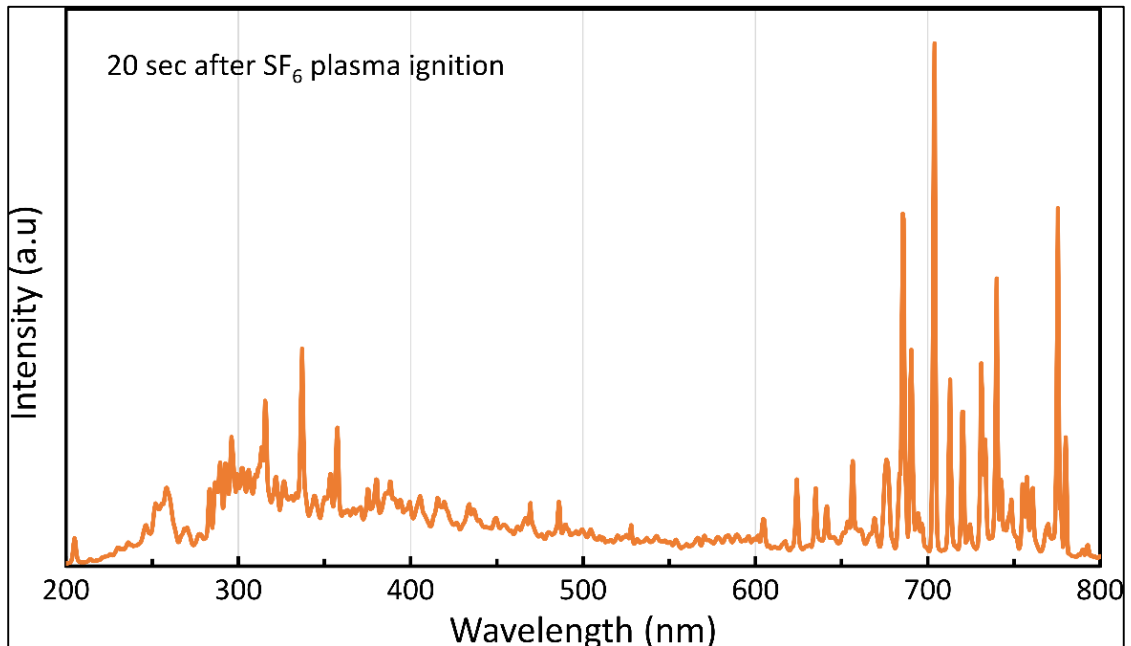


Figure 53: Time dependence of characteristic optical transitions for atomic I, H, N, and F acquired from optical emission spectra of the plasma.



**Figure 54: Optical emission spectrum taken in-situ from gas-discharge plasma 20 sec after plasma ignition. Spectrum is collected using optics collimated to c.a. 5 mm above the substrate surface. A series of well defined, sharp emission lines can be seen and identified with optical transitions in H, N, I, F, as well as, other elements.**

Our data shows the following reaction sequence: (i) ~2 seconds elapse prior to plasma stabilization; (ii) a non-monotonic drop in the intensity of optical transitions associated with perovskite components (I, H, and N) to a constant value after ~50 seconds, as depicted in Figure 53. The significant decrease of intensity for hydrogen lines during initial 5 seconds preceding plasma stabilization indicates that there is a rapid expulsion of organic components from the perovskite film. During this time, the intensity of the I line rises, indicating replacement of iodine with fluorine. Next, intensities of I-line transitions start to slowly decrease until all available iodine is replaced with fluorine. In contrast, intensity of F emission lines is initially small; this is likely due to fluorine consumption during chemical reaction with the film. As functionalization continues, intensity of fluorine emission lines increase with time, for ~50 seconds, before reaching equilibrium with chamber atmosphere. The non-linear

behavior of F- and I-emission intensities can be influenced by variations in film temperature during processing. The final stage of this process is most likely limited by diffusion of fluorine into portions of the perovskite film that are partially protected by  $\text{PbF}_2$ . The exact chemical mechanism of  $\text{SF}_6$  plasma functionalization of perovskite films appears to be complex, to the point where it is beyond the scope of this study, and could provide for the subject of a separate study. Optical spectral data shows that, at given conditions, 60 seconds of  $\text{SF}_6$  plasma treatment is sufficient to completely functionalize 350 nm thick  $\text{CH}_3\text{NH}_3\text{PbI}_3$  films.

Demonstrated advantages of patterning perovskite absorbers for optical imaging applications is shown through an array of patterned photodetecting pixels. These are fabricated by our group and subjected to performance comparison testing with non-patterned devices (Figure 55). Experiments to observe effects of patterning on device performance utilize large ( $2 \times 3 \text{ mm}^2$ ) pixels, which are patterned using lithography and compared to a reference device patterned with shadow mask (Figure 55c). Current-voltage dependence is recorded under AM1.5G  $100 \text{ mW cm}^{-2}$  and in absence of light. Patterned devices exhibit acceptable performance and less than 5% hysteresis, with a short-circuit current density ( $J_{\text{SC}}$ ) of  $18.3 \text{ mA cm}^{-2}$ , open-circuit voltage ( $V_{\text{OC}}$ ) of 0.94 V, fill factor (FF) of 0.68, and power-conversion efficiency (PCE) of 11.7%. These results are similar to reference device ( $J_{\text{SC}} = 19.2 \text{ mA cm}^{-2}$ ,  $V_{\text{OC}} = 0.95 \text{ V}$ , FF = 0.71, and PCE = 13%) and are comparable with other results reported in literature.<sup>68-70</sup> A small decrease in  $J_{\text{SC}}$  and FF for patterned devices maybe caused by processing perovskite films in air, and/or device degradation due to moisture.<sup>71</sup> Figure 55d shows photocurrent versus light intensity for patterned pixel. The device shows a linear response within power density

range from  $10^{-8}$  to  $10^{-1}$   $\text{Wcm}^{-2}$  and a linear dynamic range of over 80 dB. Cross-talk evaluations of patterned and non-patterned photodiode pixels are shown in Figure 55e. The scheme shown in Figure 55a and b with pixel pad size of  $20\ \mu\text{m}$  and a pixel pitch of  $40\ \mu\text{m}$  is meant to quantify amount of signal collected by neighboring pixels. Exposure of a single pixel to an optically attenuated green (532 nm) laser yields generation of photocurrent from that pixel as well as from neighboring pixels, as seen by the simultaneous readouts of separate current amplifiers for each pixel. Neighboring pixels, of non-patterned devices have significant cross-talk of 96%, which can be explained by high photoconductivity of perovskite layers.<sup>3,5</sup>

Patterning of  $\text{PbF}_2$  insulating layers between pixels reduces signal cross-talk to 21%. Due to comparably large band-gap of  $\text{PbF}_2$  dielectric (6 eV),<sup>72</sup> it is believed that remaining signal cross-talk is resultant of optical wave guiding effects, as well as lack of patterning in conductive PEDOT:PSS layer. Remaining signal cross-talk can be further reduced via known methods to pattern PEDOT:PSS,<sup>57,73</sup> or by employing less conductive hole transport layer alternatives. These results are of significant importance in efforts to downscale perovskite photodiodes to pixel sizes suitable for commercial imaging applications ( $\sim 10\text{mm}$ ). Moreover, ability to utilize photolithographic processing enables seamless integration of perovskite photodiodes with CMOS backplanes.

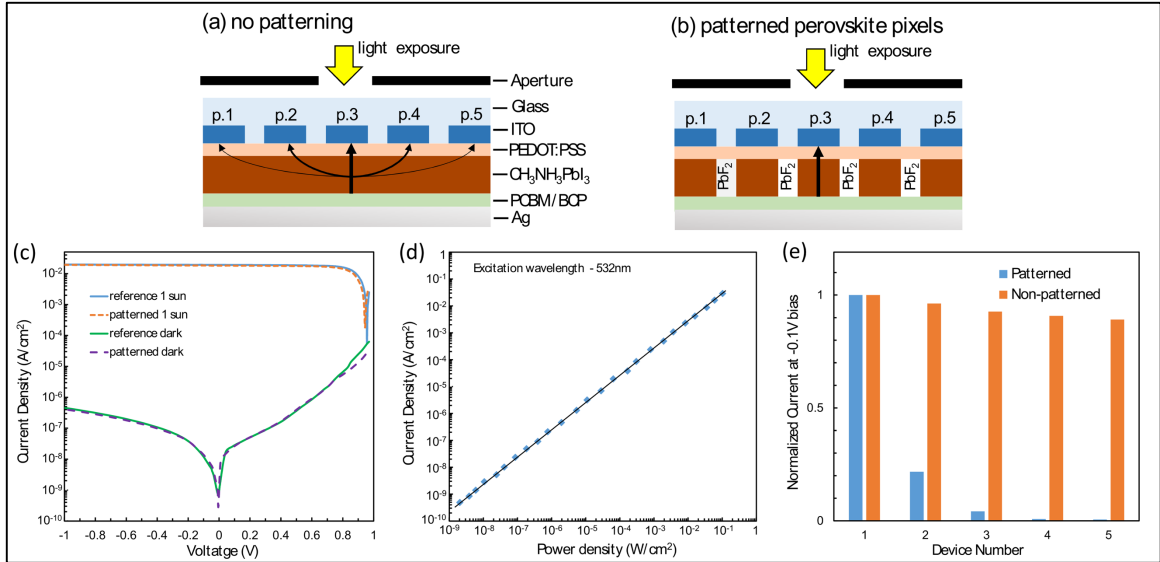


**Figure 55: Device structure of organic perovskite photodiode for (a) non-patterned reference device and (b) patterned device. (c) Current density–voltage curves of photodetectors with and without patterning of perovskite layers for large pixels ( $2 \times 3 \text{ mm}^2$ ). (d) Dynamic range of patterned photodetector at 532 nm optical excitation. Photodetector has a large linear dynamic range  $>80$  dB. (e) Cross-talk between neighboring pixels is measured as ratio of photocurrent, created in central illuminated pixel which reaches adjacent pixels. Applied external bias is  $-0.1 \text{ V}$  and light power is  $500 \mu \text{ W cm}^{-2}$  (532 nm). Each pixel ITO pad size is  $20 \mu \text{ m}$ , while pitch is  $40 \mu \text{ m}$ .**

#### 4. CONCLUSIONS

In this study, we provide a novel sequential deposition technique which utilizes methylammonium acetate (MAAc) to produce perovskite films which exhibit greater film properties, such as uniformity, coverage, smoothness, reproducibility, *etc.* We hypothesize this occurs due to MAAc widening the layers of  $\text{PbI}_2$ , allowing MAI to fully intercalate into these regions before precursor reaction completion. In addition, we suspect that MAAc is slowly removed during perovskite annealing, which allows for more controllable perovskite crystallization. Through various metrology methods, we characterize film properties and device performance for comparison to films and devices made using standard two-step perovskite processing. Results from these comparative studies confirm improved perovskite film characteristics and resulting device performance.

While full optimization of entire device architecture has yet to be completed, we show estimations of resulting performance values that can be expected upon full optimization. Through further optimization of transport layers, performance values should be among the highest in reported literature for  $\text{CH}_3\text{NH}_3\text{PbI}_3$  thin film solar cells and photodetectors. Although full optimization is not achieved in this work, it can provide valuable experience for future research endeavors conducted by future graduate students. This work provides sufficient optimization of perovskite films grown using our novel two-step deposition technique containing MAAc. Further optimization would focus on transport layers and is thus justifiably beyond the scope of this effort.

In addition to providing a novel perovskite growth technique, we present a subtractive patterning technique to provide high-resolution structuring of  $\text{CH}_3\text{NH}_3\text{PbI}_3$ ,

based on orthogonal lithography (Figure 56). This effort shows effectiveness in reducing signal cross-talk between neighboring photodetector pixels. Chemically orthogonal (highly fluorinated) commercial resist and HFE processing solvents are shown to have minimal effect on  $\text{CH}_3\text{NH}_3\text{PbI}_3$  film properties.  $\text{SF}_6$  plasma reactive in etching is used to facilitate pattern transfer. From comprehensive structural analysis (XRD, optical spectra, SEM-EDS) it is concluded that (i) 1 minute of  $\text{SF}_6$  plasma treatment converts unprotected, 350-nm thick, perovskite films to ~200-nm thick, wide band-gap,  $\text{PbF}_2$  glass; (ii) orthogonal resist acts as sufficient protection of perovskite layer against  $\text{SF}_6$  plasma. Use of *in situ* optical emission spectra taken from the vicinity of sample surfaces reveals dynamics of chemical reactions in the plasma by tracing atomic spectral lines of elements involved. Finally, it is demonstrated that this patterning process has only minor negative impact on perovskite photodiode device performance, while significantly decreasing cross-talk between neighboring pixels.

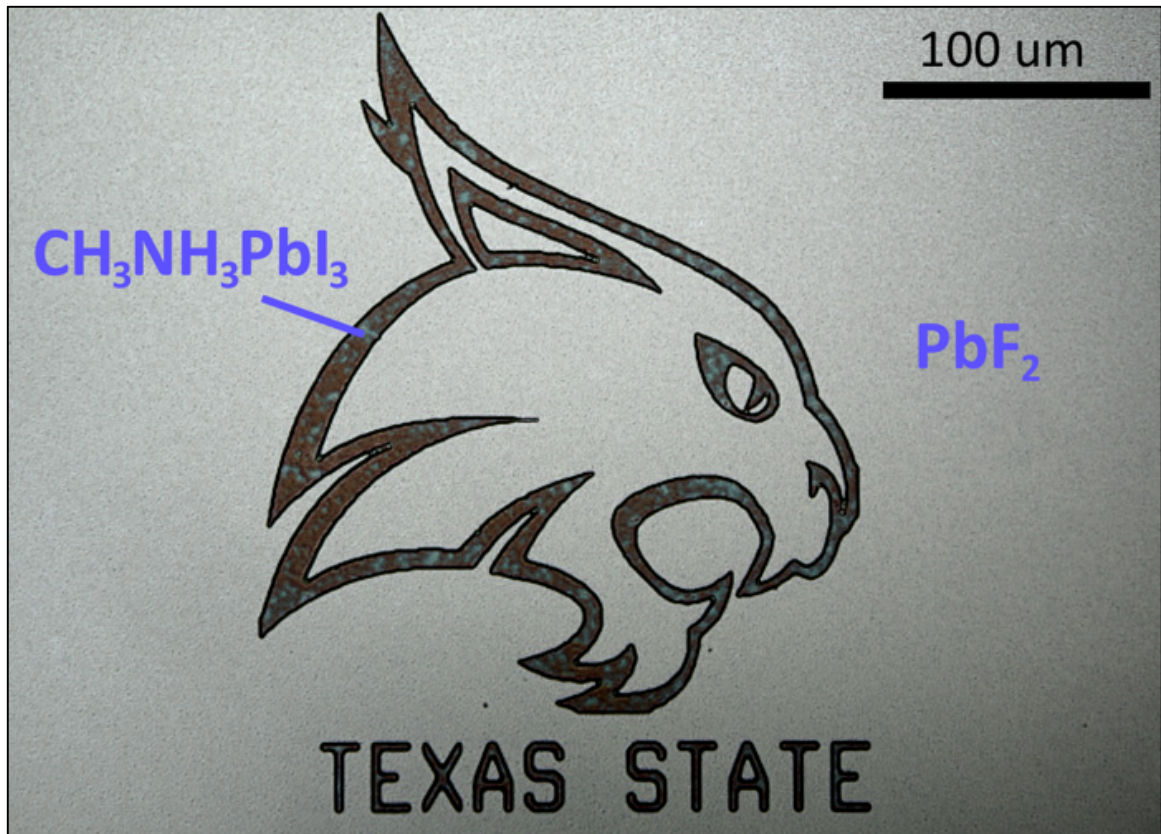


**Figure 56: Patterned perovskite**

The combination of providing a novel deposition process as well as a technique to achieve high-resolution patterning of perovskite thin films brings this fledgling technology a significant step forward in becoming a suitable, cost-effective, alternative to traditional inorganic semiconductor photodiodes for visible light imaging. While further stabilization efforts are necessary to make perovskite solar cells commercially viable, visible spectrum photodetectors are largely utilized in smart phone applications, which have much shorter lifetime requirements. In conclusion, the work presented here makes possible a soon to be realized full commercial-level implementation of perovskite photodiodes to provide cheap, high performing photodiodes for smart phone cameras.

## **APPENDIX SECTION**

Content from “High-Resolution Patterning of Organohalide Lead Perovskite Pixels for Photodetectors using Orthogonal Photolithography” reproduced from John Wiley and Sons under license number 4143250315346.

## REFERENCES

1. Sony. *Newly Developed Stacked CMOS Image Sensor Introduces 'Super Reality'*. (2012).
2. Dou, L. *et al.* Solution-processed hybrid perovskite photodetectors with high detectivity. *Nat. Commun.* **5**, 5404 (2014).
3. Hu, X. *et al.* High-Performance Flexible Broadband Photodetector Based on Organolead Halide Perovskite. *Adv. Funct. Mater.* **24**, 7373–7380 (2014).
4. Horváth, E. *et al.* Nanowires of Methylammonium Lead Iodide ( $\text{CH}_3\text{NH}_3\text{PbI}_3$ ) Prepared by Low Temperature Solution-Mediated Crystallization. *Nano Lett.* **14**, 6761–6766 (2014).
5. Lee, Y. *et al.* High-Performance Perovskite-Graphene Hybrid Photodetector. *Adv. Mater.* **27**, 41–46 (2015).
6. Lyashenko, D., Perez, A. & Zakhidov, A. High-resolution patterning of organohalide lead perovskite pixels for photodetectors using orthogonal photolithography. *Phys. status solidi* **214**, 1600302 (2017).
7. Green, M. A., Emery, K., Hishikawa, Y., Warta, W. & Dunlop, E. D. Solar cell efficiency tables (Version 45). *Prog. Photovoltaics Res. Appl.* **23**, 1–9 (2015).
8. Goldschmidt, V. M. & M., V. Die Gesetze der Krystallochemie. *Naturwissenschaften* **14**, 477–485 (1926).
9. Yin, W.-J. *et al.* Halide perovskite materials for solar cells: a theoretical review. *J. Mater. Chem. A* **3**, 8926–8942 (2015).
10. Xing, G. *et al.* Long-Range Balanced Electron- and Hole-Transport Lengths in Organic-Inorganic  $\text{CH}_3\text{NH}_3\text{PbI}_3$ . *Science (80-. )*. **342**, (2013).
11. Stoumpos, C. C., Malliakas, C. D. & Kanatzidis, M. G. Semiconducting Tin and Lead Iodide Perovskites with Organic Cations: Phase Transitions, High Mobilities, and Near-Infrared Photoluminescent Properties. *Inorg. Chem.* **52**, 9019–9038 (2013).
12. Yin, W.-J., Shi, T. & Yan, Y. Unusual defect physics in  $\text{CH}_3\text{NH}_3\text{PbI}_3$  perovskite solar cell absorber. *Appl. Phys. Lett.* **104**, 63903 (2014).
13. Gonzalez-Pedro, V. *et al.* General Working Principles of  $\text{CH}_3\text{NH}_3\text{PbX}_3$  Perovskite Solar Cells. *Nano Lett.* **14**, 888–893 (2014).
14. Carnie, M. J. *et al.* A one-step low temperature processing route for organolead halide perovskite solar cells. *Chem. Commun.* **49**, 7893 (2013).

15. Ko, H.-S., Lee, J.-W. & Park, N.-G. 15.76% efficiency perovskite solar cells prepared under high relative humidity: importance of  $\text{PbI}_2$  morphology in two-step deposition of  $\text{CH}_3\text{NH}_3\text{PbI}_3$ . *J. Mater. Chem. A* **3**, 8808–8815 (2015).
16. Im, J.-H., Kim, H.-S. & Park, N.-G. Morphology-photovoltaic property correlation in perovskite solar cells: One-step versus two-step deposition of  $\text{CH}_3\text{NH}_3\text{PbI}_3$ . *APL Mater.* **2**, 81510 (2014).
17. Moore, D. T. *et al.* Crystallization Kinetics of Organic–Inorganic Trihalide Perovskites and the Role of the Lead Anion in Crystal Growth. *J. Am. Chem. Soc.* **137**, 2350–2358 (2015).
18. Yang, W. S. *et al.* High-performance photovoltaic perovskite layers fabricated through intramolecular exchange. *Science (80-. )*. **348**, 1234–1237 (2015).
19. Jeon, N. J. *et al.* Solvent engineering for high-performance inorganic–organic hybrid perovskite solar cells. *Nat. Mater.* **13**, 897–903 (2014).
20. Tavernier, F. & Steyaert, M. *High-Speed Optical Receivers with Integrated Photodiode in Nanoscale CMOS*. (Springer New York, 2011). doi:10.1007/978-1-4419-9925-2
21. Green, M. A., Ho-Baillie, A. & Snaith, H. J. The emergence of perovskite solar cells. *Nat. Photonics* **8**, 506–514 (2014).
22. Burschka, J. *et al.* Sequential deposition as a route to high-performance perovskite-sensitized solar cells. *Nature* **499**, 316–319 (2013).
23. Dong, Q. *et al.* Electron-hole diffusion lengths > 175  $\mu\text{m}$  in solution-grown  $\text{CH}_3\text{NH}_3\text{PbI}_3$  single crystals. *Science (80-. )*. **347**, (2015).
24. Gonzalez-Pedro, V. *et al.* General Working Principles of  $\text{CH}_3\text{NH}_3\text{PbX}_3$  Perovskite Solar Cells. *Nano Lett.* **14**, 888–893 (2014).
25. Dong, Q. *et al.* Electron-hole diffusion lengths > 175  $\mu\text{m}$  in solution-grown  $\text{CH}_3\text{NH}_3\text{PbI}_3$  single crystals. *Science (80-. )*. **347**, 967–970 (2015).
26. Kim, H.-S. *et al.* Control of  $I-V$  Hysteresis in  $\text{CH}_3\text{NH}_3\text{PbI}_3$  Perovskite Solar Cell. *J. Phys. Chem. Lett.* **6**, 4633–4639 (2015).
27. Wu, Y. *et al.* Retarding the crystallization of  $\text{PbI}_2$  for highly reproducible planar-structured perovskite solar cells via sequential deposition. *Energy Environ. Sci.* **7**, 2934 (2014).
28. Yang, W. S. *et al.* High-performance photovoltaic perovskite layers fabricated through intramolecular exchange. *Science (80-. )*. **348**, (2015).

29. Yang, W. S. *et al.* High-performance photovoltaic perovskite layers fabricated through intramolecular exchange. *Science (80-. )*. **348**, (2015).
30. Zhang, W. *et al.* Ultrasmooth organic–inorganic perovskite thin-film formation and crystallization for efficient planar heterojunction solar cells. *Nat. Commun.* **6**, 6142 (2015).
31. Silicon Photodetectors. (2016). Available at: [http://www.eotech.com/content/userfiles/Silicon Photodetectors.pdf](http://www.eotech.com/content/userfiles/Silicon%20Photodetectors.pdf). (Accessed: 6th June 2017)
32. GaAs Photodetector Data Sheet. (2016). Available at: [http://www.eotech.com/content/userfiles/12.5GHz Photodetectors.pdf](http://www.eotech.com/content/userfiles/12.5GHz%20Photodetectors.pdf).
33. Park, H., Yang, G., Chun, S., Kim, D. & Kim, J. CdTe microwire-based ultraviolet photodetectors aligned by a non-uniform electric field. *Cit. Appl. Phys. Lett* **103**, (2013).
34. He, Z.-Y. *et al.* CdTe nBn photodetectors with ZnTe barrier layer grown on InSb substrates. *Cit. Appl. Phys. Lett. Junction Sol. Cells J. Appl. Phys. Appl. Phys. Lett.* **109**, 121112–151109 (2016).
35. Zhang, Y. *et al.* Ultrasensitive photodetectors exploiting electrostatic trapping and percolation transport. *Nat. Commun.* **7**, 11924 (2016).
36. High Performance Photodiode Sensors. (2017). Available at: [https://www.newport.com/medias/sys\\_master/images/images/hf0/hb9/8797036544030/918D-Series-High-Performance-Photodiode-Sensors-Data-Sheet.pdf](https://www.newport.com/medias/sys_master/images/images/hf0/hb9/8797036544030/918D-Series-High-Performance-Photodiode-Sensors-Data-Sheet.pdf). (Accessed: 6th June 2017)
37. Li, F. *et al.* Ambipolar solution-processed hybrid perovskite phototransistors. *Nat. Commun.* **6**, 8238 (2015).
38. Stevens, G. W. W. *Microphotography: Photography and Photofabrication at Extreme Resolution*. (Wiley, 1968).
39. L. F. Thompson, Grant Willson, M. J. B. *Introduction to Microlithography*. (American Chemical Society, 1994).
40. Moreau, W. M. *Semiconductor Lithography : Principles, Practices, and Materials*. (Springer US, 1988).
41. Elliott, D. J. *Integrated circuit fabrication technology*. (McGraw-Hill, 1982).
42. Campbell, S. A. *Fabrication engineering at the micro and nanoscale*. (Oxford University Press, 2008).

43. Cheng, Z. Y., Wang, Z., Xing, R. B., Han, Y. C. & Lin, J. *Patterning and photoluminescent properties of perovskite-type organic/inorganic hybrid luminescent films by soft lithography*. *Chemical Physics Letters* **376**, (2003).
44. Meng, K. *et al.* Two-Dimensional Organic–Inorganic Hybrid Perovskite Photonic Films. *Nano Lett.* **16**, 4166–4173 (2016).
45. Alias, M. S. *et al.* Enhanced Etching, Surface Damage Recovery, and Submicron Patterning of Hybrid Perovskites using Chemically Gas-Assisted Focused-Ion Beam for Subwavelength Grating Photonic Applications. *Phys. Chem. Lett.* **7**, 137–142 (2015).
46. Zimmermann, E. *et al.* Characterization of perovskite solar cells: Towards a reliable measurement protocol. *APL Mater.* **4**, 91901 (2016).
47. Brenner, T. J. K. *et al.* White-light bias external quantum efficiency measurements of standard and inverted P3HT:PCBM photovoltaic cells. *J. Phys. D. Appl. Phys.* **45**, 415101 (2012).
48. You, J. *et al.* Moisture assisted perovskite film growth for high performance solar cells. *Appl. Phys. Lett.* **105**, 183902 (2014).
49. Urai, J. L. Water assisted dynamic recrystallization and weakening in polycrystalline bischofite. *Tectonophysics* **96**, 125–157 (1983).
50. Yin, W.-J., Shi, T. & Yan, Y. Unique Properties of Halide Perovskites as Possible Origins of the Superior Solar Cell Performance. *Adv. Mater.* **26**, 4653–4658 (2014).
51. Liu, M., Johnston, M. B. & Snaith, H. J. Efficient planar heterojunction perovskite solar cells by vapour deposition. *Nature* **501**, 395–398 (2013).
52. Oku, T. in *Solar Cells - New Approaches and Reviews* (InTech, 2015). doi:10.5772/59284
53. Edri, E. *et al.* Why Lead Methylammonium Tri-Iodide Perovskite-Based Solar Cells Require a Mesoporous Electron Transporting Scaffold (but Not Necessarily a Hole Conductor). *Nano Lett.* **14**, 1000–1004 (2014).
54. Lin, Q., Armin, A., Nagiri, R. C. R., Burn, P. L. & Meredith, P. Electro-optics of perovskite solar cells. *Nat Phot.* **9**, 106–112 (2015).
55. Krotkus, S. *et al.* Photo-patterning of Highly Efficient State-of-the-Art Phosphorescent OLEDs Using Orthogonal Hydrofluoroethers. *Adv. Opt. Mater.* **2**, 1043–1048 (2014).
56. Kleemann, H. *et al.* Direct structuring of C60 thin film transistors by photolithography under ambient conditions. *Org. Electron.* **13**, 506–513 (2012).

57. Midthun, K. M. *et al.* Orthogonal Patterning of Multiple Biomolecules Using an Organic Fluorinated Resist and Imprint Lithography. *Biomacromolecules* **14**, 993–1002 (2013).
58. Szpikowska-Sroka, B. *et al.* Long-lived emission from Eu<sup>3+</sup>:PbF<sub>2</sub> nanocrystals distributed into sol–gel silica glass. *J. Sol-Gel Sci. Technol.* **68**, 278–283 (2013).
59. Ren, G.-H. *et al.* Radiation Induced Optical Absorption of Cubic Lead Fluoride Crystals and the Effect of Annealing. *Chinese Phys. Lett.* **31**, 86102 (2014).
60. John, R. A. *et al.* Modulating Cationic Ratios for High-Performance Transparent Solution-Processed Electronics. *ACS Appl. Mater. Interfaces* **8**, 1139–1146 (2016).
61. Bale, M. & Palmer, R. E. Deep plasma etching of piezoelectric PZT with SF<sub>6</sub>. *J. Vac. Sci. Technol. B AIP Conf. Proc. J. Vac. Sci. Technol. A J. Vac. Sci. Technol. A J. Vac. Sci. Technol. B J. Vac. Sci. Technol. A* **19**, 719–2467 (2020).
62. Orvek, K. J. & Huffman, C. Carbonized layer formation in ion implanted photoresist masks. *Nucl. Instruments Methods Phys. Res. Sect. B Beam Interact. with Mater. Atoms* **7–8**, 501–506 (1985).
63. Minnhagen, L. No Title. *Ark. Fys.* 415 (1962).
64. Martin, W. C. & Corliss, C. H. The Spectrum of Singly Ionized Atomic Iodine (I II). *J. Res. Natl. Bur. Stand. Phys. Chem.* **64A**, (1960).
65. Baker, J. *Transition probabilities for one electron atoms. Natl. Inst. Stand. Technol. Technical Note* (2008).
66. Moore, C. E. in *Nat. Stand. Ref. Data Ser., NSRDS-NBS 3 (Sect. 5)* (Nat. Bur. Stand., U.S., 1975).
67. Lidén, K. The Arc Spectrum of Fluorine. *Ark. Fys.* **1**, 229–267 (1949).
68. Kim, H.-S. *et al.* Lead Iodide Perovskite Sensitized All-Solid-State Submicron Thin Film Mesoscopic Solar Cell with Efficiency Exceeding 9%. *Sci. Rep.* **2**, 591 (2012).
69. Lee, M. M., Teuscher, J., Miyasaka, T., Murakami, T. N. & Snaith, H. J. Efficient hybrid solar cells based on meso-superstructured organometal halide perovskites. *Science* **338**, 643–7 (2012).
70. Etgar, L. *et al.* Mesoscopic CH<sub>3</sub>NH<sub>3</sub>PbI<sub>3</sub>/TiO<sub>2</sub> heterojunction solar cells. *J. Am. Chem. Soc.* **134**, 17396–9 (2012).

71. Yuan, H. *et al.* Degradation of Methylammonium Lead Iodide Perovskite Structures through Light and Electron Beam Driven Ion Migration. *J. Phys. Chem. Lett.* **7**, acs.jpcclett.5b02828 (2016).
72. Itoh, M., Nakagawa, H., Kitaura, M., Fujita, M. & Alov, D. L. Photoluminescence of orthorhombic and cubic single crystals. *J. Phys. Condens. Matter* **11**, 3003–3011 (1999).
73. Radivo, A. *et al.* Patterning PEDOT:PSS and tailoring its electronic properties by water-vapour-assisted nanoimprint lithography. *RSC Adv.* **4**, 34014 (2014).